Politecnico di Milano
SCHOOL OF INDUSTRIAL AND INFORMATION ENGINEERING
Master of Science – Energy Engineering

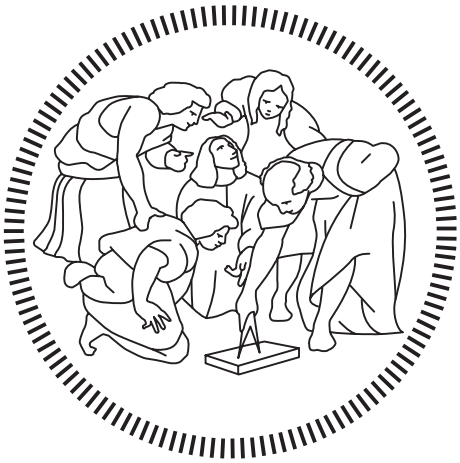

Direct Observation of Dissolution Processes in a Microfluidic Device Designed onto a Natural Rock Surface

Supervisor
Professor Alberto GUADAGNINI

Candidate
Federico PASOTTI – 918554

Academic Year 2019 – 2020

Ringraziamenti

Nel presentare questo lavoro di tesi, che segna la conclusione del mio percorso universitario, vorrei cogliere l'occasione per ringraziare coloro che mi hanno supportato in questi anni.

In primis, un ringraziamento al Professor Alberto Guadagnini, relatore di questa tesi, per la disponibilità con la quale mi ha aiutato e sostenuto durante lo svolgimento del mio lavoro.

Un ringraziamento al Professor Pietro de Anna dell'Università di Losanna, mio tutor durante la mia permanenza presso l'Istituto di Scienze della Terra, per avermi accolto nel suo gruppo di lavoro e per avermi aiutato nell'esecuzione della ricerca.

Vorrei ringraziare anche Ankur per avermi insegnato a lavorare in un laboratorio e le altre persone del gruppo di lavoro del Professor de Anna, che sono sempre state pronte ad aiutarmi in caso di bisogno.

Grazie ai colleghi con cui ho condiviso gli anni al Politecnico di Milano e la fantastica esperienza Erasmus a Trondheim.

Un sentito ringraziamento ai miei amici, da quelli di lunga data a quelli conosciuti più recentemente, con cui condivido momenti speciali, in particolare gli "Universinauti" e gli "Apostoli".

Un grazie ai miei nonni e a mio zio per essere sempre presenti e per ricordarmi sempre dell'importanza della famiglia.

Un ringraziamento speciale a mia mamma e a mio papà per avermi sempre supportato, sia nelle gioie che nelle difficoltà, per avermi sostenuto economicamente, per avermi cresciuto per quello che sono, perché senza di voi non avrei raggiunto alcun traguardo.
Ringrazio infinitamente mia sorella, per il supporto e l'incoraggiamento, perché rendi la vita meno noiosa che mai. Un enorme grazie, inoltre, per aver pazientemente revisionato le bozze del mio lavoro.

Un sentito ricordo per mio nonno Vincenzo, a cui dedico questo traguardo, nella speranza di averti reso orgoglioso.

Federico Pasotti

Sommario

I processi di trasporto reattivo in mezzi porosi sono studiati in diverse aree, tra cui l'industria del petrolio e del gas. Una migliore comprensione dei processi alla scala del poro è necessaria per lo sviluppo di modelli adatti per la scala della carota e la scala di campo. Tradizionalmente, gli studi sui mezzi porosi sono effettuati in esperimenti su carote, che, ovviamente, sono chimicamente e fisicamente rappresentativi di un mezzo poroso. Tuttavia, gli esperimenti sulle carote non consentono l'osservazione e la quantificazione dei processi alla scala del poro, che è necessaria per una migliore modellizzazione dei processi di trasporto reattivo. Alcune tecniche possono essere utilizzate per l'analisi su scala del poro in esperimenti sulle carote, ma sono complesse e costose. Di conseguenza, l'impiego di modelli microfluidici dei mezzi porosi si è diffuso. I dispositivi microfluidici consentono, accoppiandoli con un microscopio e una fotocamera, l'osservazione e lo studio dei processi alla scala del poro. Tuttavia, i modelli microfluidici classici possono imitare solo la geometria di un mezzo poroso, ma non sono rappresentativi della complessità chimica e fisica di un mezzo poroso reale, non permettendo la quantificazione di alcuni processi, come la dissoluzione della roccia. Alcuni studi precedenti sono stati finalizzati al trovare una soluzione per rendere i dispositivi microfluidici classici adatti allo studio della dissoluzione delle rocce o chimicamente rappresentativi di un mezzo poroso reale. Tuttavia, non è ancora stato raggiunto un risultato definitivo.
In questo studio, viene presentato un nuovo dispositivo microfluidico in roccia reale: il rock-in-chip microfluidics, nel quale i canali microfluidici sono fabbricati in una roccia naturale. Questo dispositivo mira ad essere un'unione tra le caratteristiche positive sia delle carote che dei dispositivi microfluidici classici. Infatti, come le carote, rappresenta le proprietà chimiche e fisiche di un mezzo poroso reale, essendo costituito di roccia reale. Inoltre, come i dispositivi microfluidici classici, permette l'osservazione e la quantificazione dei processi alla scala del poro. I canali microfluidici sono direttamente incisi su calcite naturale, risultando in un chip con la stessa geometria di un dispositivo microfluidico classico, ma la complessità fisica e chimica di un mezzo poroso reale. I canali microfluidici sono sigillati con un vetrino su un lato e con uno strato di PDMS sull'altro. Inoltre, viene presentato un protocollo sperimentale e di analisi per l'osservazione e la quantificazione della dissoluzione della roccia. Il protocollo sperimentale è stato precedentemente testato e validato per l'applicazione con classici dispositivi microfluidici in PDMS. Successivamente, è stato applicato allo studio del rock-in-chip microfluidics, che è stato inizialmente caratterizzato in conducibilità idraulica. Successivamente, l'elaborazione e l'analisi delle immagini sono state utilizzate per l'osservazione e la quantificazione della dissoluzione della roccia. Gli esperimenti hanno dimostrato che il rock-in-chip microfluidics può essere utilizzato per l'osservazione e la quantificazione della dissoluzione naturale delle rocce, quindi il protocollo sperimentale sviluppato è stato validato come metodo per l'osservazione e per la quantificazione della dissoluzione di rocce naturali.

Parole chiave: dissoluzione di roccia, microfluidica, dispositivo microfluidico in roccia naturale, quantificazione della dissoluzione, osservazione della dissoluzione, analisi alla scala del poro

Abstract

Reactive transport processes in porous media are studied in several areas, among which the oil and gas industry. A better understanding of the pore scale processes is required in order to develop models suitable for the core scale and the reservoir scale. Traditionally, porous media studies have been performed in core sample experiments, which, obviously, are both chemically and physically representative of a porous medium. However, core sample experiments do not allow the observation and quantification of processes at the pore scale, which is necessary for a better modeling of reactive transport processes. Some techniques can be employed for pore scale analysis in core sample experiments, but they are complex and expensive. As a result, the employment of microfluidic models of porous media has spread. Microfluidic devices permit the observation and the study of pore scale processes, by coupling them with a microscope and a camera. Nevertheless, classic microfluidic models can mimic only the geometry and the topology of a porous media, but they are not representative of the chemical and physical complexity of a real porous medium, not allowing the quantification of some processes, such as rock dissolution. Some previous studies have gone in the direction of finding a solution to make classical microfluidic devices suitable for the study of rock dissolution, or chemically representative of a real porous medium. However, a definitive result has not yet been reached.

In this study, a novel real rock microfluidic device is presented: the rock-in-chip microfluidics, whereby the microfluidic channels are fabricated onto a natural rock. This device aims to be a union between the positive features of both core samples and classic microfluidic devices. In fact, likewise the core samples, it is a good representative of the chemical and physical properties of a real porous medium, being made of real rock. Moreover, similarly to classic microfluidic devices, it allows the observation and quantification of processes at the pore scale. Therefore, it is a possible solution for the studying of reactive transport processes in porous media at the pore scale. In the rock-in-chip microfluidics, the microfluidic channels are directly etched onto a substrate of natural calcite, resulting in a chip with the same geometry as a classic microfluidic device, but the physical and chemical complexity of a real porous medium. The microfluidic channels are sealed with a glass slide on one side and with a polydimethylsiloxane (PDMS) layer on the other one. Moreover, an experimental and analysis protocol for the observation and quantification of the dissolution of the real rock of the rock-in-chip microfluidics is presented. The experimental protocol was previously tested and validated for the application with classic PDMS microfluidic devices. Afterwards, it was applied to the study of the rock-in-chip microfluidics, which was initially characterized in hydraulic conductivity. After that, image processing and image analysis were used for the observation and quantification of the dissolution of the real rock of the rock-in-chip microfluidics. The experiments proved that the rock-in-chip microfluidics could be employed for the observation and quantification of

natural rock dissolution, thus validated the experimental protocol as a method for real rock dissolution observation and quantification.

Keywords: rock dissolution, microfluidics, natural rock microfluidic device, dissolution quantification, dissolution observation, pore scale analysis

Extended Abstract

Introduction

The study of reactive transport processes in porous media plays an important role in the oil and gas industry. The development of models to represent these processes is researched for a better understanding of what happens at the pore scale [1]. Traditionally, porous media studies have been performed with core sample experiments. However, these experiments act as a black box, not allowing the observation of pore scale processes, which need to be understood for a better models' development for reactive transport processes in porous media. Some technologies – such as neutron radiography, high resolution optical profilometry, magnetic resonance imaging, X-ray computed tomography and synchrotron-based μ-CT – are employed for pore scale visualization in core samples. Nevertheless, they are complex and expensive techniques [2].

Therefore, the employment of microfluidic model porous media has spread. Microfluidics is a scientific discipline that studies movement, handling and manipulation of liquid substances in microvolumes across micro-scales. Microfluidic devices allow the observation of the phenomena at pore scale when they are coupled with a microscope and a camera, thanks to their transparency to light; however, they mimic a porous medium only for geometry and topology, not for physical and chemical complexity.

Alzahid et al. (2018) [3] have functionalized a PDMS microfluidic device by coating with rock minerals, in order to partially overcome this issue. They placed 1 ml of a mineral solution on top of a PDMS channel, previously subjected to plasma treatment, and sealed the device by bounding it to a plasma treated blank PDMS cover. As a result, they obtained a microfluidic model with height and surface roughness similar to those of a rock. However, such a microfluidic device is not able to also replicate the chemical complexity of a real rock since the structure is made of PDMS mainly. Therefore, dissolution of rock cannot be studied employing a microfluidic device like this one.

Yoon et al. (2019) [4] have carried out an analysis of calcium carbonate dissolution within a porous medium in a microfluidic device. However, they were not able to study directly rock dissolution since they employed a silicon microfluidic device. They injected into the microfluidic channel two solutions – one of calcium chloride and one of sodium carbonate –, which resulted in the precipitation of calcium carbonate. Subsequently, a solution of water and hydrochloric acid was injected, resulting in the dissolution of calcium carbonate previously precipitated. Images were acquired – during both precipitation and dissolution – and analysed, in order to evaluate reaction rates. However, they concluded that a real rock microfluidic device would have been essential for a complete study of the problem.

Few examples of such a microfluidic device can be found in literature: one of these is the work by Singh et al. (2017) [2]. Starting from a sandstone core they fabricated a real rock microfluidic device with a 500 μm-thick real rock wafer. The rock wafer was placed in a PDMS channelized layer, sealed on the top with another PDMS layer, and sealed laterally

with liquid PDMS. Then, the device was blocked with two clamps. They performed flooding tests and acquired images. However, they did not perform experiments to study the dissolution of the real rock of the microfluidic device.
In the present work, a novel type of real rock microfluidic device will be presented: a rock-in-chip microfluidics device. The goal was the fabrication of a microfluidic model for the study of reactive transport processes at the pore scale. The rock for the microfluidic chip was etched, resulting in a chip with the same geometry as a classic microfluidic device, but the physical and chemical complexity of a real porous medium, overcoming the limitations of classic microfluidic devices. Moreover, an experimental and analysis protocol for the quantification of the porous medium's properties variations due to rock dissolution will be presented.
Some further tests anticipated the experimentation of the rock-in-chip microfluidics, in order to validate the experimental protocols: firstly, a classic PDMS microfluidic device was characterized in hydraulic conductivity, at a later stage a PIV analysis for the determination of the fluid velocity within a classic PDMS microfluidic channel was performed. Finally, the testing of rock-in-chip microfluidics was carried out.

Materials

The main component of the experimental system was the microfluidic device mimicking a porous medium. Two different microfluidic chips were employed: a classic PDMS microfluidic device and the novel real rock microfluidic device, the rock-in-chip microfluidics. PDMS microfluidic devices are widely used in several scientific field, thus it was fabricated following the soft lithography method reported in literature [5]. The PDMS microfluidic channels employed had two different geometries: one was a porous medium with circular grains of variable diameters; the other was a porous medium with a complex geometry. However, both the types had the same sizes: width 7 mm, length 51 mm, height 50 μm.
Concerning the rock-in-chip microfluidics fabrication, it will be treated later in this paragraph.
Three different working fluids were used during the experimental works. One was just Milli-Q water, employed when neither microscope imaging nor rock dissolution were desired. A second working fluid was used to carry out a PIV analysis, for which it was necessary to use a fluid that contained within its own - as tracers - some elements easily detectable in the acquired images. For this purpose, 1 ml of a suspension of Milli-Q water and fluorescent tracer beads – in a ratio 12.5/1 by volume – was diluted with 852 μl of heavy water, used to match the densities of the beads and the fluid. The third working fluid was to be employed for the rock-in-chip microfluidics dissolution, thus it had to have two characteristics: (1) to be able to dissolve calcite; (2) to be clearly distinguishable under the microscope. To this end, a solution of Milli-Q water and fluorescein concentrated at 3 mg/l, and acetic acid was selected. The concentration of acetic acid was 1:1000, resulting in a solution with a pH of about 2.5. The fluorescein was used in order to acquire fluorescence images during the experiments. Moreover, fluorescent tracer beads were added to the above solution with the aim of performing PIV analysis during rock-in-chip microfluidics dissolution.

Two different flow control systems were employed: (1) a programmable 5 ml syringe pump (Harvard Apparatus) when a flow rate had to be imposed; (2) a pressure controller (Elveflow OBI1 Mk3) when a pressure difference between the ends of the hydraulic circuit was needed. The mass was measured with an analytical balance (Fisherbrand™ Analytical Balance).
The visualization system was composed by an inverted microscope (Nikon Eclipse Ti) and two different cameras (Nikon DS-Qi2 and Hamamatsu ORCA flash 4.0 V3). It has to be noted that the cameras were never used both at the same time. A SOLA light source was used to capture fluorescence images. Both the microscope and the camera were controlled remotely through the use of the Nikon's software NIS-Elements.

Rock-in-chip microfluidics device
The rock-in-chip microfluidics was fabricated with calcite ($CaCO_3$): a slice of rock of the thickness of some mm was cut from a block of calcite in order to be subjected to the successive workings for the fabrication of the chip.
The chip was fabricated as follows: photolithographic patterns were obtained by spin-coating a positive, photosensitive resist exposed to a near-UV laser (375 nm wavelength, fluency of about 2.7 mW) on a spot of about 2 μm (Dilase 250, from Kloe). The exposed portions of the resist were removed with a developer. The rock was then etched dipping them for 15 minutes in a solution of 1 ml of nitric acid (HNO_3) in 99 ml of deionised water, creating a porous medium geometry with circular grains of variable diameters. After the rock had been etched, it was attached to a glass slide so that it would have served as the bottom base of the microfluidic channel (Figure 1, left). The dimensions of the porous medium microfluidic channel used in the experiment were: width 2 mm, length 30 mm, height 40 μm. The rock-in-chip microfluidics was sealed in the following way: the chip was placed above a glass slide – used as a base – and sealed from above with a PDMS layer of about 2 mm and a 2 mm thick plexiglass layer above it. Finally, the device was blocked with a clamp and two screws (Figure 1, right).

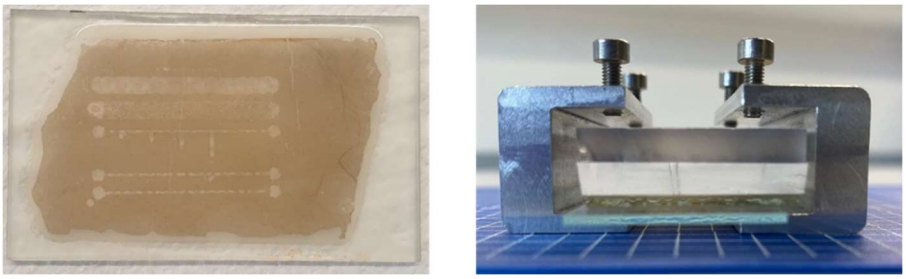

Figure 1 - Rock-in-chip microfluidics. Left: rock chip. Right: assembled device

Methods

Classic microfluidic hydraulic properties evaluation
In the first working phase, the hydraulic properties of a classic PDMS microfluidic device were measured; in particular, the aim was to determine the hydraulic conductivity of a microfluidic channel. Hydraulic conductivity expresses the ease with which a fluid is transported through a porous matrix in presence of a hydraulic gradient [6]. The experimental setup was composed by the PDMS microfluidic device - with circular grains geometry – linked to an inlet reservoir and an outlet reservoir, placed on the scale for mass

measurements, with PVC tubings. The two reservoirs were connected to the pressure controller, which established a pressure difference between them. The working fluid was Milli-Q water.
The experiment was carried out by imposing a pressure difference between the reservoirs and measuring the mass of the outlet reservoir. Initial pressure difference was 100 mbar. Every 120 s the pressure difference was increased by 10 mbar, until a final pressure difference of 200 mbar was reached.
From the data of mass, the average Darcy velocity for each pressure difference step was calculated, while the average hydraulic gradient for each step was obtained from the pressure difference data. Considering the Darcy's law

$$q = K \cdot i \tag{1}$$

where K is the hydraulic conductivity and i is the hydraulic gradient, it results that hydraulic conductivity is the proportionality constant between Darcy velocity and hydraulic gradient. A linear interpolation of the data points obtained from the data analysis was performed: as a result, the slope of the interpolant was the hydraulic conductivity. The hydraulic conductivity was compared to the theoretical evaluation of the hydraulic conductivity according to Kozeny-Carman

$$K = \frac{D^2 \phi^3}{180(1-\phi)^2} \frac{\rho g}{\mu} \tag{2}$$

where D is the characteristic dimension for the flow, ϕ is the porosity, ρ is the density, g is the acceleration due to gravity, μ is the viscosity.
The Kozeny-Carman model does not reflect properly the geometry of the microfluidic device; thus, the evaluation was expected to be of the same order of magnitude so as to validate the experimental setup, but not to be equal.

Particle Image Velocimetry (PIV) on classic microfluidic device
Subsequently, a Particle Image Velocimetry (PIV) was performed in order to analyse the flow field and the velocity of the working fluid through the microfluidic channel [7]. Moreover, a methodology to be applied to the rock-in-chip microfluidics was developed. The experimental setup was composed by a PDMS microfluidic device – with complex geometry – placed on the microscope stage, in order to allow the visualization of the microfluidic channel. The microfluidic device was connected to the syringe pump - at the inlet end -, and to an outlet reservoir – at the outlet end – by PVC tubings. The Nikon DS-Qi2 camera was mounted on the microscope in order to acquire images. The suspension with fluorescent beads was employed as working fluid.
The fluid flow rate was imposed to be 0.1 µl/min with the syringe pump. The camera captured images in a 5 mm x 1.5 mm area of the microfluidic channel, as a result of the acquisition in 21 different locations. For each location, 150 images at successive instants of time at single exposure were acquired.
The captured images were processed with the aim of creating new images – starting from the original ones – more suitable for the analysis. Two methods were employed: averaging

– in order to create a background image -, and thresholding – in order to create a mask of the microfluidic channel -. By processing images, new images cleaned from the noise were obtained.
For the analysis, the images were subdivided into interrogation windows. A 3 passes cross-correlation between every interrogation window of two images acquired in two successive instants of time was employed for the analysis. It obtained the average displacement between the analysed images and then, by dividing the displacement by the time delay between the two images, the velocity was calculated. As the captured images were 150, 149 velocities were found for each interrogation window; thus, an average velocity was considered for each of them. In this way, a velocity field of the microfluidic channel was obtained. Moreover, averaging all the velocities calculated, an average velocity for the whole investigated area was found. As last step, the average velocity evaluated with PIV analysis was compared to the velocity derived from the imposed fluid flow rate of the syringe pump.

Rock-in-chip microfluidics experimentation
The last phase of the work was the experimentation of the novel rock-in-chip microfluidics, with three main objectives:

- testing of the device under experimental conditions
- assessment of the hydraulic conductivity of the microfluidic channel
- use of image analysis to assess porous medium properties during rock dissolution

Differently from what was intended, PIV analysis could not be performed on rock-in-chip microfluidics because of a not optimal manufacturing of the microfluidic channel. In fact, a residual rock layer of some μm remained at the base of the microfluidic chip after etching, making impossible to detect the fluorescent beads for the PIV images under the microscope. Nevertheless, the potential for coupling PIV analysis with dissolution analysis remains unchanged, as will be stated in the section on future developments.
The experimental setup was more complex than those previously described. The rock-in-chip microfluidics was placed on the microscope stage, with mounted the Hamamatsu ORCA flash 4.0 V3 camera for imaging. The outlet section was connected to an outlet reservoir, placed on the scale for mass measurements. The inlet section was connected to two different inlet reservoirs: one containing a solution of Milli-Q water and fluorescein concentrated at 3 mg/l, the other containing the solution of Milli-Q water, fluorescein, acetic acid and fluorescent beads. A 3-way valve was employed to select which of the inlet reservoir had to be hydraulically connected with the rock-in-chip microfluidics. The pressure controller was linked with all the reservoirs, in order to impose the pressures.
Initially, the reservoir with Milli-Q water and fluorescein solution was employed as inlet reservoir. A pressure difference of 100 mbar between inlet and outlet reservoir was set and it was checked in real time under the microscope that no leakage or breakage of the chip happened. After that, the first experimental phase involving the evaluation of the hydraulic conductivity of the rock-in-chip microfluidics started. In order to do that, the pressure of the outlet reservoir was set to 20 mbar with the pressure controller, while the pressure of the inlet reservoir – the one with Milli-Q water and fluorescein solution – was varied linearly

from 20 mbar to 200 mbar over 10 minutes, resulting in an increasing pressure difference between the reservoirs. The mass of the outlet reservoir was measured during the experiment. Subsequently, the collection of data for the evaluation of properties changes due to rock dissolution started. At this point, the inlet reservoir was switched to the one with the rock dissolving solution. The experiment - during which images were acquired - lasted 24 hours. For the first hour, the pressure difference between the inlet and outlet reservoirs was set to 10 mbar, for the remaining 23 hours it was set to 180 mbar instead. Images of the whole rock-in-chip microfluidics were taken every 20 minutes with two modalities: (1) fluorescence acquisition – for images to be analysed -; (2) bright-field images – only for qualitative observation -. The acquisition of images for PIV analysis should have been collected if it were possible.
After the data acquisition ending, data analysis took place. Similarly to what was done for the classic PDMS microfluidic channel, the Darcy velocities were calculated from mass measurements and the hydraulic gradients were calculated from pressure difference data. A linear interpolation was performed: the hydraulic conductivity resulted to be the slope of the interpolation straight line. Even in this case, the resulting hydraulic conductivity was compared to its theoretical evaluation according to the Kozeny-Carman formula.
The captured fluorescent images were processed – before analysis – with two methods: Gaussian smoothing filtering – to remove noise -, and thresholding – to binarize the images -. As a result, the masks of the rock-in-chip microfluidics channel over time was obtained.
The idea, in fact, was to analyse images distinguishing the rock grains from the pore space. The porosity of the rock-in-chip microfluidics was calculated as the ratio of the void volume – pore space in images – to the total volume – the whole image. By recognizing the circular grains of the porous media in the images, it was possible to calculate the average grain radius and the average pore throat size of the rock-in-chip microfluidics over time. As last step, the hydraulic conductivity according to Kozeny-Carman was evaluated for every image.

Experimental results and discussion

Classic microfluidic hydraulic properties evaluation
Figure 2 shows the interpolation line of experimental data, whose slope was the hydraulic conductivity, of the classic PDMS microfluidic channel. It can be noted that the data was processed: this was done to correct a systematic bias caused by the flow control system, the pressure controller. In fact, it provided a desired pressure to the reservoirs, but it could not control the initial pressure to which it provided the extra pressure. As a result, the pressure difference was not actually null when the pressure controller was imposing the same pressure level to both inlet and outlet reservoirs. It was calculated that the pressure difference which caused the biased was of 4.84 mbar, which was credible to be caused by a different atmospheric pressure into the reservoir. Consequently, the data points were corrected, without influencing the evaluation of hydraulic conductivity.
From experimental data, hydraulic conductivity resulted to be 0.2930 ± 0.0042 mm/s, while from Kozeny-Carman it resulted 0.4605 mm/s.

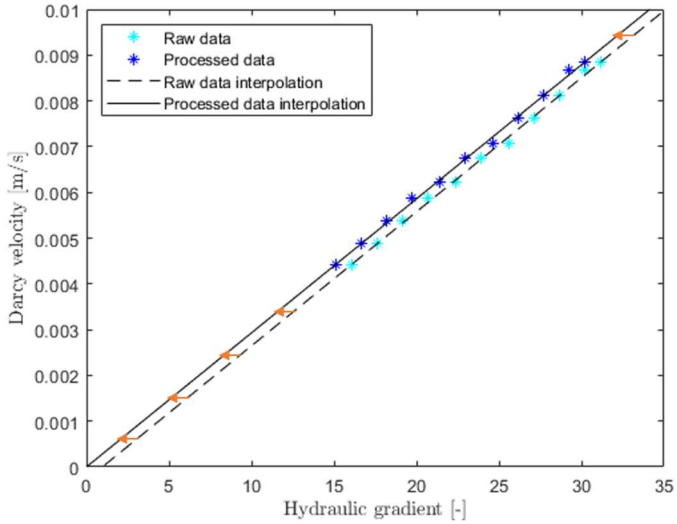

Figure - 2 Linear interpolation for the calculation of hydraulic conductivity

As the two evaluations of hydraulic conductivity was of the same order of magnitude, it was judged that the experimental method applied for the PDMS microfluidic channel allowed to get a good evaluation of the hydraulic conductivity, thus it could be a valid solution for the calculation of the hydraulic conductivity of the rock-in-chip microfluidics.

Particle Image Velocimetry (PIV) on classic microfluidic device

Figure 3 shows the velocity field in the classic PDMS microfluidic device resulting from the PIV analysis. It is clear that there are some preferential paths for the flow, namely the paths coloured in red and dark red. Moreover, the average velocity from PIV analysis was calculated: it resulted to be 0.0051 mm/s. This means that dark red-coloured pathways had a velocity of an order of magnitude higher with respect to the average velocity of the whole area. The average velocity was calculated also from the flow rate imposed by the syringe pump: it resulted 0.0048 mm/s. Therefore, the average velocity obtained from the PIV analysis was very similar to the expected average velocity. Consequently, the PIV analysis method developed was judged to be suitable for the experimentation of rock-in-chip microfluidics, in order to obtain the velocity field during dissolution. Even though the PIV analysis could not be performed, this protocol may be used in similar future experiments.

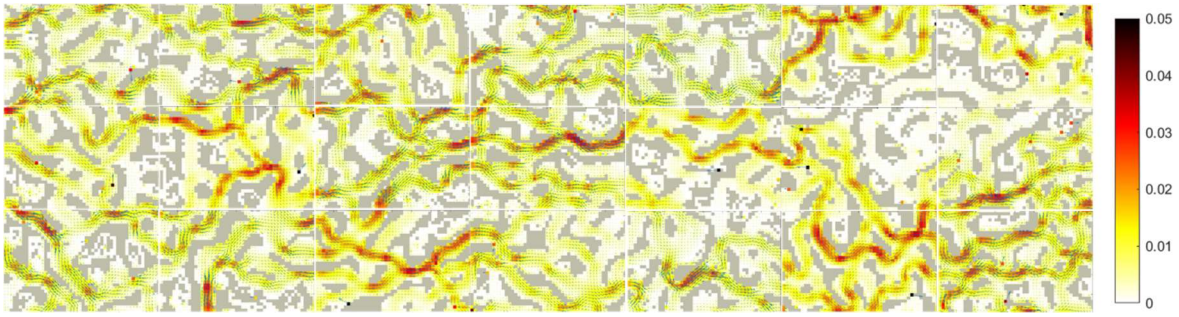

Figure 3 - Velocity field in mm/s in the PDMS microfluidic channel

Rock-in-chip microfluidics experimentation

Figure 4 shows the interpolation line of experimental data, whose slope was the hydraulic conductivity, of the novel rock-in-chip microfluidics. Similarly to the classic PDMS microfluidic device, the data were processed in order to correct the systematic bias which affected the flow control system. In this case, the difference in atmospheric pressure between inlet and outlet reservoirs was calculated to be 4.37 mbar: a plausible difference. Moreover, the data of the first 60 s were excluded from the analysis. In fact, as it can be noted, they had a peculiar trend, probably due to initial instability of the system.

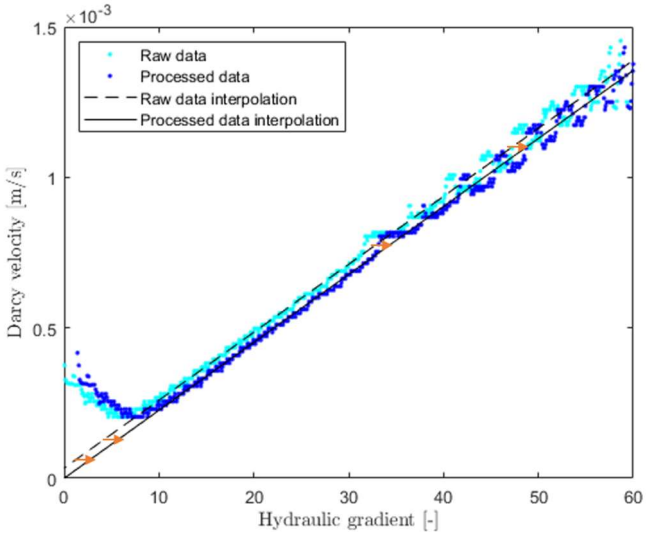

Figure 4 - Linear interpolation for the calculation of hydraulic conductivity

From experimental data, hydraulic conductivity resulted to be 0.0226 ± 0.0001 mm/s, while from Kozeny-Carman it resulted 0.0669 mm/s.

Even though the geometry considered in the Kozeny-Carman model was different from the one of the rock-in-chip microfluidics, the fact that the two evaluations had the same order of magnitude suggested that the developed experimental protocol was successful in assessing the hydraulic conductivity – and thus the permeability – of the novel rock-in-chip microfluidics.

Figure 5 shows the properties of the porous medium which was calculated in order to estimate the effects of dissolution on the porous medium. These properties were average grain radius, average pore throat size, porosity, theoretical hydraulic conductivity according to Kozeny-Carman. The figure illustrates the variation of the porous medium properties over time while dissolution was occurring. However, all the properties exhibited peculiar tendencies, contrasting with the expectations. In fact, after an initial variation – which was, besides, opposed to the trend expected due to dissolution -, each of the properties stabilized to constant values. The explanation to these peculiar behaviours was found in the fluorescein which came out from the working solution. In fact, at the end of the experiment, fluorescein powder was visible both in the inlet reservoir and in the PVC tubing connecting inlet reservoir and rock-in-chip microfluidics. As a result, fluorescein powder partially blocked both the tubing and the rock-in-chip microfluidics channel, thus almost stopping the flow and the dissolution reaction. However, it could be verified that the experimental protocol

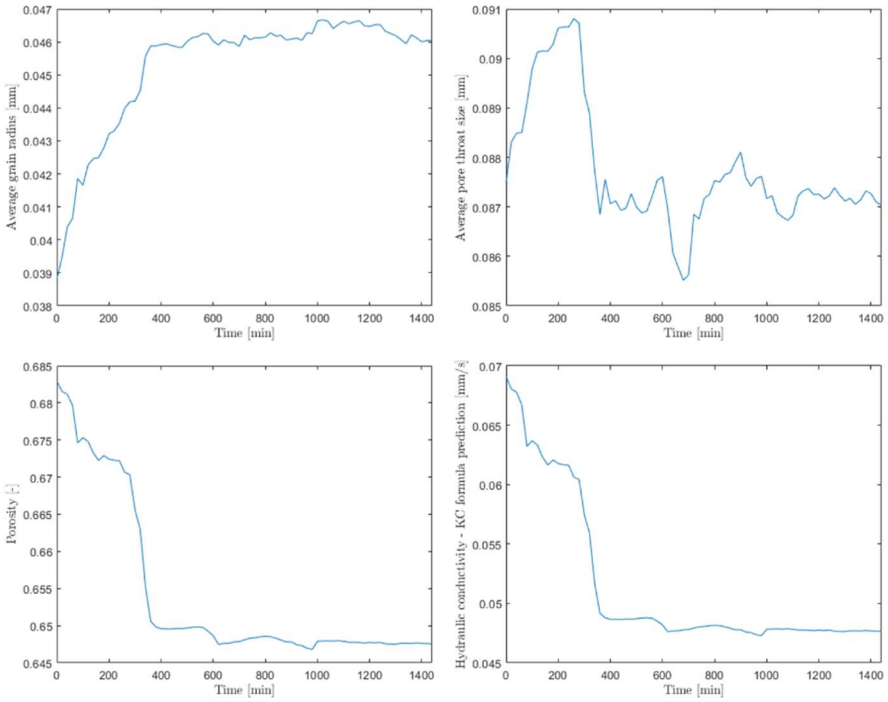

Figure 5 - Porous medium properties over time during dissolution. Top left: average grain radius. Top right: average pore throat size. Bottom left: porosity. Bottom right: theoretical hydraulic conductivity

allowed the quantification of rock dissolution through the evaluation of the variations of the porous medium properties over time.

Moreover, Figure 6 shows two bright-field images of rock-in-chip microfluidics - one acquired at the beginning of the experiment, the other acquired at the end of the experiment – in which, in the highlighted details, dissolution can be observed. In fact, in the second image, the black zones suggest the dissolution of the residual rock layer.

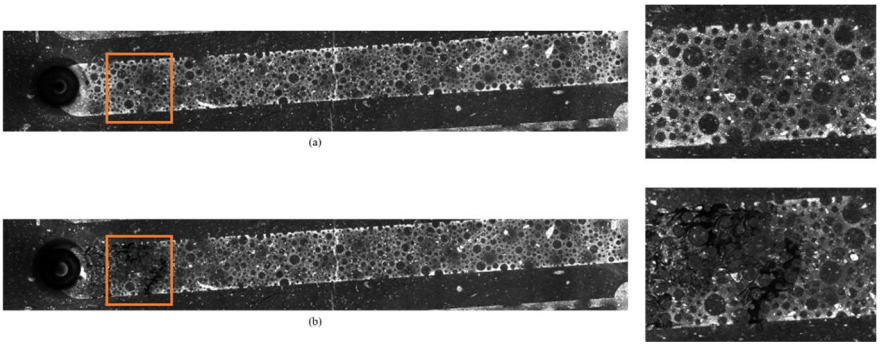

Figure 6 - Bright-field images of rock-in-chip microfluidics and details of a portion. (a) t = 0 min. (b) t = 1440 min.

Conclusions and future directions

This thesis proposed the fabrication and use of a novel microfluidic device: the rock-in-chip microfluidics. In addition, an experimental protocol has been proposed and validated for the use of the novel rock-in-chip microfluidics for the observsation and the quantification of natural rock dissolution. The main feature of the rock-in-chip microfluidics is the designing onto a natural rock surface. In this way, the study of reactive transport phenomena in porous

media can take place in a real porous medium, and not in a medium that mimic a porous medium.
Initially, an experimental setup for the evaluation of the hydraulic conductivity was built and validated for a classic PDMS microfluidic device. Therefore, it was considered suitable also for application with rock-in-chip microfluidics.
Subsequently, a PIV analysis protocol was established for the classic PDMS microfluidic device. The methodology was intended to be applied to the rock-in-chip microfluidics after validation. In fact, it could be useful to compare the velocity field within the porous medium and the preferential zones of dissolution in the rock-in-chip microfluidics. Moreover, the evolution of the velocity field over time due to dissolution could be characterized.
For these reasons, future work on rock-in-chip microfluidics should include the execution of the PIV analysis.
Afterwards, the rock-in-chip microfluidics was characterized in hydraulic conductivity, and the observation and quantification of the dissolution of the porous medium took place.
As a result, it was experienced that

- the experimental setup developed allowed the evaluation of parameters of rock-in-chip microfluidics useful for the study of transport phenomena within porous media

- the employment of image analysis allowed tha observation of rock dissolution and the evaluation of the evolution of the rock-in-chip microfluidics' properties for the quantification of dissolution

The novel rock-in-chip microfluidics has proven successful for the applications tested in this thesis, however some improvements can be made for future applications.
In fact, the rock-in-chip microfluidics manufacturing could be improved in order to avoid to have the residual rock layer. Besides, as fluorescein came out of solution, a different way for the visualization of the flow should be investigated.
Concluding, the novel rock-in-chip microfluidics could be used for the study of reactive transport in porous media; in particular, it could be of interest to study how dissolution of a porous media could be controlled.

Table of Contents

List of Figures

List of Tables

Chapter 1
Introduction

1.1 Introduction to Thesis Work

In the oil and gas industry, the study of reactive transport phenomena in porous media - reservoirs in the subsurface - plays a role of paramount importance. Currently, as much as 50% of the original oil remains in the fields. Therefore, an improvement in oil extraction techniques is necessary and sought. For this purpose, the development of chemical and physical models representing reactive transport in porous media is necessary [1]. The traditional method for conducting studies on porous media used to be the core sample experiments in laboratory. However, these core sample experiments are expensive and time consuming to obtain and operate, as the cores need long times for equilibration. Moreover, the experiments act as a black box, in which the reactive transport processes – occurring at the pore scale – are not allowed to be observed. Nevertheless, the study of processes at the pore scale is crucial for the understanding of physicochemical processes, indispensable for developing the best models possible to be upscaled to a core scale and then reservoir scale. Due to this lack, it is challenging to model the processes that take place at the pore scale in porous media. In order to overcome the problems listed, some technologies are used to obtain a characterization at the pore scale of the core samples, such as neutron radiography, high resolution optical profilometry, magnetic resonance imaging, X-ray computed tomography and synchrotron-based μ-CT. However, these are expensive and complex techniques, which require specialized instrumentation because of the opaque nature of rock core samples [2].
As a result, the use of microfluidic model porous media, also used in other fields of research - such as biomedical - has spread. Microfluidics is a scientific discipline that studies movement, handling and manipulation of liquid substances in microvolumes across micro-scales. Microfluidic model porous media are devices in which the observation of the phenomena occurring inside, at the pore scale, is possible due to their transparency to light, as opposed to real porous media. The observation at the pore level is possible by coupling the employment of transparent micromodels with a microscope and a camera. The micromodels can be produced both with nonorganic and polymeric materials.
Glass and silicon are two nonorganic materials used for the fabrication of micromodels. Because of their stiffness, glass and silicon are suitable for experiment at high pressures. Moreover, they can withstand high temperatures, making them adequate for harsh environment experiments. Besides, it is easy to modify the surface wettability, which is important to study the effect of wettability on porous media flow. Silicon micromodels are

usually bound to a glass plate to make possible the visualization of the internal flow, as silicon is not transparent for visible light.
Polymer materials for micromodels fabrication are characterized by optical transparency and low cost of fabrication. Polydimethylsiloxane (PDMS) and poly(methyl methacrylate) (PMMA) are the most common polymers employed for microfluidic models fabrication. PDMS is an elastomer that is ideal for rapid replication by soft lithography and molding. Moreover, it can be easily bound to glass, making its employment very simple. However, it cannot be used for every application as it swells in contact with nonpolar solvents. PMMA is a thermoplastic material used for fabrication of microfluidic models. It has to be taken into account that it can be dissolved by many organic solvents, such as ethanol and acetone.
These material have different properties, which make them suitable for different applications [8].
The fabrication of microfluidic models can be carried out with different methods, depending on the material with which the microfluidic device is produced. It can be divided into three main technologies: non-additive manufacturing, additive manufacturing and particle packing.
Almost all non-additive manufacturing methods follow two steps: (1) lithography, in order to transfer the geometric pattern of the microfluidic model from a mask to a photoresist layer on the substrate; (2) shaping, in order to give a shape to the microfluidic material. The most common lithography technique is photolithography, which employs ultraviolet light to transfer the pattern to the photoresist. Instead, several methods are used for the shaping. When microfluidic models are made of glass or silicone, the substrate on which the photoresist is deposited is the microfluidic model itself: in this case, the shaping takes place by etching. The etching involves the removal of the unprotected material from the photoresist layer, in order to obtain the desired geometry. The etching may be of two types: (1) "wet etching" when chemical solutions are used; (2) "dry etching" when the material is exposed to plasma of reactive gases.
Another method for shaping is replica molding, which is used for polymer materials. It involves the employment of a mold, which is the negative of the microfluidic model geometry. The mold is filled with the prepolymer material, which is then crosslinked and unmolded. Subsequently, the micromodel geometry is bound to a glass plate in order to complete the microfluidic device. PDMS microfluidic devices are mainly manufactured with this technique: the mold is produced by photolithography and, subsequently, the microfluidic model is fabricated by replica molding. This technique is also called "soft lithography". The main advantage of this technique is that the mold can be used many times to manufacture identical microfluidic models in a short time, resulting in a less expensive technique.
Two other non-additive manufacturing techniques are laser engraving, in which the pattern is engraved directly onto the substrate using laser technology, and hot embossing, used for thermoplastic polymers, such as PMMA.
Additive manufacturing is based on solidification of liquid or melted materials placed in layers, in order to create the desired structure. Stereolithography is the most common type of additive manufacturing.
Particle packing technique is used for glass microfluidic models, fabricated by packing glass beads between two parallel transparent plates [8].

A more detailed treatment of microfluidic model manufacturing methods can be found also in [9] and [10].
The most suitable visualization method varies depending on the purpose of the experiment for which a microfluidic model mimicking a porous medium is used. Commonly, the visualization of microfluidic experiments involves the employment of a camera coupled to a microscope. This setup is suitable when the interest is on focusing on a specific area of the microfluidic channel at a high resolution. If the focus is on the study of rapid events, high-speed cameras are employed.
Another setup involves the use of a camera – or multiple cameras – without the microscope. This setup is suitable for experiments requiring a large field of view or for experiments with high acquisition rates. Lower-resolution images are obtained since the microscope is not employed in this setup.
When three-dimensional imaging is required or experiments with high-resolution requirements are performed, confocal microscopy is employed. Confocal microscopy allows the visualization of slow displacements over a length scale less than the optical diffraction limit. Moreover, this setup provides images over the depth of the chip, up to 250 μm.
Fluorescent microscopy is employed for the visualization of different fluid phases or fluorescent particles added to the flow, using a light source to excite the fluorescent molecules. The convenience of fluorescent microscopy lies in the ease of use and the low detection limit.
One optical technique used for measuring the velocity of fluids is particle image velocimetry (PIV). This technique is used to evaluate fluids velocity by measuring the average displacement of tracer particles between two images captured at successive instants of time, with a time delay Δt. Fluorescent tracer particles are employed in order to increase the signal-to-noise ratio in images [11].
Raman spectroscopy is used to measure the vibrational modes of molecules, in order to derive molecule-specific information at the microscale. Coupling the Raman spectroscopy with microfluidic experiments could provide information about miscible and immiscible fluids. [9]
A more in-depth discussion of the visualization techniques of microfluidic devices, also applied to different fields of study - such as the biological field - can be found in [12].
Microfluidic devices produced as mentioned have been used for evaluating properties of porous media [13], for characterizing processes for secondary production [14] and EOR processes [15].
The fabrication of microfluidic devices allows the production of microfluidic channels that mimic a porous medium for geometry and topology, making it possible to perform studies at the pore scale. However, the physical and chemical complexity of real porous media is not reproducible by using materials that have been mentioned above.
To partially overcome this problem, Alzahid et al. (2018) [3] have functionalized a PDMS microfluidic device by coating the pore space of the microfluidic chip with rock minerals. They functionalized two distinct microfluidic devices with two different types of rock: sandstone and carbonate. In order to obtain the functionalized microfluidic device, they peeled off the PDMS channel from a silicon mold and treated it with oxygen plasma. Immediately after the plasma treatment, 1 ml of the mineral solution – one of quartz and kaolinite to simulate sandstone rock and one of calcite for carbonate rock – was placed on

top of the PDMS slice. Then the PDMS slice was air-dried, cleaned and bounded to a blank PDMS cover with a plasma treatment in order to seal the microfluidic channel. As a result, after comparing the functionalized PDMS microfluidic devices to representative rocks, they obtained microfluidic models with height profile and surface roughness similar to those of the rocks. Although this type of microfluidic model is better for representing a porous medium, it does not allow a complete study of a reactive transport process, since the reactions between porous medium - whose structure remains mainly of PDMS - and fluid cannot be studied in their completeness. In fact, this microfluidic model does not allow a study on the dissolution of rock in a porous medium.

An analysis of calcium carbonate ($CaCO_3$) dissolution within a porous medium in a microfluidic device was carried out by Yoon et al. (2019) [4]. However, they employed a silicon microfluidic device, thus they could not study rock dissolution directly. In fact, they injected two influent solutions of calcium chloride ($CaCl_2$) – pH was 6 – and sodium carbonate (Na_2CO_3) – pH was 11 – into the microfluidic channel, each solution into a separate inlet. As a result, $CaCO_3$ precipitated in the microfluidic channel. The precipitation phase continued for 75 h. Subsequently, a solution made up of water and HCl – pH was 4 – was injected into both inlets, resulting in the dissolution of $CaCO_3$, which lasted about 150 h. During both precipitation and dissolution phases images were acquired with a CCD camera – for two-dimensional analysis – and laser scanning confocal microscope – for three-dimensional analysis – at selected time intervals. Images were processed and analysed in order to quantify the change of two and three-dimensional reactive surface area over time and to evaluate how to estimate precipitation and dissolution reaction rates in a micromodel. Images were analysed to study the precipitation in multiple pores, the dissolution in multiple pores, the precipitation and the dissolution in a single pore, and reaction rates. Image analysis results were compared with results obtained with a two-dimensional pore scale reactive transport model, modified in order to simulate the experimental conditions.

As a result, they found that the two-dimensional expression for reaction rates in the pore scale model oversimplified the local reactivity early during precipitation and late during dissolution, because of the complexity of flow at such times. However, they concluded that a microfluidic device with controlled mineral surface – a calcite chip – would have been essential for the study of dissolution reactions in a controlled hydrodynamic system.

Few examples of such a microfluidic device can be found in literature. For example, Singh et al. (2017) [2] constructed a real rock microfluidic model, starting from a sandstone core. From the sandstone core they obtained a 500 μm-thick real rock wafer to be used for a microfluidic device. The rock wafer was placed in a 5 mm PDMS layer with a channel to land the wafer. The microfluidic chip was sealed with a 0.2 mm PDMS layer. Liquid PDMS was poured in order to seal the lateral walls of the rock wafer. The assembly was put into an aluminum-plexiglass manifold in order to seal the device during operation. These two plates were connected by screws and tightened to press together the PDMS layer. They performed flooding tests with the real rock microfluidic device, acquiring images with bright-field microscopy, fluorescence microscopy and confocal laser scanning microscope. However, due to the thickness of the opaque rock wafer, they could acquire images of only half of the rock wafer. Besides, the liquid PDMS - used to seal the channel – invaded the rock wafer for 2-4 mm from the edges of the PDMS microfluidic channel, creating a non-uniform boundary for the flow.

In the present work, a novel type of natural rock microfluidic device will be presented: a rock-in-chip microfluidics device. In addition, an experimental and analysis protocol to determine the properties of the porous medium and to evaluate the variations of those properties caused by the dissolution of the rock will be presented. The aim was to develop a device that was able to allow an analysis as complete as possible of what happens at the pore scale during a reactive transport process. A feature of the rock-in-chip microfluidics device presented herein is that it was etched in such a way to construct a microfluidic channel - which mimicked a porous medium - with a geometry similar to the one of the classic microfluidic channels, but made of natural rock, in order to represent both the physical and chemical complexity of a porous medium, overcoming the limitations of classic microfluidic devices. The use of the rock-in-chip microfluidics device was coupled to image acquisition and analysis in order to carry out the intended evaluations of the study.
Some further tests anticipated the experimentation of rock-in-chip microfluidics. Initially, a classic PDMS microfluidic device was characterized in hydraulic conductivity, validating an experimental protocol to be applied to the study of rock-in-chip microfluidics. At a later stage, a PIV analysis was performed for the characterization of the velocity field within a PDMS classic microfluidic device. The experimental protocol validated for PIV analysis was to be applied to the rock-in-chip microfluidics device, to have an additional tool for analysing rock dissolution. Finally, the testing of rock-in-chip microfluidics was performed.
The work is organized as follows. In the next paragraph physics of microfluidics will be briefly introduced. Chapter 2 will describe the materials employed during the experimental phase. Chapter 3 will describe the experimental and analysis methodologies and protocols followed. Chapter 4 will present the results obtained. Chapter 5 will outline the final conclusions and future directions of this study.

1.2 Introduction to Physics of Microfluidics

This section will briefly outline the physical characteristics of the flow within a microfluidic channel. What is proposed refers to [16] [17] [18] [19] [20].
The main properties of the fluids used during the experiments that will be proposed were:

- Newtonian fluids. A Newtonian fluid is a fluid whose viscosity can be considered independent on the shear stress and fluid velocity. This means that the ratio of the shear stress to the shear rate is constant.

- incompressible fluids. An incompressible fluid is a fluid with a density ρ that is constant in space and time, whereas a compressible fluid is a fluid with a density ρ that varies as a function of space and time. The incompressible flow can be expressed as

$$\frac{D\rho}{Dt} = 0 \tag{1.1}$$

where *D* stands for the material derivative.

As a consequence, the continuity equation is

$$\nabla \cdot \boldsymbol{v} = 0 \tag{1.2}$$

- Laminar flow. To determine whether a flow is laminar or turbulent it is necessary to consider the Reynolds number, which expresses the ratio of inertial forces to viscous forces

$$Re = \frac{\rho v L}{\mu} \tag{1.3}$$

where ρ is the fluid density, v is the velocity, L is the characteristic linear dimension and μ is the fluid dynamic viscosity. In fact, a flow is laminar for Re < 2000 and is turbulent for Re > 4000. In a microsystem with a characteristic linear dimension of 100 μm (for excess), and filled with water ($\mu = 10^{-3}$ Pa·s, $\rho = 1000$ kg/m^3) running with a velocity of 1 cm/s – which is a high velocity for a microfluidic flow -, it results Re ≈ 1, which is far in the laminar regime. In general, it can be considered that the flow is always laminar in microsystems.

Newton's second law for fluid particles is called the Navier-Stokes equation. In case of incompressible fluids, the Navier-Stokes equation results in

$$\rho(\partial_t \boldsymbol{v} + (\boldsymbol{v}\nabla)\boldsymbol{v}) = -\nabla p + \mu \nabla^2 \boldsymbol{v} + \rho g \tag{1.4}$$

where $\boldsymbol{v}$ is the fluid velocity and p is the fluid pressure.
The Navier-Stokes equation is notoriously difficult to solve analytically because it is a non-linear differential equation. Analytical solutions can however be found in a few, but very important cases. In particular, an important solution to the Navier-Stokes equations is the Hagen-Poiseuille flow, which applies when the fluid is driven through a long, straight, and rigid channel by imposing a pressure difference between the two ends of the channel. For a circular cross-section it results

$$Q = \frac{\pi R^4}{8\mu L}\Delta p \tag{1.4}$$

where R is the radius, and L is the length.
The Hagen-Poiseuille flow will be employed in the analysis that will be presented.

Chapter 2
Materials

This section will present all the materials used during the experimental work. Since not all of them have been used at every stage of the work, in the section dealing with the methods (Section 3) the materials in use at each stage will be recalled.

2.1 Microfluidic Devices

The microfluidic device was the main part of the experimental system employed, being the medium through which the fluid flowed. Two different types of microfluidic devices have been used:

- polydimethylsiloxane (PDMS) microfluidic device
- rock-in-chip microfluidics device

The PDMS microfluidic device is the most widely used in scientific research, on the other hand, the rock-in-chip microfluidics is a new technology; for this reason, there is no material in literature for fabrication or experimental use.
Rock-in-chip microfluidics is the main element of innovation that has been tested in the course of the proposed work.
Both the microfluidic devices had microfluidic channels which mimicked a porous medium.

2.1.1 PDMS Microfluidic Device

PDMS microfluidic devices are widely used in several scientific fields, so for its manufacturing the most common method reported in the literature was followed [5]. This method will be illustrated in the current paragraph.
The first step was to mix the base, a silicone elastomer, and the curing agent in a 10:1 ratio in order to produce the PDMS in an optimal composition: using a ratio other than the one suggested in literature could lead to the production of a PDMS with a wrong compactness, bringing to the possibility of PDMS breaking at a later stage. Afterwards the mixture was mixed and placed to degas in a vacuum desiccator, in order to eliminate the air bubbles, present inside; the degassing process took about 45 minutes.

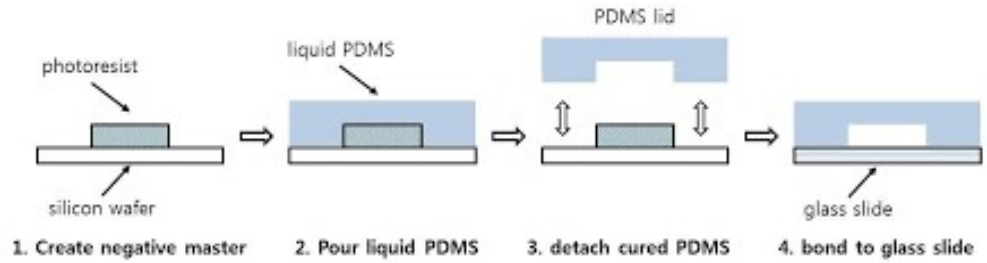

Figure 2.1 - Scheme of PDMS microfluidic device fabrication

Once the PDMS had been degassed, it was poured into a silicon mold that contained the negative of the desired channel to replicate the channel via soft lithography, taking care to eliminate all possible residual air bubbles. The master filled with the PDMS was placed in the curing oven at 60°C for a minimum of 4 hours.
Once the necessary time had elapsed in the oven, the most delicate operation of the microfluidic chip fabrication was managed: the unmolding from the master of the desired PDMS channels. A small knife was used to cut the section of PDMS with microfluidic channel that had to be employed, with the aim of unmolding it. This operation had to be necessarily performed slowly and carefully so as not to break the PDMS and consequently damage the microfluidic channel.
The device required to have an inlet and an outlet in order to connect the microfluidic channel to a hydraulic circuit, thus two holes were punched with a needle in the PDMS in correspondence with the inlet and the outlet sections of the microfluidic channel. Since the connection between the microfluidic channel and the hydraulic circuit was made with PVC tubings with an internal diameter of 0.5 mm, the hole had to have a diameter such as to allow the tubing to enter but not so large as to allow the fluids to escape. A needle with a 1.2 mm tip was used for this purpose.
To finish the manufacturing of the device it was needed to bond the PDMS channel already cut to a glass slide. In order to achieve this, the glass slide was cleaned with ethanol to avoid including impurities inside the chip; then both the glass slide and the PDMS had to be subjected to plasma treatment. Plasma treatment of PDMS increased the exposure of silanol groups (-OH) at the surface of the PDMS layers so that they could form strong covalent bonds (Si– O–Si) when brought together with treated glass. These covalent bonds formed the basis of a practically inseparable seal between the layers. Figure 2.1 shows schematically how these steps were accomplished. A final operation was required before the microfluidic device could be ready to be used: the device needed to be placed on a heater at 100°C for 30 minutes. After this phase, the fabrication of the microfluidic was over. Figure 2.2 shows a PDMS microfluidic device ready to be used.
The dimensions of the microfluidic channel were as follows:

- width 7 mm
- length 51 mm
- height 50 μm.

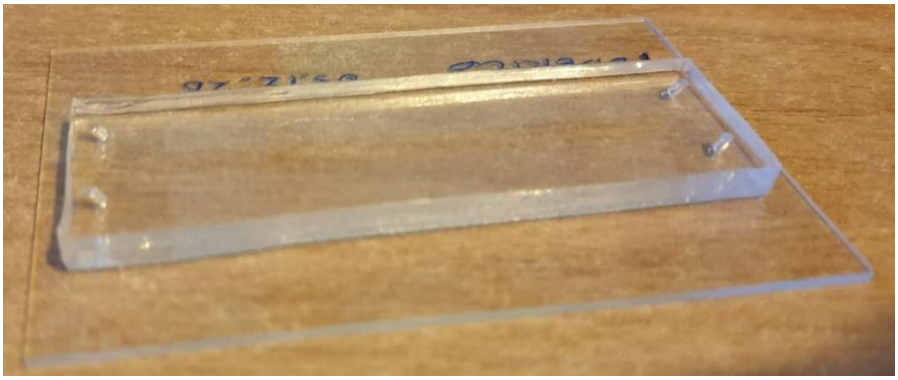

Figure 2.2 - PDMS microfluidic device

The used microfluidic channels modelled porous media; two different geometries of PDMS microfluidic channel were employed:

- channel with circular grains with variable diameters, with average diameter 0.13 mm (Figure 2.3)
- channel with a complex geometry created by grains (Figure 2.4)

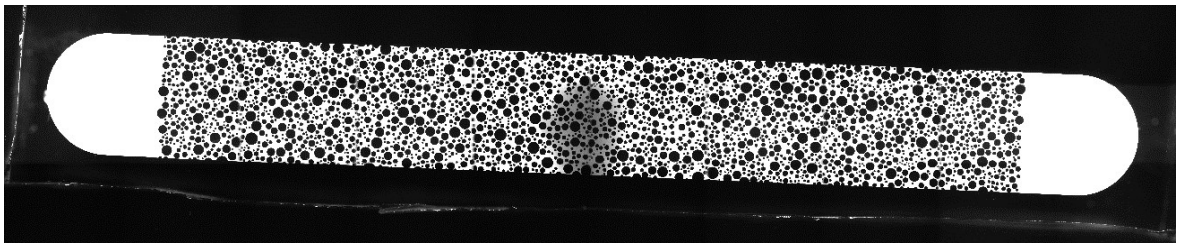

Figure 2.3 - Circular grains microfluidic channel. Fluorescence image acquired by microscope

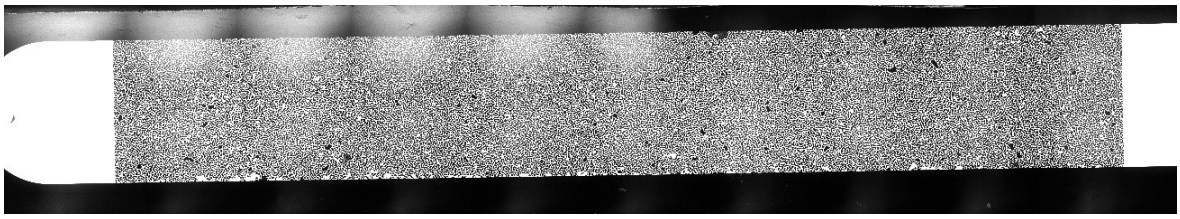

Figure 2.4 - Complex geometry microfluidic channel. Fluorescence image acquired by microscope

2.1.2 Rock-in-chip Microfluidics Device

The use of microfluidic devices in PDMS allows to study the flow of a fluid within a porous material at the pore scale. However, the PDMS can only mimic the geometry of a porous medium but cannot replace its reactive behaviour. In order to study, therefore, the reactive transport at the pore scale, it is necessary to move towards the use of different materials.

For this reason, it was decided to create a microfluidic device designed onto a natural rock surface, in order to further expand the studies on a porous medium that could be carried out with a microfluidic device.
However, in the literature it was not available a technique for the manufacturing of such a device and, as its manufacturing required skills that were beyond the knowledge of the author, the rock-in-chip microfluidics (Figure 2.5) was manufactured at the laboratory of the *Aix-Marseille Université* in Marseille with a novel use of already known techniques.
For the fabrication of the microfluidic device, it has been chosen to use calcite ($CaCO_3$): a slice of rock of the thickness of some mm has been cut from a block of calcite in order to be subjected to the successive workings for the fabrication of the chip.
The chip was fabricated as follows: photolithographic patterns were obtained by spin-coating a positive, photosensitive resist exposed to a near-UV laser (375 nm wavelength, fluency of about 2.7 mW) on a spot of about 2 μm (Dilase 250, from Kloe). The exposed portions of the resist were removed with a developer. The rock was then etched dipping them for 15 minutes in a solution of 1 ml of nitric acid (HNO_3) in 99 ml of deionised water. After the rock was etched, it was attached to a glass slide so that it would serve as the bottom base of the microfluidic channel.

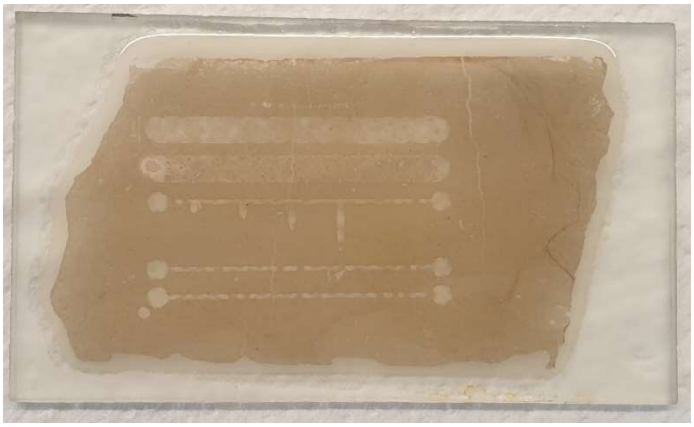

Figure 2.5 - Rock-in-chip microfluidics

From Figure 2.5 it is visible that 5 microfluidic channels with different geometries have been realized; from the top to the bottom of the figure:

- straight empty channel
- porous medium channel composed of circular rock grains
- small straight empty channel with 4 lateral channels
- straight channel with circular pillars
- straight channel with circular pillars

Nevertheless, the only channel used for the studies presented in this paper was the porous medium microfluidic channel composed of circular grains (Figure 2.6).

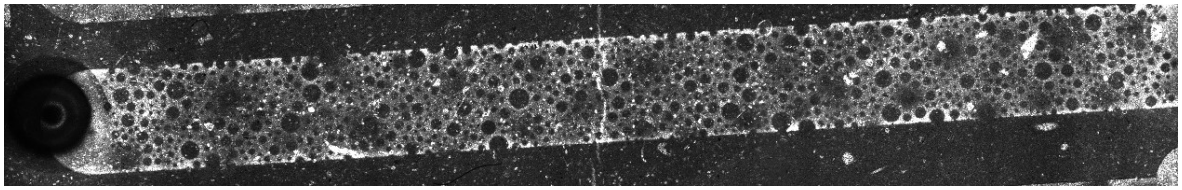

Figure 2.6 - Porous medium channel of rock-in-chip microfluidics. Bright field image acquired by microscope

Although the presented micromodel geometry was quite simplified in comparison to a real carbonate rock, it was sufficient to demonstrate the validity of the technique used and the possibility of carrying out reliable experimental measurements with the apparatus constructed.
The dimensions of the porous medium microfluidic channel used in the experiment were as follows:

- width 2 mm
- length 30 mm
- height 40 μm

After obtaining the rock-in-chip microfluidics, it was necessary to seal the upper part of the channel in order to prevent the injected fluid from leaking from the channels under investigation, which would have compromised the experimentation. Figure 2.7 shows the sealing and clamp system that was adopted; it consisted of:

- 2 screw clamps
- glass slide
- smooth PDMS layer, without any geometry, about 2 mm thick
- approximately 2 mm thick poly(methyl methacrylate), also known as plexiglass, layer

The glass slide was placed at the base, leaning against the lower part of the clamps. In fact, in order to lock the device, the screws of the clamps had to be tightened, applying a force to the base layer. Aiming to avoid stressing the rock-in-chip microfluidics' glass, the glass slide was positioned at the base. The rock-in-chip microfluidics was placed between the glass slide and a PDMS layer. A layer of PDMS was chosen to seal the microfluidic channel: in fact, thanks to its elasticity, PDMS could adapt to the rock geometry to seal the microfluidic channel, even if the rock did not have a constant thickness throughout the rock-in-chip microfluidics. However, due to its elasticity, after closing the clamps on the sides the PDMS would have deformed, bending in the center and failing in its purpose of sealing the microfluidic channel. To solve this problem, a layer of plexiglass was placed above the PDMS: the rigidity of the plexiglass, in fact, prevented the PDMS from deforming, ensuring an adequate sealing of the microfluidic channel. After placing all the necessary layers to properly seal the microfluidic channel, the screws of the clamps were tightened to lock the device.

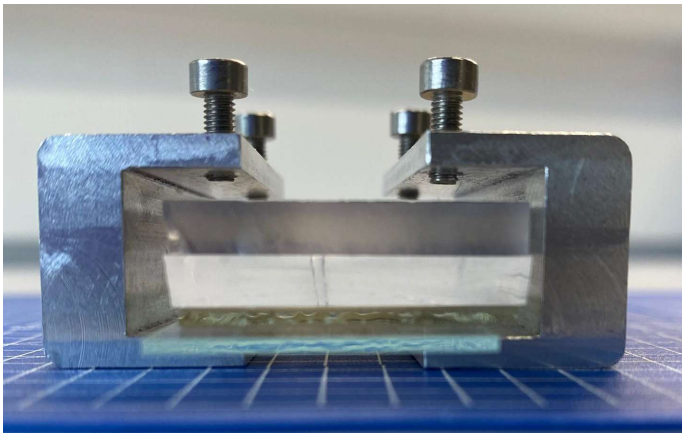

Figure 2.7 - Rock-in-chip microfluidics device with sealing system

Both the PDMS layer and the plexiglass layer had been worked in such a way as to allow the connection of PVC tubings to the inlet and outlet sections of the microfluidic channel, in order to connect the rock-in-chip microfluidics to a hydraulic circuit.
Two holes were punched in the PDMS layer at the inlet and outlet sections with a needle with a 1.2 mm tip, using the same technique described in Section 2.1.1 for PDMS microfluidic device. In this case, however, the operation was more complicated because the microfluidic channel was in the rock-in-chip microfluidics, not in the PDMS itself, therefore the holes to be punched in PDMS had to be aligned to the inlet and outlet sections of rock-in-chip microfluidics, in order to fit the PVC tubing connections.
The plexiglass layer was drilled at the inlet and outlet sections of the microfluidic channel with a milling machine; in the case of plexiglass, it was not necessary to take care of the size of the hole because it had the sole purpose of allowing access to the underlying layers. In addition, a fitting space for the screws of the clamps had been milled on the plexiglass in correspondence with their position to facilitate the locking of the device.
It should be noted that, before starting the assembly of the device, both the rock-in-chip microfluidics channel and the PDMS layer used had been degassed for about 30 minutes in a vacuum desiccator, in order to remove the air inside. For this reason, the assembly had to be carried out quite quickly, in order to be able to saturate with the working fluid the microfluidic channel before it filled with air again.
The microfluidic device created was tested by injecting a mixture of water and fluorescein concentrated at 3 mg/l and verifying under the microscope in real time with fluorescence vision that:

- the fluid did not leave the microfluidic channel
- the fluid did not flow between the grains of the channel and the layer of PDMS that closed the microfluidic channel from above

After verifying the functioning of the microfluidic device, it was ready for experimental use.

2.2 Working Fluids

During the experimental work, three different working fluids were used. The selection of the fluids was based on the analysis activities that should have been carried out on the data collected during the experiments conducted. When the experimentation activity involved the use of the microscope to acquire images to be analysed, a fluorescent component was used to allow visualization by exploiting fluorescence. The working fluids that have been used are described below.

2.2.1 Working Fluid for PDMS Microfluidic Device

For the measurement of the hydraulic properties of the microfluidic device it was not necessary to use the microscope followed by an analysis of the images, therefore the working fluid used for the experiment was Milli-Q water, since a fluorescent component was not required in the working fluid. Milli-Q water was chosen because the PDMS does not swell in contact with it, so the microfluidic channel would not have been deformed during the experiments.

2.2.2 PIV Solution

As it will be described later in this paper, to be able to use the images acquired under the microscope and carry out a Particle Image Velocimetry (PIV) it was necessary to use a fluid that contained within its own - as tracers - some elements easily detectable in the images taken. For this reason, the working fluid used was a suspension containing water - as continuous phase - and fluorescent beads with a diameter of 1.1 μm - as dispersed phase -. The preparation of a suitable working fluid was elaborate because the beads used had a density of about 1.05 g/ml, different from the density of the Milli-Q water, which was 1 g/ml. Using Milli-Q water only, the densities of water and tracer particles would not have matched, deriving in a gravitationally induced velocity (U_g) from Stokes' drag law. Assuming spherical particles in a viscous fluid [16], it yields

$$U_g = d_p^2 \frac{(\rho_p - \rho)}{18\mu} g \tag{2.1}$$

where g is the acceleration due to gravity, μ is the dynamic viscosity of the fluid and d_p is the diameter of the particle.
To prevent this from happening, it was chosen to level off the densities of beads and fluid, adding heavy water. For this purpose it was necessary to consider the ratio in volume between a first suspension of (1) Milli-Q water and beads and (2) heavy water; to match the densities the volume ratio was 1 ml : 852 μl. Therefore, initially a starting suspension of Milli-Q water and beads had to be produced. However, it should be noted that in the preparation of this suspension it was necessary to decide on the concentration of particles to be used; in fact, it had to be high enough to be able to perform the PIV analysis, as it will be explained in Section 3.2. Furthermore, it had to be considered that the initial suspension would have been diluted subsequently with heavy water. Given this, a suspension was

produced by combining 1600 µl of beads and 20 ml of Milli-Q water, so as to have a ratio between particles and Milli-Q water of 1/12.5. The suspension obtained was mixed with a vortex to ensure that the particles dispersed evenly. Later, 1 ml was taken from this first suspension and diluted with 852 µl of heavy water to match the densities. As a last step before use, the suspension was sonicated for 20 minutes to keep the fluorescent beads in suspension.

2.2.3 Rock Dissolving Solution

The rock dissolving solution was used as a working fluid to be injected into the rock-in-chip microfluidics described in Section 2.1.1 to verify its dissolution through the images acquired by the microscope.
For this reason, the solution to be selected had to have two very precise characteristics:

- be clearly distinguishable by the microscope
- be able to dissolve the rock

The first requirement was met by a solution of Milli-Q water and fluorescein concentrated at 3 mg/l. In this way, in fact, it was possible to use the fluorescence of the solution to obtain images under the microscope that emphasized the structure of the microfluidic channel. This was fundamental for the evaluation of the possible dissolution of the rock, which is a non-fluorescent element, during the experiment. The non-fluorescence feature of the rock was important because it could be identified in contrast to the fluorescent working fluid.
Regarding the need to dissolve the rock, research had been carried out in the literature in order to select the most suitable element for the purpose [21] [22]. The literature review led to the choice of acetic acid to dissolve carbonate rock; however, to select the appropriate concentration of acetic acid to be used it was necessary to proceed with an experimental test. Table 2.1 shows the concentrations of acetic acid in Milli-Q water that was tested, and the pH of the solutions, measured with a litmus paper.

Table 2.1 - Concentration and pH of acetic acid solutions tested

Sample	Concentration	Measured pH
1	1:1000	2.5
2	1:4000	3.5
3	1:10000	4
4	1:40000	4.5
5	1:100000	5

The most concentrated solution that was tested was 1:1000 because it was wanted to avoid using solution with a pH too acidic, because too risky to be handled. Moreover, the choice of the solution was not conditional on compliance with a specific predetermined condition, since the main focus of the work was on the establishment of an experimental protocol aimed to the development of a new type of experiment; not on the characterization of rock

behaviour in a predetermined situation, for which further consideration about the acidity of the solution should have been developed.
The test was conducted by immersing fragments of the carbonate rock - of which rock-in-chip microfluidics was composed - in each of the tested solutions, verifying the variation of the mass of the fragments at intervals of about 60 minutes.
Figure 2.8 shows the results obtained as mass to initial mass ratio, as a function of time. In the end, the solution chosen was the 1:1000 concentration solution because it was the one that showed the most convincing results. In fact, the figure shows a different trend for the mass to initial mass ratio of samples 1, 3, 5 compared to samples 2 and 4, which apparently seemed the best dissolving solutions. Nevertheless, regarding rock sample 2, it provided incomplete data as the test fragment broke during the test, not providing results that could have been taken into account. Rock sample 4 did not present this problem, at least in appearance, however it was noted that in two distinct phases of the test it suffered a considerable decrease in mass; this behaviour was not in accordance with the average trend that followed during almost all of the test. For these reasons, solutions of acetic acid and Milli-Q water referred to samples 2 and 4 were discarded. Given these considerations, the choice has therefore fallen on the 1:1000 concentration solution since it was the most dissolving solution between the tested ones, and, in the meanwhile, it was estimated that the rate of dissolution of the rock immersed in that solution was not too high to perform the experiment in a proper manner.

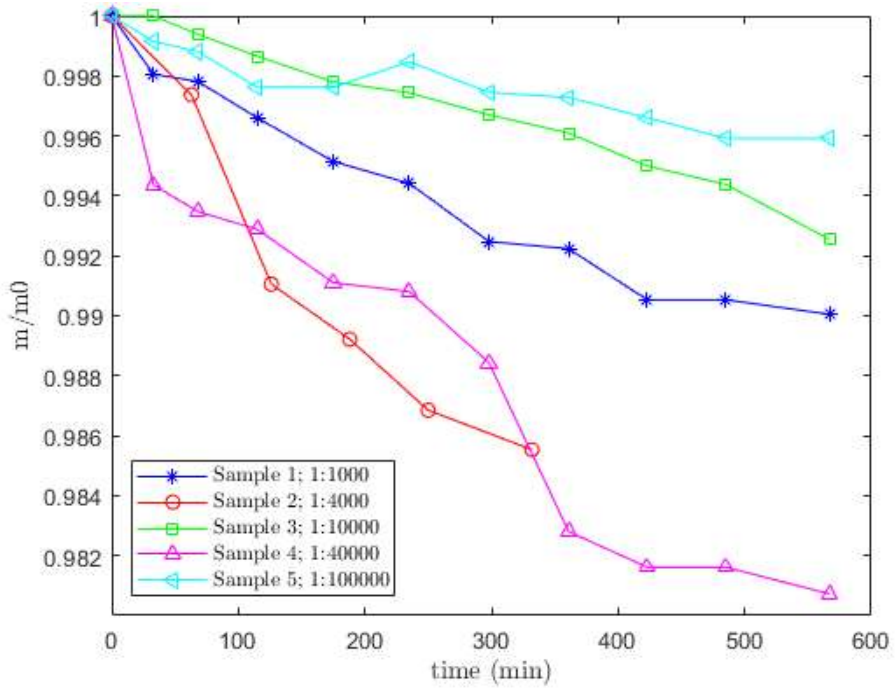

Figure 2.8 - Mass to initial mass ratio over time of rocks immersed in different acid solutions

As a last step in the preparation of the working fluid, 800 µl of fluorescent beads were added to 20 ml of the solution of Milli-Q water, fluorescein and acetic acid. At this point, the suspension was sonicated for 20 minutes to disperse the particles homogeneously.
Note that fluorosceine was fluorescent to yellow light, while fluorescent particles were fluorescent to red light: in this way it was possible to focus on the total flow or particles by changing the filter for light.

2.3 Flow Control Systems

During the work carried out, two different flow control systems were used:

- syringe pump
- pressure controller

The conceptual difference between the two systems was that the syringe pump allowed to set a flow rate to the system, while the pressure controller allowed to impose a pressure difference between inlet reservoir and outlet reservoir.

2.3.1 Syringe Pump

The syringe pump allowed to impose a desired flow rate. In the course of practical work, a programmable 5 ml syringe pump from Harvard Apparatus was used (Figure 2.9).

Figure 2.9 - Syringe pump

2.3.2 Pressure Controller

Figure 2.10 shows the flow control scheme using an Elveflow OBI1 Mk3 pressure controller connected to the Elveflow Software Interface (ESI) control software.
An external pressure source was connected to the device. Through the ESI interface two different pressure values were set at the inlet reservoir and at the outlet reservoir, generating a pressure difference between them; the pressure chosen was imposed by injection of air

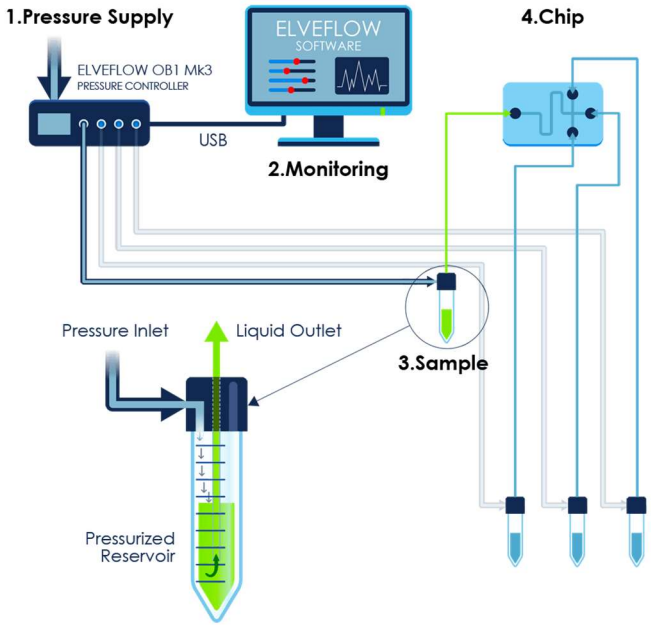

Figure 2.10 - Microfluidic flow control scheme with pressure controller

through a PVC tubing that connected the pressure controller to the reservoir to be pressurized. The maximum pressure applicable with this device was 200 mbar.
It should be noted that the pressure controller did not have a pressure detection system, so it merely provided an extra pressure level to a closed reservoir, without being able to control the actual pressure level present in the reservoir itself.
Since the ESI interface works with the pressure in mbar, during this written paper mbar will be used as a unit of measurement for pressure when referring to the use of the pressure controller, to remain aligned with what was performed from the practical point of view. However, when the results will be presented, the pressure values will be reported in Pa, as required by the SI.

2.4 Scale

The mass of the test samples was measured with the analytical balance Fisherbrand™ Analytical Balance, equipped with sliding doors to protect the measuring environment from external disturbances. The data obtained from this device was recorded and stored for subsequent analysis thanks to USB and RS232 connectivity for communication and download of data on a PC. The most useful characteristics owed by the balance were the time interval between two successive measurements of 1 s and the readability of 0.1 mg.

2.5 Visualization system

The visualization systema consisted of a camera mounted on a microscope. The microscope was used in order to observe and analyse what was happening in the microfluidic channel. In particular, the Nikon Eclipse Ti microscope (Figure 2.11) was used, a motorized inverted

Figure 2.11 - Microscope

microscope, particularly suitable for the activity carried out, based on the use of time lapse images. The microscope was equipped with several objectives - in a range of magnitude from 2x to 40x - and with filters cubes, in particular to acquire bright field and fluorescence images, useful for the analysis carried out in the course of the study. A SOLA light source was used to capture fluorescence images.
The images were acquired using cameras mounted on the microscope. For this purpose, two different cameras were used:

- Nikon DS-Qi2
- Hamamatsu ORCA flash 4.0 V3

The two cameras had different characteristics regarding

- pixel size
- resolution
- exposure times available

In addition, the Nikon camera had a connecting tube for the microscope attachment that provided an extra magnification of 2.5x.
However, the use of one camera rather than the other one was not a technical choice decided in the experimentation phase, but it was due to the change of instrumentation that was brought into the laboratory during the experimental phase, thus did not depend on the author. It should be noted, however, that these are two cameras with excellent performance and that the change from one camera to the other one did not bring differences neither in the procedure of work nor in the results obtained.
Both the microscope and the camera were controlled remotely through the use of the Nikon's software NIS-Elements: thanks to it, the parameters for the acquisition of images were managed, such as the placement of the stage, the light filter to be used, the light source and time-lapse acquisition.

Chapter 3
Methods

This section will describe the methods followed during the described work. Figures 3.1, 3.2 and 3.3 show the workflow that has been followed. The first two experimental phases, carried out with the classic microfluidic device in PDMS, were followed by the experimentation of the new type of microfluidic device: rock-in chip microfluidics. In this last part of the work, analyses were carried out both deriving from the study of fluid flow within the microfluidic channel, like in first phase of the work, and from the acquisition and analysis of images, as performed in the second phase of the study.

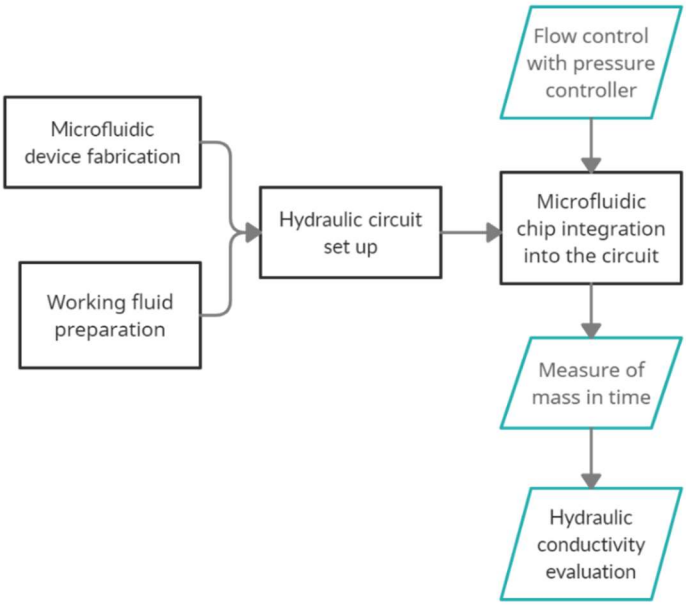

Figure 3.1 - Workflow of classic microfluidic experiment and analysis

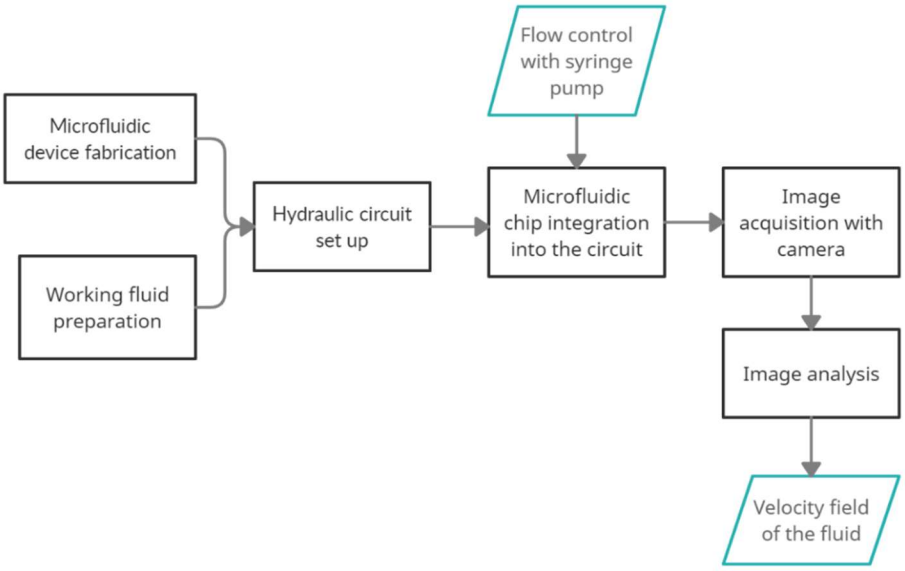

Figure 3.2 - Workflow of PIV data acquisition and analysis

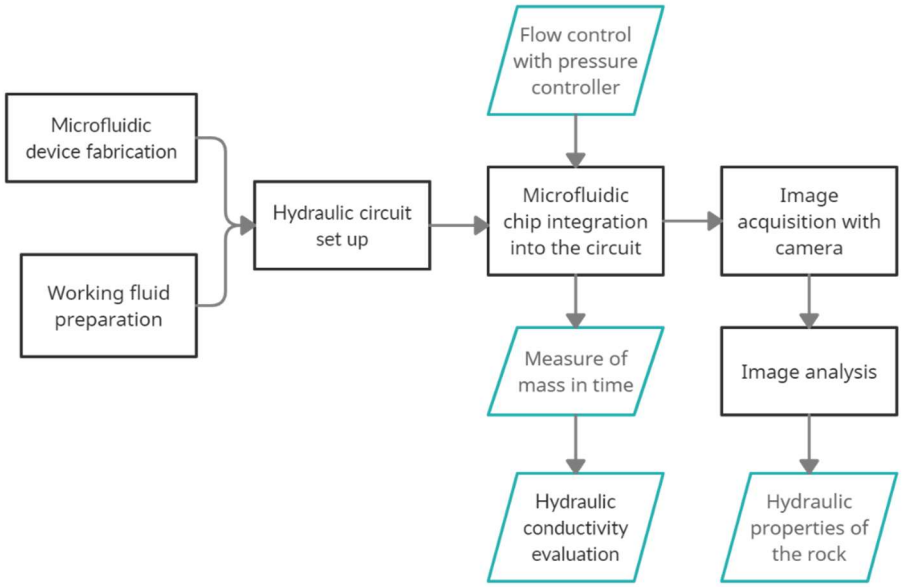

Figure 3.3 - Workflow of rock-in-chip microfluidics experiment and analysis

3.1 Classic Microfluidic Hydraulic Properties Evaluation

In the first working phase, the hydraulic properties of the classic PDMS microfluidic device were measured; in particular, the aim was to determine the hydraulic conductivity of a microfluidic channel which could be assimilated to a porous medium. Hydraulic conductivity expresses the ease with which a fluid is transported through a porous matrix in

presence of a hydraulic gradient. It is, therefore, a coefficient that depends on both matrix and fluid properties. The involved fluid properties are density (ρ) and viscosity (μ), while the involved solid matrix properties are grain-size distribution (or pore-size distribution), shape of grains (or pores), tortuosity, specific surface and porosity.

$$K = k\frac{\rho g}{\mu} \tag{3.1}$$

where k is the permeability. [6]

3.1.1 Experimental Setup

In order to assess the hydraulic conductivity of the microfluidic channel, the materials used among those described in Section 2 were the following:

- PDMS microfluidic chip with circular grains
- Solution for PDMS microfluidic chip
- Pressure controller
- Scale

The preliminary steps of this experiment were the fabrication of the microfluidic device in PDMS and the preparation of the working fluid described in Section 2. Second step was the assembly of the hydraulic circuit (Figure 3.4) with which the experiment was performed. The pressure controller was connected to the inlet and outlet reservoirs, so as to impose the desired pressure difference during the experimental phase. The purpose of the experiment required the use of the pressure controller: in fact, it was intended to measure the hydraulic properties of the microfluidic device, it was necessary to be able to couple pressure differences to the corresponding flow rate generated.

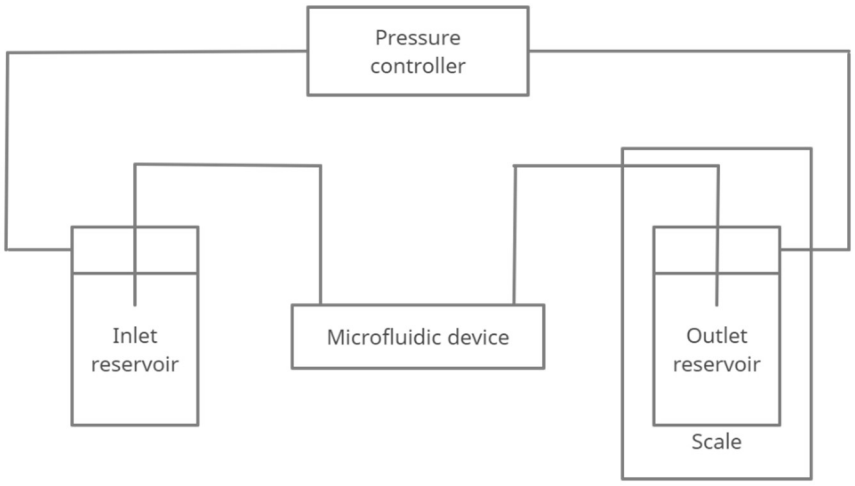

Figure 3.4 - Scheme of the hydraulic circuit for classic microfluidics experiment

Both the inlet and outlet reservoirs contained 20 ml of working fluid, which in this case was Milli-Q water. However, the requirement to be satisfied was only one: the volume of fluid used should have been enough such as not to finish during the experiment; indeed, it was not a fundamental parameter for the success of the experiment. The outlet reservoir was placed on the scale so that its mass can be monitored throughout the duration of the experiment.
The circuit was completed by connecting the microfluidic device to the two reservoirs using PVC laboratory tubings with an inner diameter of 0.5 mm. The lengths of the tubings were:

- 107.5 cm the inlet tubing
- 91 cm the outlet tubing

PDMS microfluidic device with heterogeneous circular grain geometry was used. Before starting the experiment, it was needed to degas the microfluidic device for about 30 minutes in order to eliminate the air inside; the vacuum desiccator already mentioned in Section 2.1.1 was used for this purpose. After the microfluidic channel had been degassed, it was necessary to saturate it with the working fluid within 10 minutes from the end of the degassing: this operation was fundamental for the good realization of the experiment. In fact, if the saturation had been delayed, some air bubbles would have entered the microfluidic channel, risking to compromise the results of the experiment. As a matter of fact, the air bubbles would have modified the fluid flow inside the channel, leading to instability. If they had entered, they would have taken a long time (even a few hours) before they were absorbed by the PDMS itself, delaying the beginning of the experiment – which required a free-bubble channel -. However, it could happen that some air bubbles had entered into the channel without the operator noticing: in this case, the beginning of the experiment would have meant the failure of the experiment itself.

3.1.2 Data Acquisition

Once the hydraulic circuit had been completed, the experiment was carried out. The pressure controller, using the ESI interface, was set to provide an initial pressure difference between the inlet and outlet reservoirs of 100 mbar over a period of 120 s, time required to be sure that the system was stabilized. During the 120 s of pressure difference imposition, the acquisition of mass data by the scale was activated. After finishing the first step, the pressure difference was increased by 10 mbar - bringing it to 110 mbar - for a further time of 120 s, acquiring again the data provided by the scale on which the outlet reservoir was located. This pattern of work, which involved increasing the pressure difference by 10 mbar and acquiring the mass measurements of the outlet reservoir for 120 s, was repeated until the maximum pressure difference that could be imposed with the pressure controller in use, that was 200 mbar, as Figure 3.5 shows. From the figure it can be noticed that the maximum applied pressure difference was about 196 mbar: this was due to the inaccuracy of the pressure controller and its inability to actually approach the maximum of 200 mbar. However, this discrepancy did not compromise the analysis of the results as the ESI interface of the pressure controller itself allowed to acquire the actual pressure values that were

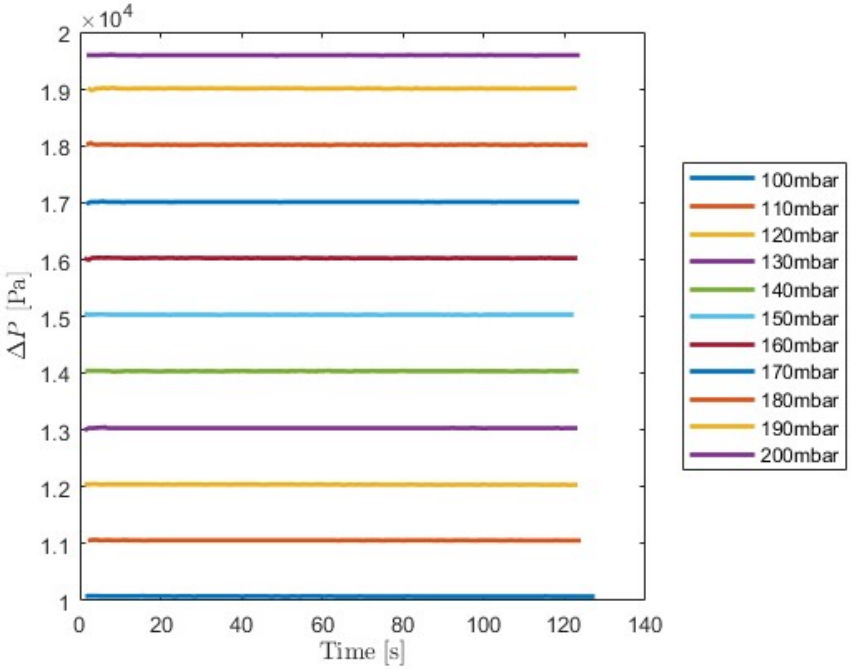

Figure 3.5 - Nominal pressure difference imposed

applied to the inlet and outlet reservoirs, even when they were different from the nominal ones, like in this case.

3.1.3 Data Analysis

The mass and time data from scale were used to calculate the mass flow rate

$$\dot{m} = \frac{dm}{dt} \tag{3.2}$$

where *dm* is the gradient of mass data acquired and *dt* is the gradient of time data acquired. Then the volume flow rate was

$$Q = \frac{\dot{m}}{\rho} \tag{3.3}$$

For each fixed pressure difference step, the volume flow rate was calculated for each recorded data of the experiment in this way. Since each step of pressure difference required the pressure difference to be kept constant, the calculated volume flow rate should also remain constant; for this reason, the average volume flow rate was considered for each step of pressure difference

$$Q_{av} = \frac{\sum Q_i}{n} \tag{3.4}$$

where Q_i refers to all the volume flow rate calculated, and n is the number of acquired data from which instantaneous volume flow rate were calculated.
Considering the section of the microfluidic channel in use

$$A = w \cdot H \tag{3.5}$$

where w is the width of the microfluidic channel and H is its height, the average Darcy velocity could be evaluated as

$$q_{av} = \frac{Q_{av}}{A} \tag{3.6}$$

Regarding the pressure data, it had to be considered that the pressure difference applied was between the inlet and outlet reservoirs, and not between the inlet and outlet of the microfluidic channel being analysed. Pressure losses within the PVC tubings connecting the reservoirs to the microfluidic device were therefore considered.
As the working fluid was incompressible, Newtonian and subject to laminar flow, the flow could be considered as Hagen-Poiseuille flow. In addition, the connecting tubings were circular, thus the analytical solution of the Navier-Stokes equation for the Hagen-Poiseuille flow in a tube of circular section could be used for both the inlet and outlet tubings [19]

$$\Delta p_{tbg} = \frac{8\mu L_{tbg} Q_{av}}{\pi R_{tbg}^4} \tag{3.7}$$

where L_{tbg} is the length of the tubing and R_{tbg} is its radius.
Using '1' as subscript for the pressure imposed at the inlet reservoir and '2' as subscript for the pressure imposed at the outlet reservoir, it was possible to calculate the pressures at the inlet and outlet of the microfluidic channel as

$$p_{in} = p_1 - \Delta p_{tbg,in} \tag{3.8}$$

$$p_{out} = p_2 + \Delta p_{tbg,out} \tag{3.9}$$

thus, the pressure difference between inlet and outlet of the microfluidic channel was

$$\Delta p = p_{in} - p_{out} \tag{3.10}$$

Again, this was the pressure difference for each recorded data, thus an average pressure difference was calculated for each pressure step imposed

$$\Delta p_{av} = \frac{\sum \Delta p_i}{n} \tag{3.11}$$

From the average pressure difference for each step, the pressure gradient along the length of the microfluidic channel was then calculated

$$\nabla p = \frac{\Delta p_{av}}{l} \tag{3.12}$$

where l is the length of the microfluidic channel.
The purpose of this phase of experimental work was to define the hydraulic conductivity of the porous medium under examination. By Darcy's law it is known that the magnitude of the Darcy velocity vector is

$$q = K \cdot i \tag{3.13}$$

where K is the hydraulic conductivity and i is the hydraulic gradient.
In this formulation of the Darcy's law, the hydraulic conductivity results being the proportionality constant that binds the Darcy velocity and the hydraulic gradient. The hydraulic gradient, in turn, can be calculated as

$$i = \frac{dh}{dl} = \frac{\Delta h}{l} \tag{3.14}$$

where h is the hydraulic head.
The hydraulic head is expressed as

$$h = z + \frac{p}{\rho g} \tag{3.15}$$

where z is the elevation. The difference of hydraulic head results thus

$$\Delta h = \Delta z + \frac{\Delta p}{\rho g} \tag{3.16}$$

where the difference in elevation was zero in the case taken in analysis.
Considering Equation 3.12 and Equation 3.16, from Equation 3.14 the hydraulic gradient results in

$$i = \frac{\nabla p}{\rho g} \tag{3.17}$$

Following the above steps, the hydraulic gradient for each step of pressure difference imposed by the pressure controller was obtained.
Starting from the collected data of mass and pressure it was then obtained a pair of data composed of hydraulic gradient and corresponding Darcy velocity for each step of pressure difference that had been imposed: in total the pairs of data obtained were 11.
At this point, a linear interpolation was carried out between the points obtained from the analysis of the initial data: the slope of the interpolation line found turned out to be the value of the hydraulic conductivity, as from Equation 3.13.

It was decided to compare the hydraulic conductivity obtained from the analysis of the experimental data with a theoretical formulation of the hydraulic conductivity, to verify that the calculations carried out had a certain level of credibility also from a theoretical point of view. To this end, the Kozeny-Carman formulation for hydraulic conductivity was used. The Kozeny–Carman equation is a relation to calculate the pressure drop for laminar flow through a packed bed of solids. It was originally developed by Kozeny, using the simplified model of a number of parallel capillary tubes of equal length and diameter (Figure 3.6) to describe the packed bed, starting from Hagen-Poiseuille law. The Kozeny equation is given by [23]

$$\frac{\Delta p}{L} = -\frac{C v \mu}{\sigma_s^2 D^2} \frac{(1-\phi)^2}{\phi^3} \tag{3.18}$$

where Δp is the pressure drop, L is the total height of the bed, v is the superficial velocity, μ is the viscosity of the fluid, ϕ is the porosity of the bed, σ_s is the sphericity of the particles in the packed bed, D is the diameter of the equivalent spherical particle, and C is an empirical constant, which depends on bed tortuosity. The diameter D is considered an estimate of the pore throat size, which is the characteristic dimension for fluid flow in the porous medium.

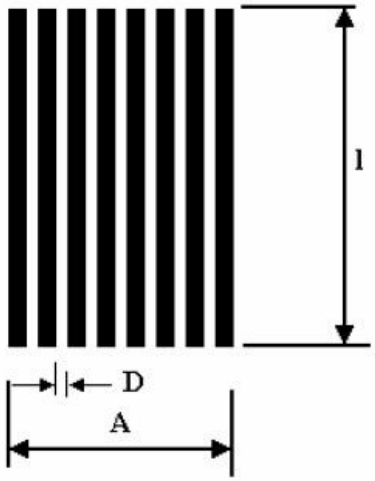

Figure 3.6 - Scheme of Kozeny's model of the packed bed

The sphericity of a particle is defined as

$$\sigma_s = \frac{6/D}{a_v} \tag{3.19}$$

where a_v is the specific surface area of the particle and is representative of the specific surface of the bed if the bed is made of uniform particles. a_v is simply the surface to volume ratio. For a spherical particle with the diameter D, the sphericity results to be 1.

Later, Carman applied Equation 3.18 to experimental results of flow through packed beds, founding that the empirical constant C = 180. Thus, the Kozeny-Carman equation results in

$$\frac{\Delta p}{L} = -\frac{180 v \mu}{D^2} \frac{(1-\phi)^2}{\phi^3} \tag{3.20}$$

Considering the Darcy's law

$$q = \frac{k}{\mu} \nabla p \tag{3.21}$$

where k is the permeability and recalling Equation 3.1, the expression of hydraulic conductivity according to the formulation of Kozeny-Carman is

$$K = \frac{D^2 \phi^3}{180(1-\phi)^2} \frac{\rho g}{\mu} \tag{3.22}$$

From what has been described, it can be understood that the case referred to in the Kozeny-Carman formulation does not accurately reflect what has been experienced with the microfluidic channel in use. However, as already stated, the comparison was not made with the aim to validate the exact result - expecting a coincidence between the two results -, but to understand whether the work carried out could be considered useful as a basis for testing the rock-in-chip microfluidics of new manufacture and obtaining reliable results from a similar analysis.

3.2 Particle Image Velocimetry on Classic Microfluidic Device

During the second phase of the experimental work, a Particle Image Velocimetry (PIV) was performed in order to analyse the flow field and the velocity of the working fluid through the microfluidic channel [7]. As part of the work, this analysis was aimed at developing a methodology able to study the flow field within the rock-in-chip microfluidics. Indeed, coupling the technique that will be illustrated in this paragraph and the analysis of rock dissolution within the rock-in-chip microfluidics in Section 3.3, considerations could have been advanced regarding the relationship between preferential zones for the working fluid flow and preferential zones of dissolution within the microfluidic device itself. In fact, in the zones of higher flow in the microfluidic channel, it was expected to find a greater dissolution of the grains due to the establishment of a greater fluid exchange, with a double consequence:

- the concentration of the dissolved rock around the grains decreased
- the acid concentration of the flow that was flowing was restored

Consequently, the dissolution reaction of the rock by the acid would be much favoured in areas of major fluid replacement.

This was a simplified explanation of what can be quantified through the Damköhler number, which has different formulations in the literature, based on the problem to which it is applied; however, it describes the relationship between the characteristic transport time (t_t) and the characteristic reaction time (t_r) [24]

$$Da = \frac{t_t}{t_r} \tag{3.23}$$

To further expand the analysis, a Damköhler number map could have been constructed to match the flow field of the PIV analysis and the dissolution results.
In addition, by studying the rock dissolution in a rock-in-chip microfluidics, PIV analysis could be repeated several times at time intervals, in order to assess how the flow field changed as the microfluidic channel dissolution progressed. In the event of a change in the flow field over time, it would have been possible to verify how the dissolution pattern would have changed at a later time.

3.2.1 Introduction to PIV

PIV has been recognized as a very useful technique for analysing two-dimensional complex flow fields and two-phase fluid flows. PIV is generally based on fluid visualization and image processing techniques; its main advantages for the study of fluid flow are the following:

- it can instantaneously provide comprehensive and quantitative information about the whole flow field
- it is a contact-free measurement
- it is easy the extraction and processing of physical information through velocity information

The principle behind PIV is the evaluation of instantaneous fluid velocities by deriving the movement distances of the tracer particles - suspended in the fluid - starting from their position in a series of consecutive images acquired by a camera at successive time instants. The tracer particles in the fluid should be:

- distributed as evenly as possible in the fluid
- well reflecting
- accurately follow the motion of the fluid
- not alter the properties of the fluid and its flow

Given as proven the clear visibility of the tracer particles, to meet other conditions the particle tracers should be small and their density should approach the fluid density, as already specified in Section 2.2.2 [25].
PIV differs from Particle Tracking Velocimetry (PTV) as in PIV the fluid velocity results from a statistical analysis performed over the possible displacements of tracer particles

contained in high concentration into the fluid, while in PTV the velocity is determined at random locations, using a single specific tracer particle in the acquired images. As a consequence, PIV is limited to providing only an average velocity, without contributing to provide information on the trajectory of the individual particles within the flow.
PIV analysis allows to study flow fields on planar domains; however, it is performed only on a plane, not allowing the study in a three-dimensional space. This limitation can be overcome with more complicated techniques such as the Tomographic PIV, a technique based on the use of several cameras to record images simultaneously from different angles and analyse them to determine a three-dimensional velocity field, or the Stereoscopic PIV, based on the use of two cameras with different viewing angles in order to determine the third-dimension displacement [25]. However, the work described in this paper was limited to a two-dimensional analysis.
In a basic PIV system, a pulsed light source creates a light sheet which illuminates only the tracer particles contained within the depth of focus of the recording lens, with low levels of background noise emitted from the out-of-focus particles. In this way the thickness of the light sheet determines the out-of-plane spatial resolution of the velocity measurements. However, in a micro-PIV it is not possible to have a light sheet of the micron size and align it to the plane of the objective lens; for this reason, the whole section is illuminated and the definition of the out-of-plane thickness of the measurement plane is entrusted to the focusing of the lens (the section δ is the in focus section with visible particle in Figure 3.7) [26].
A limitation created by this situation is the out-of-plane loss of pairs, which determines a reduction of the signal-to-noise ratio. Some particles, in fact, can enter or exit from the focus plane considered by the PIV, constituting a noise for the analysis of the images: they appear only in one instant of time and not in the next one or vice versa. This is a problem to be considered especially in determining the concentration of tracer particles to be used within the fluid.

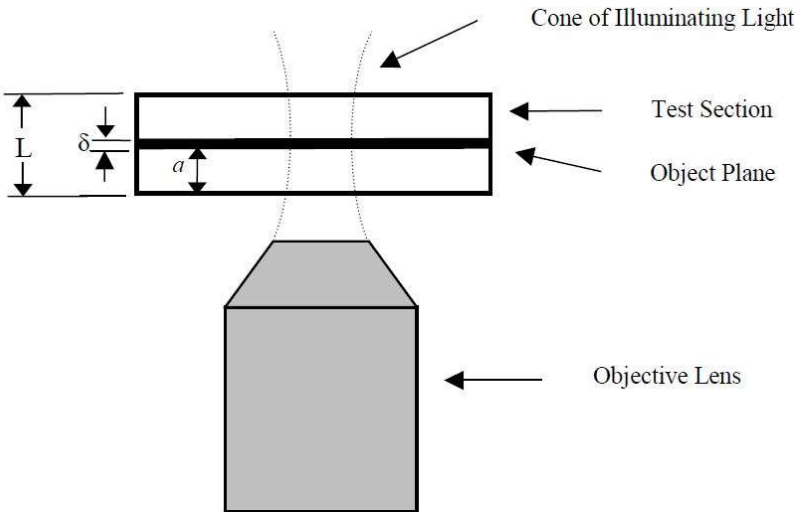

Figure 3.7 - Scheme of the geometry for volume illumination particle image velocimetry (Wereley S., Meinhart C. 2005)

PIV analysis consists of three steps:

- data acquisition
- image processing
- image analysis

In the following sections the experimental set up and the three stages of the PIV will be described.

3.2.2 Experimental Setup

The materials employed during the data acquisition for PIV were:

- PDMS microfluidic chip with complex geometry
- PIV solution
- syringe pump
- microscope
- Nikon DS-Qi2 camera

It was chosen the microfluidic device with complex geometry as it was the most suitable for the development of a MATLAB code appropriate for the processing and the analysis of the acquired images, differently from the device with circular geometry, in which the complexity of the fluid flow would be less.
As flow control device, the syringe pump was chosen because - unlike the case study previously described - in this case it was not necessary to measure the pressure difference at the ends of the microfluidic channel, but rather the imposed flow rate, as a measure of comparison with the velocity field obtained from the analysis carried out.
Regarding the camera, the use of Nikon DS-Qi2 instead of Hamamatsu ORCA flash 4.0 V3, as previously specified, was not the result of a choice due to the characteristics of the camera itself; the reason for its use was that the camera was supplied to the laboratory where the experiment took place.
As also specified in Section 2.1.1, the first step was to degas the microfluidic device for about 30 minutes in the vacuum desiccator in order to eliminate the air inside of the microfluidic channel.

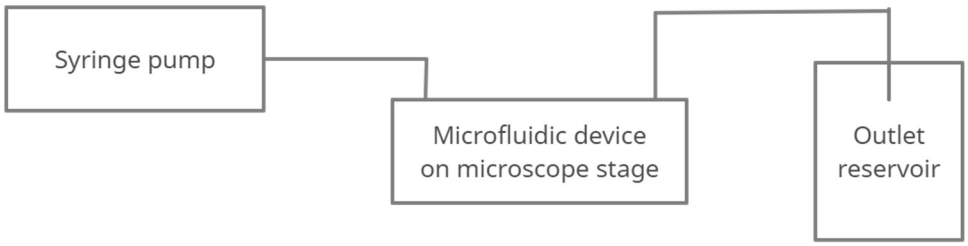

Figure 3.8 - Scheme of the hydraulic circuit for PIV

Figure 3.8 shows how the hydraulic circuit was assembled for this working phase: the microfluidic channel was connected to both the syringe pump and the outlet reservoir through PVC tubings. Since no mass measurements were needed to perform the PIV, in this case the outlet reservoir was not placed on the scale.
The microfluidic device was placed on the microscope stage, so that images of the microfluidic channel could be acquired with the microscope and the camera.
Before starting to acquire the necessary data, and within ten minutes after the end of the process of degassing the microfluidic device, the microfluidic channel was saturated with the working fluid, imposing a flow of 1 µl/min for about 30 minutes with the syringe pump.

3.2.3 Data Acquisition

The acquisition of images to perform the PIV was done by imposing a fluid flow rate of 0.1 µl/min with the syringe pump.
The images were acquired only in a small portion of the microfluidic channel and not in its entirety, as the actual objective of this phase of work was not the characterization of the fluid flow within the complex geometry microfluidic channel in use, but rather the verification that the technique provided results reflecting the conditions of flow imposed by the syringe pump. The investigated area was 5 mm x 1.5 mm, as a result of the acquisition in 21 different locations divided into a 7 x 3 grid area.
The images of particles motion within the fluid flow were acquired with the camera. They could be captured on a single frame and double exposure or on two separate frames at single exposure [25]. The image analysis method would have been different according to the acquisition method. To capture images in separate frames at single exposure was chosen as method.
Despite the fact that only two images at successive instants of time would have been sufficient to perform the PIV analysis, it was chosen to capture 150 images per location; therefore, the displacement of particles in a greater number of time intervals could be analysed. The results obtained for each location were subsequently averaged during the analysis in order to obtain individual values averaged over the time of investigation.
The camera and microscope parameters used during data acquisition were as follows:

- resolution = 1636 x 1088
- exposure time = 50 ms
- magnification = 20x (from microscope) · 2.5x (from camera tube) = 50x
- 8 bit acquisition

In order to obtain images in which only fluorescent tracer particles appeared, the images were captured using the SOLA light source - as illumination source of the microscope - and a yellow light filter.
The NIS-Elements software, that managed the microscope and the camera, allowed to record the time intervals that elapsed between the acquisition of one image and the next one; that was a critical value for performing the analysis and determining the velocities.

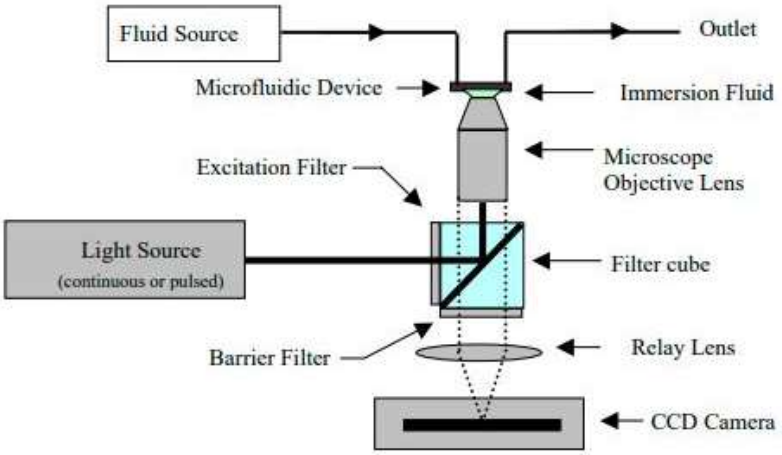

Figure 3.9 - Scheme of the data acquisition system (Wereley S., Meinhart C. 2005)

Figure 3.9 shows how a data acquisition system for micro-PIV is set up.
After the acquisition of the images for PIV had finished, it was decided to take a fluorescence image for each location under investigation. This was done in order to be able to process the images at a later time with the purpose of eliminating possible particle measurements in the spaces occupied by the grains, as it will be explained below. With the aim of doing that, a fluorescent solution of Milli-Q water and fluorescein concentrated at 3 mg/l was injected into the microfluidic channel with a luer-lock syringe, which replaced the syringe pump. The images were also taken in this case using the SOLA light source, in order to detect fluorescence within the microfluidic channel.

3.2.4 Image Processing

In this section and in the next one, it will be described how the previously acquired images have been processed and analysed referring to a single location. However, the same procedure was applied to all (21) locations where the images were captured.
Image processing involved the creation of new images from those that were being processed, in order to improve them and make them more suitable for the following analysis.
The purpose of the image processing that was carried out was to obtain images that had a lower noise, so as to facilitate the identification of tracer particles.
In addition, it was intended to process the images in such a way as not to wrongly identify particles in areas of the microfluidic channel occupied by the grains: for this purpose, the fluorescent images collected at the end of the data acquisition were employed.
Therefore, the image processing methods used were:

- averaging
- thresholding

Averaging was applied on all the 150 images collected in a single location, with the aim of generating a new background image. This image was intended to be removed from the acquired images to eliminate noise and obtain modified images - more easily analyzable - in

which the particles were more recognizable. The net effect was that the contribution of moving particles was small on average, while the stationary noise that was present in all images constituted the background image [27].
Considering an image $I_i(x,y)$ and the noise of the image $N(x,y)$, the noisy image $G_i(x,y)$ results in

$$G_i(x,y) = I_i(x,y) + N(x,y) \tag{3.24}$$

and the average of the noisy images

$$\bar{G}(x,y) = \frac{1}{n}\sum_{i=1}^{n} G_i(x,y) \tag{3.25}$$

Bearing in mind that, as has been said, the average of a noisy image is almost entirely made up of the noise of it, it is inferred that

$$E\{\bar{G}(x,y)\} = N(x,y) \tag{3.26}$$

where $E\{\bar{G}(x,y)\}$ is the expected value of the average of the images.
This means that by subtracting the average of the images from all the images acquired, for the Equations 3.24 and 3.26, it was expected to get the image "clean" from the noise; in fact

$$G_i(x,y) - E\{\bar{G}(x,y)\} = I_i(x,y) \tag{3.27}$$

The only drawback of this methodology lies in the possibility that some particles move slowly enough to appear in all images, resulting in influencing the determination of the average and being eliminated with it in the processing of the image. However, this potential problem is largely compensated by the greater ease in analysing images processed in this way.
Thresholding, on the other hand, was applied to fluorescence images captured in the last phase of data acquisition, not to images for which PIV was carried out. It was used, in fact, to derive the mask $M(x,y)$ of the geometry of the microfluidic channel from fluorescence images. Indeed, thresholding is the process of discriminating pixels depending on their gray scale intensity: the pixels with a intensity above the threshold are replaced with the value 1 (white) and all the other pixels are replaced with the value 0 (black) [27]

$$M(x,y) = \begin{cases} 0 & if\ I(x,y) < \tau \\ 1 & if\ I(x,y) \geq \tau \end{cases} \tag{3.28}$$

where τ is the threshold.
In the image processing that was carried out, the thresholding was performed with the *imbinarize* MATLAB function, which selects the threshold by the Otsu method [28]. Otsu method minimizes intra-class variance, defined as the weighted sum of the variances of the two classes as follows [29]

$$\sigma_w^2(\tau) = \omega_0(\tau)\sigma_0^2(\tau) + \omega_1(\tau)\sigma_1^2(\tau) \tag{3.29}$$

where the weights ω_0 and ω_1 are the probabilities of the two classes separated by the threshold τ, while σ_o^2 and σ_1^2 are the variances of the two classes.
By pairing averaging and thresholding, all location images were modified to new images $II_i(x,y)$ according to the equation

$$II_i(x,y) = [G_i(x,y) - E\{\bar{G}(x,y)\}] \cdot M(x,y) \tag{3.30}$$

In practice, the background noise, obtained with averaging, was subtracted from the acquired images obtaining "clean" images; then the "clean" images were multiplied by the mask obtained from thresholding: in this way, everything that would have been detected in the spaces actually occupied by the grains of the microfluidic channel was made 0, in other words not considered, eliminating any errors in those areas of microfluidic channel.

3.2.5 Image Analysis

After the image processing, the images were analysed in such a way to obtain the fluid flow velocity in the portion of the microfluidic channel examined.
Since the images were acquired with single exposure, the appropriate method for their analysis was cross-correlation; on the contrary, if the images were acquired with double exposure, auto-correlation should have been applied [25].
Considering the intensity of the areas of investigation (supposed to be square of size D for simplicity) of two images at two successive instants of time as $f_{i,j}$ and $g_{i,j}$, their normalized cross-correlation in the discretized version results

$$\Phi(\Delta x, \Delta y) = \frac{\sum_{i,j}^{D}\left(f_{i,j} - \mu_f\right)\left(g_{i+\Delta x, j+\Delta y} - \mu_g\right)}{\sqrt{\sum_{i,j}^{D}\left(f_{i,j} - \mu_f\right)^2 \sum_{i,j}^{D}\left(g_{i+\Delta x, j+\Delta y} - \mu_g\right)^2}} \tag{3.31}$$

where μ_f and μ_g are the mean intensities of the interrogation areas.
The main advantage of this method is that Fast Fourier Transform (FFT) can be used thanks to cross-correlation theorem, according to which [30]

$$\Phi(\Delta x, \Delta y) = F^{-1}\{F\{f\}^* \cdot F\{g\}\} \tag{3.32}$$

where F is the Fourier transform and the star denotes the complex conjugate.
In this way, image analysis is faster and less expensive, from a computational cost point of view.
Figure 3.10 shows how image analysis takes place using cross-correlation and correlation theorem.
Images captured at successive times are divided into interrogation windows (Figure 3.10a), which are subjected to a FFT cross-correlation procedure (Figure 3.10b). In the resulting

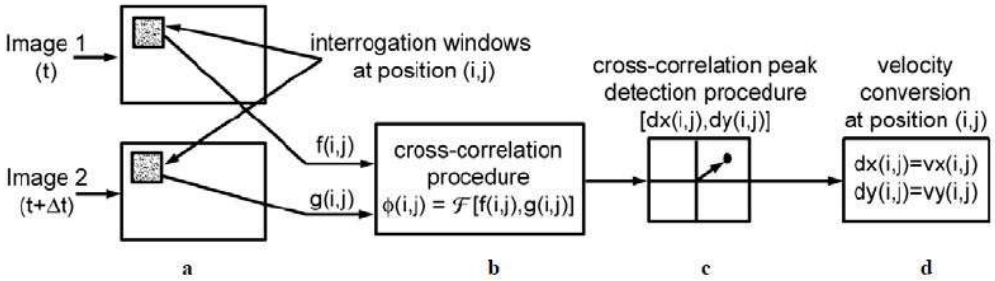

Figure 3.10 - Cross-correlation image analysis procedure using an FFT algorithm (Dabiri D. 2007)

image, the cross-correlation peak is searched for: the maximum of the cross-correlation map provides the location of the most likely displacement of the particles within the interrogation spot (Figure 3.10c). Through calibration parameters, the displacement obtained (*dx* and *dy*) is converted into velocity (Figure 3.10d), having also the interval of time between the acquisition of the two images

$$v_x(i,j) = \frac{\Delta x(i,j)}{\Delta t} \tag{3.33}$$

$$v_y(i,j) = \frac{\Delta y(i,j)}{\Delta t} \tag{3.34}$$

where Δx and Δy are the displacements corresponding to the pixel displacements *dx* and *dy* [31].

In order to improve the analysis and increase the signal-to-noise ratio, during the analysis it was decided to use a 3 passes cross-correlation approach [25]. The first interrogation window was selected as a square of 128 pixels on the side. The analysis developed in this first step was the basis for a second analysis in which the interrogation window was 64 pixels. The third - and last – analysis, based on the previous one, had interrogation windows of 32 pixels, making the total analysis more accurate.

Since, as already stated, 150 images were captured for each location, as a result the displacements and corresponding velocities were calculated for 149 successive time intervals for each location. For this reason, at the end of the analysis, for each interrogation window of each different location was calculated the average of all the velocities that had been obtained

$$v_{x,av}(i,j) = \frac{\sum v_x\,(i,j)}{n} \tag{3.35}$$

$$v_{y,av}(i,j) = \frac{\sum v_y(x,y)}{n} \tag{3.36}$$

where *n* in this situation was 149.

From the axial velocity components obtained, the velocity vector magnitude was derived in each interrogation window of each location

$$|u|(i,j) = \sqrt{v_{x,av}^2 + v_{y,av}^2} \tag{3.37}$$

In order to compare the result of the PIV analysis with the flow rate that had been imposed with the syringe pump, the average velocity was calculated over the entire portion of microfluidic channel investigated by the PIV analysis

$$u_{av} = \frac{\sum_{loc}\left[\frac{\sum_i \sum_j |u|\,(i,j)}{i \cdot j}\right]}{loc} \tag{3.38}$$

where *loc* defines the different locations in which images have been captured.
All the operations described for image processing and image analysis were carried out using a MATLAB code.

3.3 Rock-in-chip Microfluidics Experimentation

The last phase of the experimentation carried out involved the use of the novel rock-in-chip microfluidics device. As this technology was new and not yet tested, the experimental phase had three main objectives:

- testing of the device under experimental conditions
- assessment of the hydraulic conductivity of the microfluidic channel, in a similar way to what was done with the PDMS microfluidic channel
- use of image analysis to assess properties such as average grain radius, average pore throat size, porosity and theoretical value of hydraulic conductivity according to the Kozeny-Carman formulation during the rock-in-chip microfluidics dissolution. The evaluations of these characteristics were made at regular intervals of time in order to be able to evaluate, moreover, how the dissolution of the rock changed the properties of the microfluidic channel

It should be noted that initially, as stated in Section 3.2, a PIV analysis was planned, but the collection of data for the analysis was not possible. This was due to the non-visibility under the microscope of the fluorescent tracer particles used to obtain the data to be analysed; this was attributable to a not optimal manufacturing of the microfluidic channel, owing to the fact that it was the first time that the technique was used in order to create the novel rock-in-chip microfluidics. In fact, the channel of the rock-in-chip microfluidics had not been totally etched: in some areas there was a residual layer of rock with a thickness in the order of some μm. The residual rock layer was not significant for the other activities requiring the use of image analysis, because a fluorescent working fluid was used, and the small layer of rock was not able to block its fluorescence. As for fluorescent particles, on the contrary, they could not be detected because their fluorescence could not overcome the residual rock because of their small size.

Nevertheless, the potential for coupling PIV analysis with dissolution analysis remains unchanged, as will be stated in the section on future directions.
As regards the experimental phase with rock dissolution, an acetic acid solution was used. The kinetic of dissolution of calcium carbonate is a function of the concentration of the carbonate species in the solution and, therefore, a function of the partial pressure of carbon dioxide (CO_2) and pH. Calcite dissolution has been characterized in terms of three pH regimes: a low pH regime, a transitional regime, and a high pH regime [32]:

$$CaCO_3 + H^+ \leftrightarrow Ca^{2+} + HCO_3^- \qquad \text{pH} < 3.5 \qquad (3.39)$$

$$CaCO_3 + H_2CO_3^0 \leftrightarrow Ca^{2+} + 2HCO_3^- \qquad 3.5 < \text{pH} < 5.5 \qquad (3.40)$$

$$CaCO_3 + H_2O \leftrightarrow Ca^{2+} + HCO_3^- + OH^- \qquad \text{pH} > 6.5 \qquad (3.41)$$

At low pH (Equation 3.39) the dissolution is limited by the transport of hydrogen ions to the calcite surface and is unrelated with the partial pressure of CO2.
At transition pH (Equation 3.40) the kinetics of the surface reaction begins to influence the dissolution, while mass transfer provides significant limitations.
In the high pH regime (Equation 3.41), with pH close to saturation, hydrolysis reaction starts to become important, and the dissolution rate of calcium carbonate decreases drastically, depending on CO_2 pressure.
Since the working fluid used for the experiment had a pH of 2.5 (Section 2.2.3), it was expected that the reaction concerned would have been the one with low pH of Equation 3.39.

3.3.1 Experimental Setup

Experimentation with rock-in-chip microfluidics was carried out with the following materials, already described in Section 2:

- rock-in-chip microfluidics device
- rock dissolving solution
- solution of Milli-Q water and fluorescein concentrated at 3 mg/l
- pressure controller
- scale
- microscope
- Hamamatsu ORCA flash 4.0 V3 camera

As flow control system was chosen the pressure controller because, as happened also for the experimentation on the PDMS microfluidic device (Section 3.1.1), it was necessary to have a measure of the pressure levels at the ends of the microfluidic channel, in order to evaluate the hydraulic conductivity of the channel.
In the same way as the PIV analysis (Section 3.2.2), it should also be pointed out that the use of the Hamamatsu ORCA flash 4.0 V3 camera was not due to a technical choice, but to a change of equipment in the laboratory where the experiments were taking place.

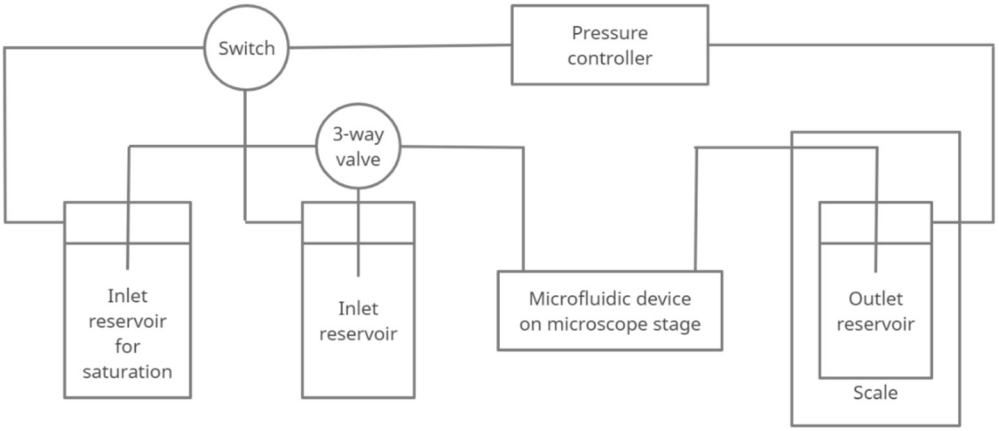

Figure 3.11 - Scheme of the hydraulic circuit for rock-in-chip microfluidics experiment

Figure 3.11 shows how the hydraulic circuit was constructed for testing the rock-in-chip microfluidics: as can be noted, it was more complicated than the hydraulic circuits previously used. The pressure controller was connected to the inlet and outlet reservoirs; however, unlike what happened in the first experiment (Section 3.1.1), the inlet reservoirs were two. For this reason, a switch was introduced so that the same pressure could be applied to both inlet reservoirs. Two inlet reservoirs were used because one contained the mixture of Milli-Q water and fluorescein used at first to saturate the microfluidic channel and to verify under the microscope that the channel was well sealed and the fluid did not escape from it, while the other one contained the rock dissolving solution that was used in the second phase of the experimentation. Due to the presence of two different inlet reservoirs for the microfluidic channel, a three-way valve was used to select which of the two reservoirs should actually be in communication with the rock-in-chip microfluidics. Even in this case the outlet reservoir was placed on the scale, so that mass measurements could be made to obtain the fluid flow rate that passed through the microfluidic channel.
The rock-in-chip microfluidics was integrated into the hydraulic circuit after being assembled. It was placed on the microscope stage so that images could be captured during the experiment and be analysed at a later time. PVC laboratory tubings with an internal diameter of 0.5 mm were used to connect the microfluidic channel to the inlet and outlet reservoirs. For the connection between the two inlet reservoirs and the rock-in-chip microfluidics it was taken care to make sure that the total length of the tubing (considering both the part before the valve and the common one between valve and inlet of the microfluidic channel) was the same for both reservoirs. The total lengths of the connecting tubings were:

- 140 cm for the inlet tubing
- 100 cm for the outlet tubing

As already stated in Section 2.1.2, the microfluidic channel and PDMS layer were degassed before assembly. However, the time taken to assemble the device and integrate the rock-in-chip microfluidics into the hydraulic circuit was quite long. For this reason, after saturation of the microfluidic channel, it had to be verified the absence of air bubbles in the channel

before the experiment could begin. After introducing the rock-in-chip microfluidics in the hydraulic circuit, in fact, the microfluidic channel was saturated by imposing with the pressure controller a pressure difference of 100 mbar between the inlet reservoir (the one with Milli-Q water and fluorescein) and outlet reservoir. While saturation was taking place, the microfluidic channel was observed in real time by the microscope with fluorescent light to verify the absence of air bubbles and the proper sealing of the device, without fluid leaks from the microfluidic channel. As the first leakage test of the rock-in-chip microfluidics was successful, it was possible to omve on to data acquisition.

3.3.2 Data Acquisition

The first phase of the experiment involved the assessment of the hydraulic conductivity of the rock-in-chip microfluidics channel. To collect the data, the solution employed to saturate the channel was used also as working fluid in this phase, since the dissolution of calcite did not need to begin at this stage; therefore, the inlet reservoir was not switched yet. The data acquisition, however, took place with a slightly different method than with the PDMS microfluidic channel (Section 3.1.2).
In fact, in this case the pressure of the outlet reservoir was fixed with the pressure controller at 20 mbar, while the pressure of the inlet reservoir was linearly varied from 20 mbar to 200 mbar in a time interval of 10 minutes, resulting in a pressure difference between inlet and outlet reservoir shown in Figure 3.12. The mass of the outlet reservoir was measured with the scale and the measurements were saved, therefore the fluid flow rate - caused by the pressure difference - could be derived from the mass data.

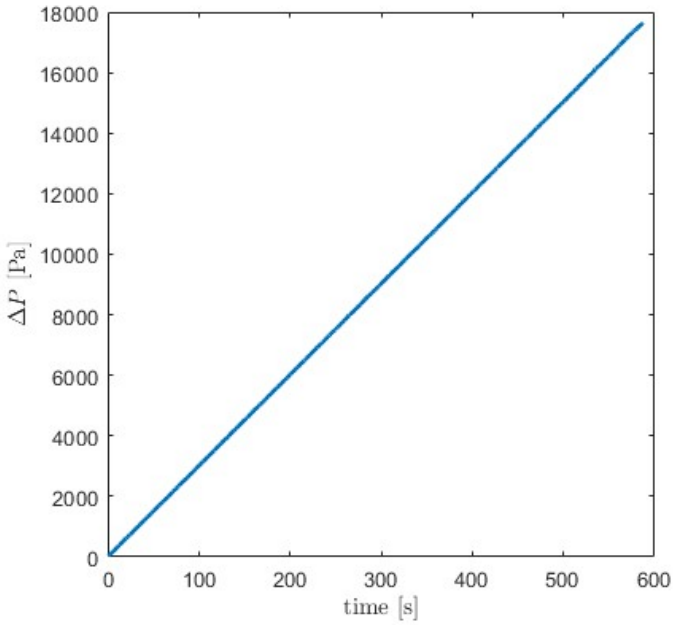

Figure 3.12 - Nominal pressure difference imposed

At this point, the collection of data necessary for the evaluation of the hydraulic conductivity of the rock-in-chip microfluidics was finished, consequentially it was possible to begin the new phase of the experiment, consisting of the measurement of the other properties of the microfluidic channel - previously listed in Section 3.3 - in the presence of rock dissolution. For this purpose, the inlet reservoir connected to the inlet of the microfluidic channel was switched from the one containing the Milli-Q water and fluorescein solution to the one containing the rock dissolving solution.
The second phase of the experiment lasted 24 hours and required the acquisition of microscope images to be analysed at a later time.
Inside the rock-in-chip microfluidics was established a flow by imposing a pressure difference between the inlet reservoir and the outlet reservoir with the pressure controller: for the first hour it was set to 10 mbar, while for the remaining 23 hours of the experiment a nominal pressure difference of 180 mbar was set (Figure 3.13).
Initially the pressure difference was set to 10 mbar for safety reasons: being the first time the device was used for a long-term trial it was decided to start with a low pressure difference. Moreover, it was the first time the device was used with a solution that had to dissolve it; not being able to predict how the system would have reacted, a cautious start was chosen. After the first hour it was certified that the device had not suffered any complications and it was verified that the generated flow rate was very low. For this reason, it was decided to raise the pressure difference between the inlet reservoir and the outlet reservoir to 180 mbar. Given the large increase in pressure difference, during the first few hours after the increase, the system was visually checked to ensure that no problems would have arisen in the microfluidic device; in the event that problems were revealed, the trial would have been stopped. Actually, no criticality was found, thus the experiment was conducted until the end - for 24 hours -. In the second phase of the experiment also, the mass measurement data of the outlet reservoir were collected by the scale.

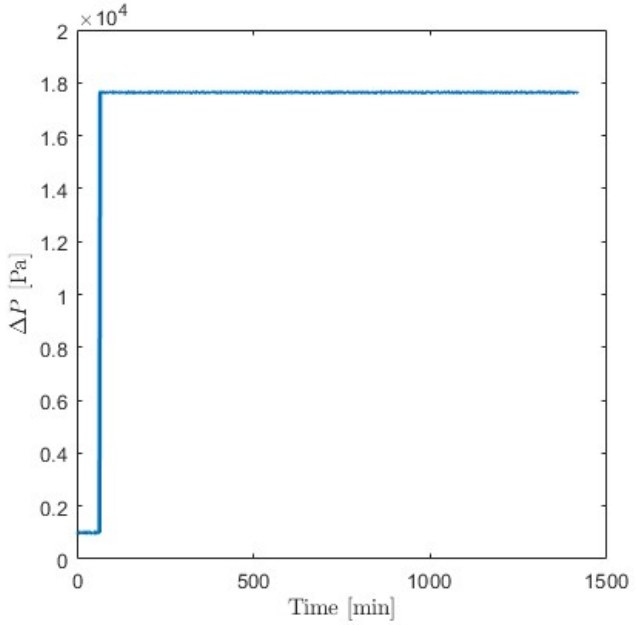

Figure 3.13 - Nominal pressure difference imposed during dissolution experiment

To perform image analysis to assess microfluidic channel properties, images were captured every 20 minutes during the 24-hour period. They were acquired in two modalities:

- fluorescence
- bright-field

Both modalities had in common the following microscope and camera settings:

- resolution = 2048 x 2048
- magnification = 10x
- 8 bit acquisition

However, the exposure time was different in the two cases. Regarding fluorescence microscopy, for which the SOLA light source and a yellow light filter were used to capture fluorescein's fluorescence, the exposure time needed to better capture the images was 30 ms. Regarding bright-field microscopy, instead, which exploits the attenuation of white light due to the presence of an object, the exposure time used was 2 ms.
Since a single image could not contain the entire rock-in-chip microfluidics, large images were taken: a series of images were taken in adjacent locations to cover the entire surface of the microfluidic channel. After that, the NIS-Elements microscope and camera management software reconstructed the complete image by stitching the images taken.
At this stage, if it were possible, data would have been collected for PIV analysis. The procedure intended to be followed was quite similar to the one followed for the PIV analysis in the PDMS microfluidic channel (Section 3.2.3). Again 150 images would have been captured at successive instants of time for each location chosen in the microfluidic channel. Unlike what previously done in Section 3.2.3, however, for the rock-in-chip microfluidics a number of locations sufficient to cover the entire area of the microfluidic channel would have been selected, so that the flow field in its entirety could have been assessed. Another difference compared to the previous one was in the light filter to be used: in the working fluid, in fact, the inserted particles were fluorescent in the red light, thus a red-light filter would have been used. In this way, both yellow-light and red-light fluorescent images could have been captured at the same time by only changing the light filter. Although the PIV analysis phase could not be carried out, the methodology described may be used in a similar experiment in the future.
At the end of the data acquisition, data analysis began.

3.3.3 Data Analysis for Hydraulic Conductivity

Data analysis for the assessment of the hydraulic conductivity of the rock-in-chip microfluidics was similar to the one performed for the hydraulic conductivity of the PDMS microfluidic channel, since the methodology followed in running the experiment was analogous to the one previously described in Section 3.1.3. The only difference was that in this case it was not necessary to average the data but, due to the way the data were acquired, it was possible to make instantaneous evaluations.

The mass flow rate was calculated from mass and time data acquired by the scale

$$\dot{m} = \frac{dm}{dt} \tag{3.2}$$

from which the volume flow rate resulted

$$Q = \frac{\dot{m}}{\rho} \tag{3.3}$$

Considering the rock-in-chip microfluidics channel section

$$A = w \cdot H \tag{3.5}$$

the Darcy velocity was

$$q = \frac{Q}{A} \tag{3.6}$$

The pressure losses in the tubings connecting the rock-in-chip microfluidics to the inlet and the outlet reservoirs were calculated with the analytical solution of the Navier-Stokes equation for the Hagen-Poiseuille flow in a tube of circular section, since the working fluid was incompressible, Newtonian and subject to laminar flow, and the tubings were circular

$$\Delta p_{tbg} = \frac{8\mu L_{tbg} Q_{av}}{\pi R_{tbg}^4} \tag{3.7}$$

Thus, the pressures at inlet and outlet of the rock-in-chip microfluidics could be evaluated as

$$p_{in} = p_1 - \Delta p_{tbg,in} \tag{3.8}$$

$$p_{out} = p_2 + \Delta p_{tbg,out} \tag{3.9}$$

and the pressure difference between inlet and outlet

$$\Delta p = p_{in} - p_{out} \tag{3.10}$$

From pressure difference, the pressure gradient was calculated

$$\nabla p = \frac{\Delta p}{l} \tag{3.12}$$

Considering Equation 3.12 and Equation 3.16, from Equation 3.14 the hydraulic gradient results in

$$i = \frac{\nabla p}{\rho g} \tag{3.17}$$

Since the Darcy's law states that the Darcy velocity magnitude is

$$q = K \cdot i \tag{3.13}$$

and the data of Darcy velocity and hydraulic gradient were already calculated, in order to find the hydraulic conductivity, a linear interpolation of the data was carried out: the slope of the interpolation line turned out to be the hydraulic conductivity of the rock-in-chip microfluidics.
Even the hydraulic conductivity calculated for the rock-in-chip microfluidics was compared with the theoretical hydraulic conductivity evaluated with the Kozeny-Carman formula, to verify the affinity between the rock-in-chip microfluidics and the theoretical model considered by Kozeny-Carman, referred to in Section 3.1.3

$$K = \frac{D^2 \phi^3}{180(1-\phi)^2} \frac{\rho g}{\mu} \tag{3.22}$$

However, in this case, the average grain diameter could not be considered as a good estimate of the characteristic dimension for the flow in the porous medium. In fact, it had to be considered that the height of the rock-in-chip microfluidics was actually lower than the nominal one of manufacturing (40 μm). This had two causes:

- the presence of the residual rock layer at the base of the rock-in-chip microfluidics
- the pressure of the PDMS from above, caused by the force applied by the clamps to seal the microfluidic channel

as a result, for an approximate estimate, the height of the rock-in-chip microfluidics could be considered lower than the nominal one: 20 μm. Since the height was much lower than the average grain diameter, it was to be considered as the characteristic dimension for the flow in the porous medium within the Kozeny-Carman formula.

3.3.4 Dissolution Data Analysis

To evaluate the variation of the average grain radius, of the average pore throat size, of the porosity and of the hydraulic conductivity according to the Kozeny-Carman formula, images have been acquired. In order to obtain the desired results, two steps were needed:

- image processing
- image analysis

Both steps were applied to the fluorescent images only, as the bright-field images were acquired only to make qualitative - and not quantitative - considerations.

3.3.5 Image Processing

Two methods were used in the processing of captured images in order to obtain better images for image analysis [27]:

- Gaussian smoothing filtering
- thresholding

The Gaussian smoothing filter is a 2-D convolution operator used to blur images and remove detail and noise. In fact, it attenuates the variations of light intensity in the neighborhood of a pixel, smoothing the overall shape of objects and attenuating details. The filter uses a Gaussian function with mean equal to zero in order to build a kernel for the calculation of the new intensity of each pixel. In two dimensions, an isotropic Gaussian function with mean equal to zero has the form

$$GF(x,y) = \frac{1}{2\pi\sigma^2} e^{-\frac{x^2+y^2}{2\sigma^2}} \tag{3.42}$$

Values from the Gaussian distribution are used to build the kernel to be applied to the image; the kernel has the following shape

Table 3.1 - Example of a Gaussian smoothing filter kernel

b	a	b
a	x	a
b	a	b

with a decreasing value as distance from the central pixel - to which processing is applied - increases (x > a > b). Since all the coefficients are positive, as a result each pixel intensity is transformed in a weighted average of its neighbors. The method by which the transformation kernel is built implies that the closer a pixel is to the one being processed, the greater is its weight in defining the intensity of the pixel in the new processed image.
Gaussian smoothing filtering was applied to all fluorescent images acquired within 24 hours of the experiment. The only parameter to be selected was the standard deviation and it was chosen to be σ = 3: this value was selected because it was the best one to create a new image for the following analysis. The actual application of the filter to the images was carried out using the MATLAB *imgaussfilt* function [33].
Before applying thresholding, the images were rotated and cropped in such a way that only the microfluidic channel remained in the image. After the cropping, the images resulted in a 3000 x 30000 pixels size. This step was crucial to properly analyse the images, eliminating interference elements external to the microfluidic channel that could have influenced the result.

Thresholding was applied with the aim of obtaining binarized images; during the image analysis, in fact, it was important that the images were binarized in order to be able to recognize the geometric structures present, as it will be explained later. Even though during image processing for PIV analysis (Section 3.2.4) the Otsu method was used for establishing the threshold value, in the current experiment an adaptive threshold was employed. This choice was guided by the fact the images processed had areas in which the intensity of light varied significantly. The threshold value to be used for each pixel was calculated as the average of the pixel values in a 501 pixels-side square neighborhood of the pixel whose threshold was being calculated, using the MATLAB function *adaptthresh* [34]. The threshold obtained by the adaptive method was scaled for a better image processing: the final threshold was considered as 60% of the calculated adaptive threshold. As a result of image processing, a microfluidic channel mask was obtained: in it, the pixels corresponding to the grains of the rock-in-chip microfluidics had 0 as value, while the pixels corresponding to the pores had 1 as value.

3.3.6 Image Analysis

As a result of the mask implementation method (pixels of value 1 for pores and pixels of value 0 for grains), the calculation of the porosity of the microfluidic channel was straightforward. Indeed, considering that porosity is defined as the ratio of the volume of voids to total volume [6]

$$\phi = \frac{V_v}{V} \tag{3.43}$$

for the acquired images resulted

$$\phi = \frac{\sum px}{n_p} \tag{3.44}$$

where px is the intensity of the pixels and n_p is the number of the pixels of the image.
However, the calculation of average grain radius, average pore throat size and theoretical hydraulic conductivity required more elaborated image analysis.
The basic idea, for obtaining the desired information from the masks that were created with image processing, was to recognize in the images the grains of the porous medium. For this purpose, it had to be considered that the grains in the images were, geometrically, circles within the microfluidic channel. The MATLAB function *regionprops* was used at this stage of the analysis [35]. The *regionprops* function recognizes the 8-connected components (objects) present in a binary image. The 8-connected components are made up of all pixels with the same intensity whose sides or corners touch, therefore they can be connected horizontally, vertically or diagonally. Hence, the grains in the microfluidic channel were recognized by *regionprops* function as distinct objects to be analysed. The function calculated the following properties for each identified object within the image:

- centroids
- major axis length
- minor axis length

Regionprops stored the horizontal and vertical coordinates of the centers of mass of each detected object, thus it provided the coordinates of the centers of mass of the grains of the porous medium.
Regionprops stored the length of the major axis of the ellipse with the same normalized second central moments as the region's one, returned as a scalar, named as "major axis length" (MAL).
Regionprops stored the length of the minor axis of the ellipse with the same normalized second central moments as the region's one, returned as a scalar, named as "minor axis length" (mal).
Since the grains of the microfluidic channel were circular, MAL and mal should have been equal and coincident with the diameters of the grains; however, as they were slightly different due to either imperfections in microfluidic channel manufacturing or inaccuracies in image processing, the diameters of the grains were considered as the average between MAL and mal. The grain radii were derived from the calculated diameters. Subsequently, the radii were averaged, in order to have the evaluation of the average radius of the grains of rock-in-chip microfluidics

$$R_i = \frac{(MAL_i + mal_i)/2}{2} \tag{3.45}$$

$$R_{av} = \frac{\sum R_i}{n} \tag{3.46}$$

The last phase of data analysis was the one needed to derive the pore throat sizes from the data obtained from the *regionprops* function. For this purpose, the Delaunay triangulation was applied to the grain centers that had been previously found. A Delaunay triangulation for a set of discrete points is a triangulation for which no point of the set stands inside the circumcircle of any triangle of the triangulation itself [36].
What was important for the calculation of the pore throat sizes was that each triangle had as vertices the grain centers and as sides the segments that connected the adjacent grain centers. As a result, the pore throat sizes could be calculated by subtracting from each side of the Delaunay triangles, the radii of the grains whose centers corresponded to the vertices of the considered side

$$r_{ij} = DT_{ij} - R_i - R_j \tag{3.47}$$

where r is the pore throat size and DT are the Delaunay triangle sides.
The average pore throat size was found by averaging the pore throat sizes obtained

$$r_{av} = \frac{r_{ij}}{n_{ij}} \tag{3.48}$$

As a final assessment the theoretical hydraulic conductivity according to the Kozeny-Carman formulation was calculated

$$K = \frac{D^2\phi^3}{180(1-\phi)^2}\frac{\rho g}{\mu} \tag{3.22}$$

The analyses that have been described were carried out on all the images acquired during the experiment; as a result, it was possible to verify the evolution over time of the calculated parameters during the dissolution of the rock-in-chip microfluidics.
The processing and analysis of the images were both carried out with a MATLAB code.

Chapter 4
Experimental Results

This chapter will present the results obtained during the experiments and the evaluations resulted from data analysis. Afterwards the presentation of the results, a discussion of them will follow.

4.1 Classic Microfluidic Hydraulic Properties Evaluation

The experiment aimed to determine the hydraulic conductivity of the porous medium mimicked by the PDMS microfluidic channel. Subsequently, hydraulic conductivity was compared to hydraulic conductivity derived from the Kozeny-Carman formulation. During the elaboration of the acquired data, the following values for the working fluid and porous medium properties were considered:

- gravitational acceleration was considered to be 9.81 m/s^2
- density of Milli-Q water - which was the working fluid - was considered to be 1000 kg/m^3
- viscosity of Milli-Q water was considered to be 1.00×10^{-3} Pa·s
- porosity of the porous medium of the microfluidic channel was considered to be 0.5, because the microfluidic channel was generated by replica molding from a master mold created to have a porosity of 0.5
- average grains diameter was considered to be 1.3×10^{-4} m because the microfluidic channel was generated by replica molding from a master mold with that average grains diameter

With regard to the geometric properties of the microfluidic channel and PVC connecting tubings, they have already been mentioned in previous chapters.
The driving force for the fluid flow was the pressure difference between the inlet reservoir and the outlet reservoir, provided by the pressure controller. However, for the calculation of hydraulic conductivity, the pressure difference between the two ends, inlet and outlet, of the microfluidic channel was considered. Figure 4.1 shows the pressure differences between the ends of the porous medium of the microfluidic device, after having calculated the pressure losses between the reservoirs and the microfluidic channel caused by the working fluid flow through the connecting PVC tubings. Thus, the pressure differences shown were the actual

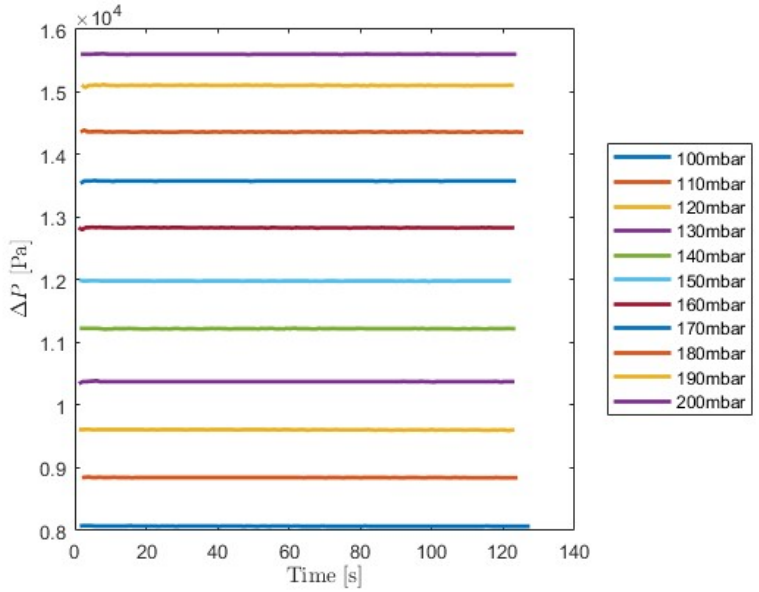

Figure 4.1 - Pressure differences between microfluidic channel's inlet and outlet

driving forces that were considered for each step of the experiment, as described in Section 3.1.

Figure 4.2 shows the mass measurements of the outlet reservoir recorded during the experiment as the pressure difference on the hydraulic circuit changed. The experiment was performed starting with the lower pressure difference - 100 mbar - and continued increasing the pressure difference at each step, so the final mass of each pressure step (t = 120 s) coincided with the initial mass of the next one (t = 0 s).

From the mass data shown in Figure 4.2, the volumetric fluid flow rate for each pressure difference was calculated (Figure 4.3).

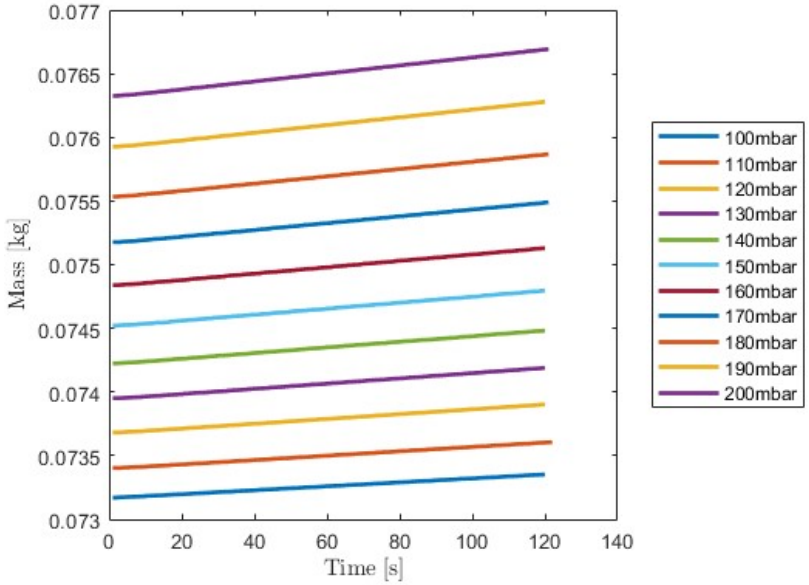

Figure 4.2 - Outlet reservoir's mass trends at different pressure differences

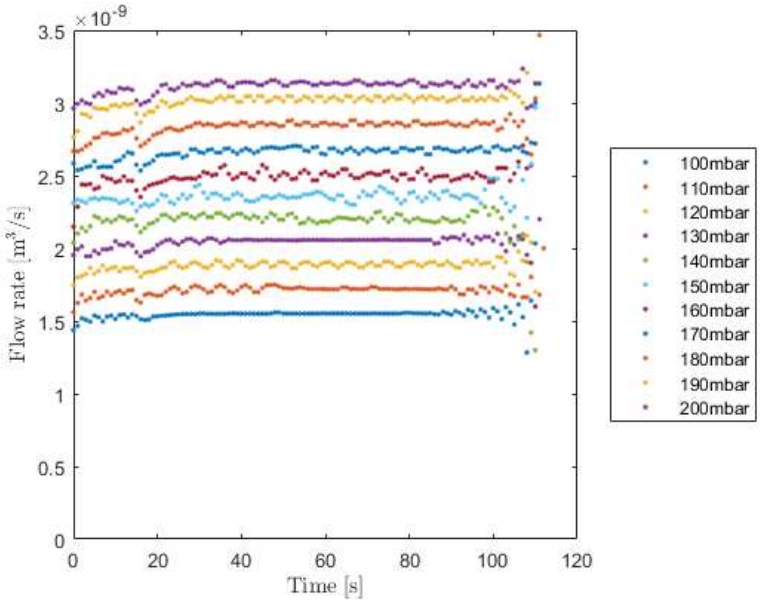

Figure 4.3 - Flow rates at different pressure differences

As it was logical to expect since the pressure difference - and therefore the driving force - was constant at each step of the experiment, the fluid flow rates remained constant throughout the time in which each pressure difference step was applied.
The average volumetric flow rate data were used to derive the Darcy velocity at each step, while the pressure difference between the microfluidic channel ends data were used to derive the hydraulic gradient at each step.
As a result, the couplings between Darcy velocities and respective hydraulic gradients were obtained and plotted on a graph that showed the Darcy velocity as a function of the hydraulic gradient (Figure 4.4). The points found were fitted with an interpolation straight line. In fact, from Equation 3.13, hydraulic conductivity was obtained as the slope of the interpolation straight line of the points, which related the Darcy velocity to the hydraulic gradient. From Figure 4.4 it is noted that the interpolation line for the raw data did not pass from the origin of the axes, conversely to what it would have been expected from the theory. As a matter of fact, Equation 3.13 implied that the interpolation line would have had to pass from the origin of the axes. The cause of this misalignment was a systematic bias caused by the flow control system - the pressure controller -. In fact, as already specified in Section 2.3.2, the pressure controller provided an extra pressure to the inlet and outlet reservoirs. However, it did not control the initial pressure level of the reservoirs before they were pressurized. Thus, the initial pressure level of the reservoirs was determined by the atmospheric pressure at which the reservoirs were located, and the height of the fluid column contained. In the preparation of the experimental apparatus, the inlet and outlet reservoirs were filled with approximately the same level of fluid. Nevertheless, a difference of a few mm between the two levels could have been considered possible. In addition, a small difference in the atmospheric pressure value related to the two reservoirs could have existed.
In order to verify that the misalignment of the interpolation line could have been justified by the explanation above, the value of hydraulic gradient i_0, which corresponded to null Darcy velocity, was considered. i_0 was 0.967, which corresponded, following Equation 3.14, to a

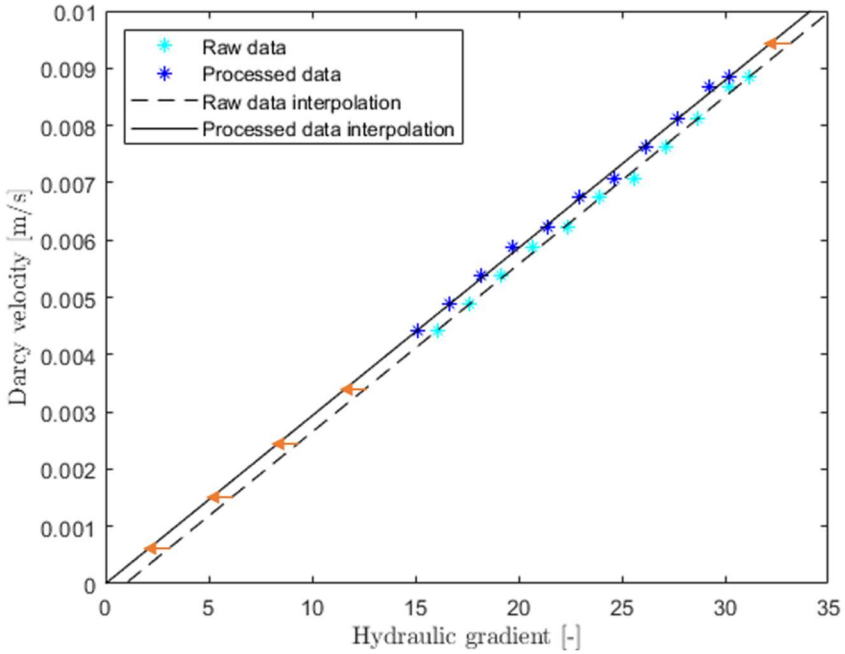

Figure 4.4 - Interpolation of data for the hydraulic conductivity calculation

hydraulic head of 49 mm. Part of this 49 mm may have been due to the difference in fluid levels between the reservoirs. In spite of this, it was assumed that the 49 mm was all due to the difference in atmospheric pressure between the reservoirs. This was done to verify that the maximum possible atmospheric pressure difference was not too high, which would have meant that it was not the motivation of misalignment between theory and practice. From Equation 3.16 the pressure difference corresponding to the 49 mm hydraulic head was calculated to be 4.84 mbar. This meant that a difference of 4.84 mbar – about 5/1000 of the atmospheric pressure of 1.013 bar - between the atmospheric pressures of the two tanks justified the misalignment between theory and practical results.

Since such a pressure difference was considered a plausible justification, it was decided to process the experimental data in such a way as to correct the systematic bias that was described. From a graphical point of view, the consequence of systematic bias was the horizontal translation of experimental data on the plane. For this reason, the experimental data - and therefore the interpolation line generated by them – was shifted horizontally by a value $i_0 = 0.967$ (red arrows in Figure 4.4). As a result, the interpolation line of the new processed data passed from the origin of the axes, as required by theory.

It should be noted that the data processing carried out did not influence the value of the calculated hydraulic conductivity. In fact, although the data processing involved the translation of the data points - thus of the interpolation line -, the hydraulic conductivity was not modified by the processing carried out because it corresponded to the slope of the interpolation line.

Table 4.1 shows the hydraulic conductivity values derived from the analysis of the experimental data and from the application of the Kozeny-Carman formula.

Table 4.1 Hydraulic conductivity from experimental data and from Kozeny-Carman formula

	Experimental result	Kozeny-Carman theoretical value
Hydraulic conductivity (mm/s)	0.2930 ± 0.0042	0.4605

4.1.1 Discussion of the Results

Table 4.1 shows that the hydraulic conductivity derived from the analysis of the data was of the same order of magnitude as the hydraulic conductivity calculated according to the Kozeny-Carman formulation. A priori, it was not expected that the two assessments were identical due to the differences between the model considered by Kozeny and Carman in the development of their formulation, and the physical characteristics of the PDMS microfluidic channel. Despite this, it was expected that the two values did not differ greatly because the porous medium mimicked by the PDMS microfluidic channel was considered quite well represented by the Kozeny-Carman model.
Therefore, it was inferred that:

- Kozeny-Carman's formula was suitable for the evaluation of the hydraulic conductivity of the microfluidic channel. In particular, the use of the average grain size of the porous medium as an estimate of the ratio of volume to surface of the medium was suitable for the evaluation of the friction opposite to the fluid flow by the porous medium that was being studied
- the experimental protocol applied allowed a good evaluation of the hydraulic conductivity of the porous medium under investigation

As a result, it was judged that the experimental method applied for the PDMS microfluidic channel could be a valid solution for the calculation of the hydraulic conductivity of the rock-in-chip microfluidics.

4.2 Particle Image Velocimetry on Classic Microfluidic Device

The PIV analysis was carried out with the aim of reconstructing the velocity field of a fluid flow through a porous medium in a microfluidic channel.
The parameters used for the PIV analysis were as follows:

- magnification = 50x
- passes for PIV analysis = 3
- initial window size = 128 pixels
- final window size = 32 pixels
- pixel size = 7.3 (μm/px) / 50 * 3 = 0.438 μm/px

The pixel size resulted from the original pixel size of the Nikon DS-Qi2 camera (7.3 μm/px), the magnification, and a correction factor (3) due to the resolution of the images acquired.

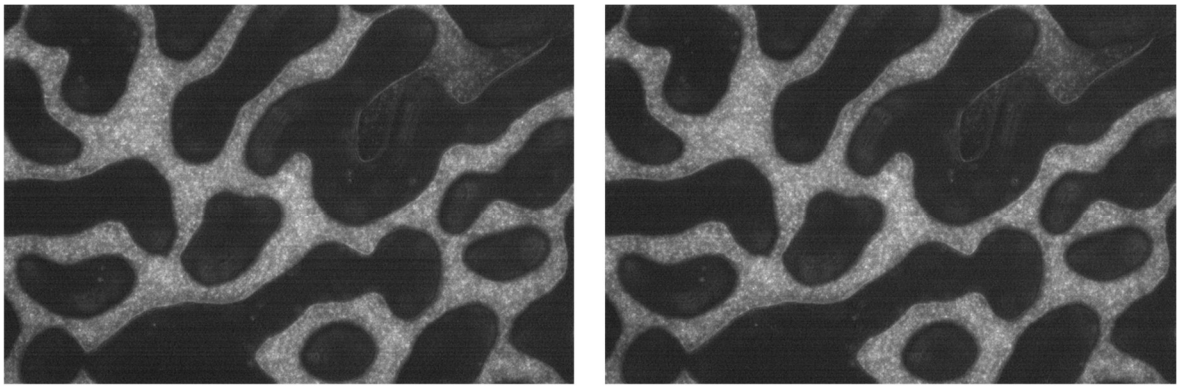

(a) (b)

Figure 4.5 - Images acquired under the microscope at successive times.
(a) image acquired at time t. (b) image acquired at time t+Δt

In fact, the camera could acquire images with a standard resolution of 4908x3264 pixel (full-pixel) or with a resolution of 1636x1088 pixel, with a 3x3 averaging. The correction factor was introduced because the images were acquired with the lower resolution available.
Figure 4.5 shows two images taken under the microscope in two successive instants of time in one of the 21 locations investigated. They were used to perform PIV analysis. Figure 4.5a was acquired at the instant of time t, while Figure 4.5b was acquired at the subsequent instant of time t+Δt. The time interval Δt between two successive images was not constant but depended on the acquisition properties of the employed camera. In this case, the time interval between two successive acquisitions was about 0.180 s.
In the images the large density of fluorescent tracer particles used - the white dots – can be seen. In fact, they were the only clearly visible elements because a fluorescent light was used to capture images.
For each location 150 images were taken. Subsequently, they were elaborated in order to obtain images that could be analysed more easily. Image processing generated the images shown in Figure 4.6.

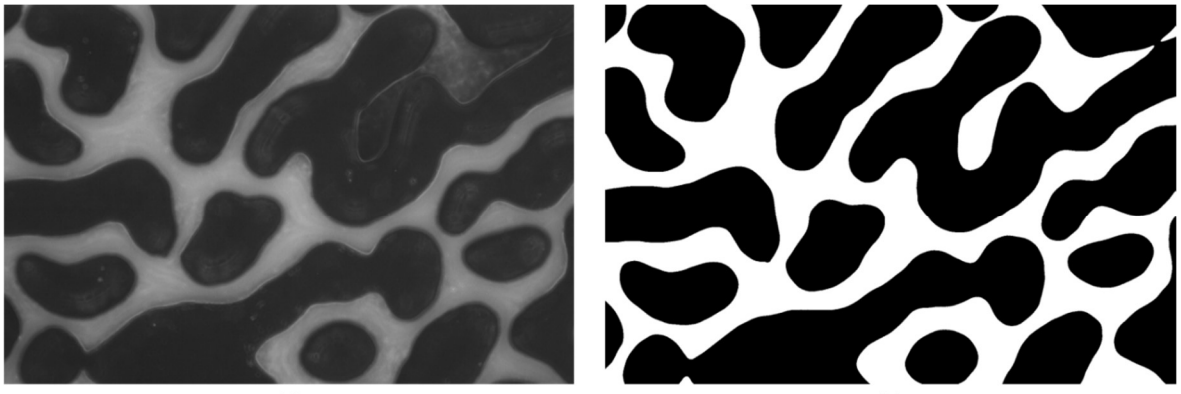

(a) (b)

Figure 4.6 - Images obtained from image processing. (a) background of the images obtained with averaging method. (b) mask of a location obtained with thresholding method

Figure 4.6a shows the average of the 150 images of a location obtained by the averaging method. It represented the background noise of the image series and was used to obtain the images to be analysed, according to Equation 3.30.
For Equation 3.30, the mask of each location was also used. Figure 4.6b shows the mask of a location: as it can be noted, the mask distinguishes the elements of an image according to the white or black color. In this case, black corresponded to the grains of the microfluidic channel, while white corresponded to the pores.

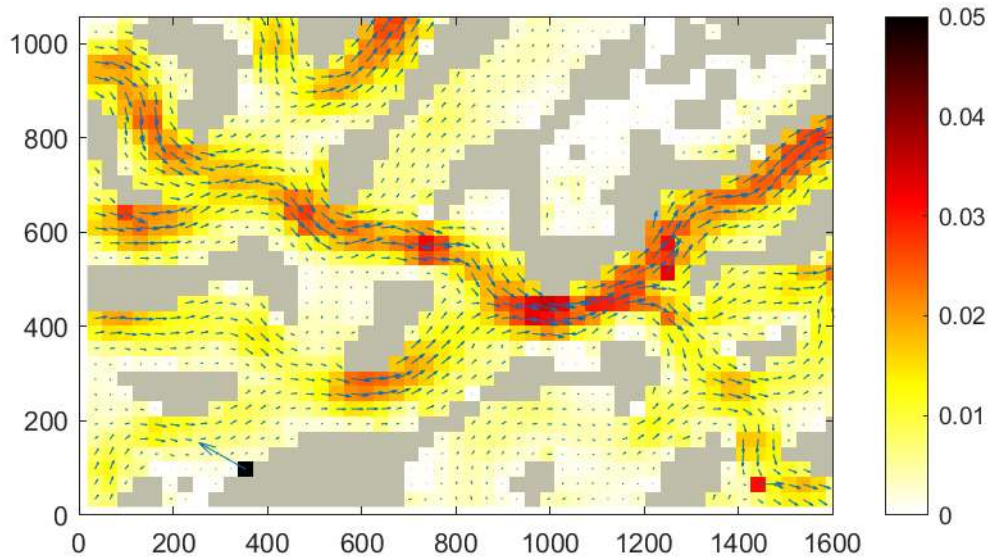

Figure 4.7 - Velocity field of a location in mm/s

After the analysis of the images obtained from the processing, the velocity field for each location was derived. Figure 4.7 shows the velocity field resulting from the analysis of the above images in one location. In the image, each investigation window has a color that depends on the velocity magnitude in that window. In addition, the blue arrows report the direction of the velocity vectors in each of the investigation windows.
The orange and red coloured interrogation windows were those where velocity was higher, thus preferential fluid flow paths could be identified.
Figure 4.8 shows the reconstruction of the velocity field in all locations for which the PIV analysis was performed. In this figure it is evident the presence of preferential pathways of the flow inside the microfluidic channel, thanks to the different coloring of the interrogation windows.
The average velocity within the microfluidic channel was calculated by averaging the velocities of each interrogation window. At the same time, the expected average velocity was calculated from the flow rate imposed by the syringe pump. The results are shown in Table 4.2.

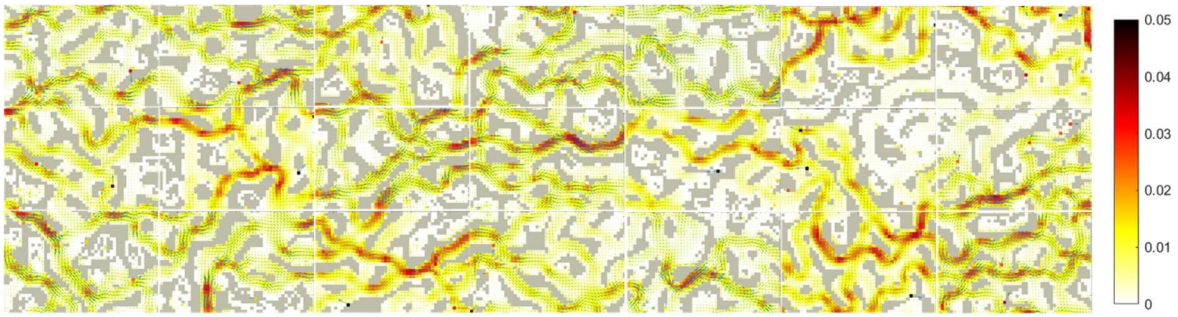

Figure 4.8 - Overall velocity field in all the locations in mm/s

Table 4.2 - Average velocity within the microfluidic channel

	PIV result	Derived from imposed flow rate
Average velocity (mm/s)	0.0051	0.0048

4.2.1 Discussion of the Results

Table 4.2 shows that the average velocity obtained from the PIV analysis was very similar to the expected average velocity. Therefore, it could be considered that the processing and analysis of images led to reliable results. For this reason, the PIV analysis method developed could be used during the experimentation of rock-in-chip microfluidics, in order to obtain the velocity field of the working fluid within it.
In the experimentation of the rock-in-chip microfluidics during the rock dissolution, it would have been interesting to be able to compare the velocity field, whose result would have been similar - as pattern - to Figure 4.8, and the areas of the porous medium where dissolution was greatest. However, as already explained in Section 3.3, it was not possible to perform PIV analysis for rock-in-chip microfluidics. Nevertheless, it can be explained what the expected results would have been if the analysis could have been carried out. Considering a velocity map similar to Figure 4.8, the greater rock dissolution would have been expected in areas where PIV analysis would have shown the presence of preferential flow pathways, in other words, in red-coloured areas. In fact, zones of microfluidic channel in which the velocity was of an order of magnitude greater than the average velocity can be seen. Indeed, as already explained in Section 3.2, preferential flow paths were expected to be subjected to greater dissolution for two reasons:

- the greater flow rate would have contributed to provide new acid reagent for the dissolution reaction
- the greater flow rate would have carried away the concentration of dissolved calcite in the surroundings of the dissolution zones, thus favoring the dissolution reaction

In addition, if the PIV analysis had been repeated at intervals of time during the dissolution of the porous medium, it would have been expected that preferential flow pathways could have changed, thus resulting in new preferential dissolution zones.

Therefore, by coupling PIV analysis and dissolution analysis, one could reconstruct the complex dynamics of dissolution in a porous medium and predict which areas would be subject to a higher dissolution rate.

4.3 Rock-in-chip Microfluidics Experimentation

The aim of the rock-in-chip microfluidics experiment was to demonstrate that the fabrication methodology of the microfluidic device was effective in allowing the experimental derivation of the properties of the porous medium during dissolution. The experimental part was divided into two distinct phases:

- the evaluation of the hydraulic conductivity of the microfluidic channel following the same method employed for the classic PDMS microfluidic device
- the evaluation of average radius, average pore throat size, porosity and theoretical hydraulic conductivity according to Kozeny-Carman formula employing image analysis during rock dissolution

During the elaboration of the acquired data, the following values for the working fluid and porous medium properties were considered:

- gravitational acceleration was considered to be 9.81 m/s^2
- density of the working fluid was considered to be 1000 kg/m^3, since the working fluid was mainly made up of Milli-Q water
- viscosity of the working fluid was considered to be 1.00 x 10^{-3} Pa·s, for the same reason

Instead, in contrast to what was done for the classic PDMS microfluidic channel, for the porosity the value resulting from the image analysis of the second part of the experiment was used, not the nominal value from the microfluidic channel manufacturing. As a result, the porosity was 0.68. Moreover, the rock-in-chip microfluidics height - corrected for the residual rock layer and the PDMS pressure - was $2 \cdot 10^{-5}$ m (20 μm).
The geometric properties of the elements used have already been specified in the previous sections.

4.3.1 Results for the Hydraulic Conductivity

By analogy with Section 4.1, the driving force for fluid flow within the rock-in-chip microfluidics was the pressure difference between the inlet and outlet reservoir, provided by the pressure controller. Since the pressure difference between the rock-in-chip microfluidics' ends (Figure 4.9) was of interest for the evaluation of hydraulic conductivity, it was obtained by calculating the pressure losses in the PVC connecting tubings.
From the Figure 4.9 it can be noted the increasing linear trend that was set for the pressure difference, along a time of 600 s.

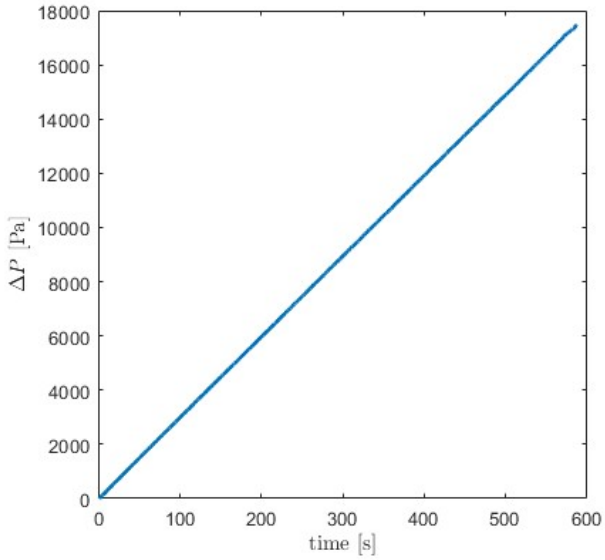

Figure 4.9 - Pressure differences between rock-in-chip microfluidics ends

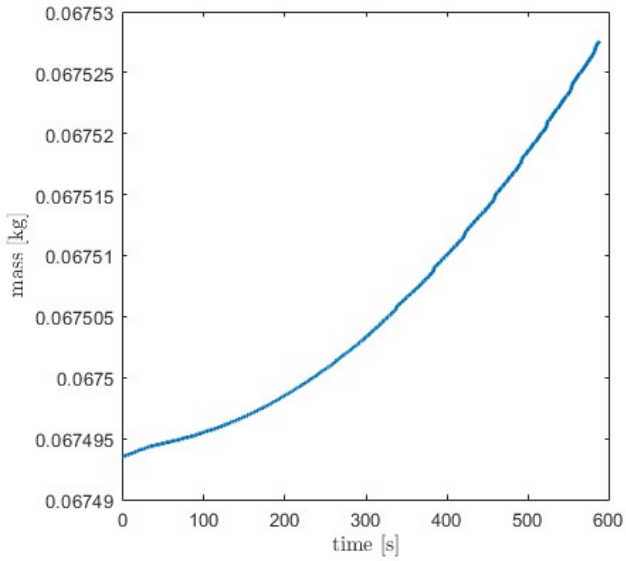

Figure 4.10 - Outlet reservoir's mass measurement

Figure 4.10 shows the mass of the outlet reservoir, measured by the scale: its trend reflected the increasing pressure difference imposed. From the mass data, the volumetric flow rate was calculated (Figure 4.11).
From the volumetric flow rate shown in Figure 4.11, the Darcy velocity was assessed. From the pressure difference between the ends of the rock-in-chip microfluidics, the hydraulic gradient was derived. As a result, the Darcy velocity corresponding to the hydraulic gradient was calculated for each instant of time (Figure 4.12).

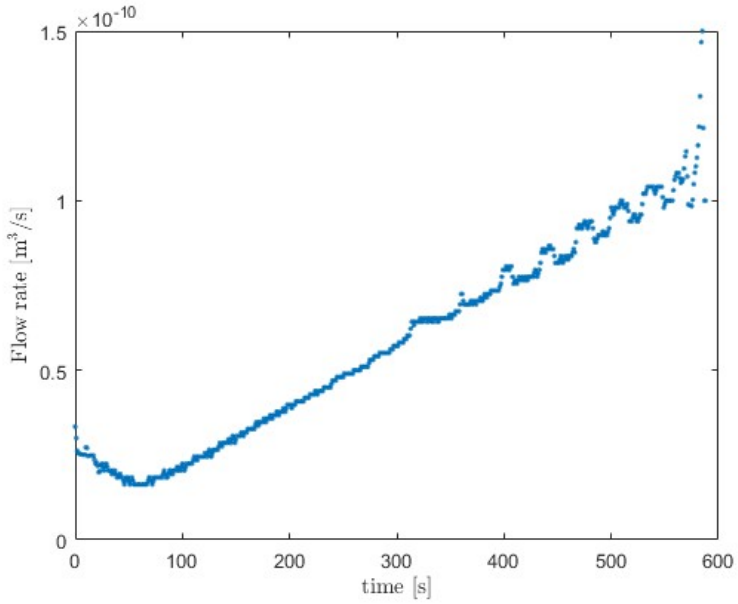

Figure 4.11 - Flow rate over time

The points found were fitted with an interpolation straight line: the slope of the line was the hydraulic conductivity, according to Equation 3.13. However, for the construction of the interpolation line, not all the points in Figure 4.12 were taken into account: in fact, the points obtained from the measurements of the first 60 s were excluded from the analysis because they reproduced a tendency in disagreement with the theory, due to the initial instability of the system.

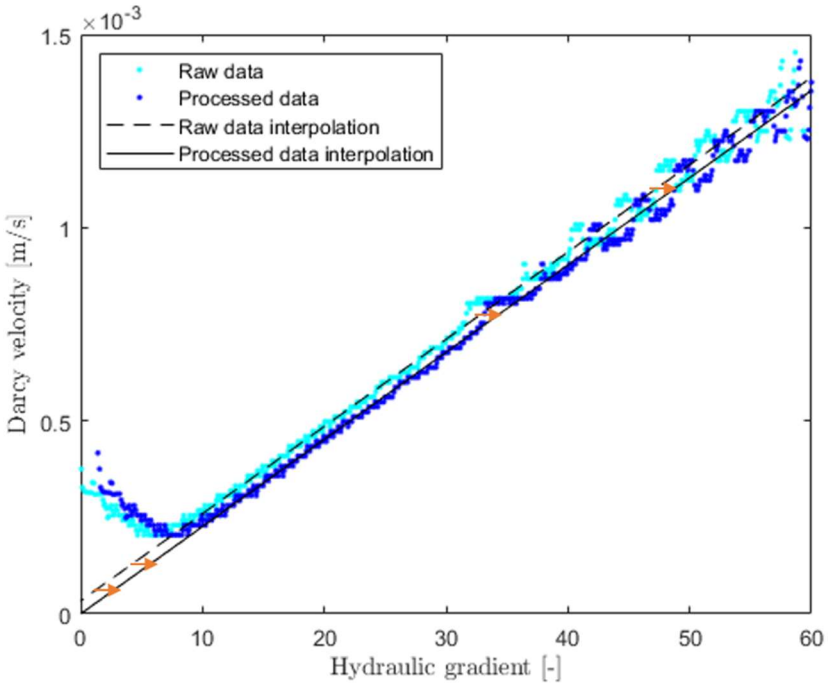

Figure 4.12 - Interpolation of data for the hydraulic conductivity calculation

In addition, the data was processed in order to eliminate misalignment of the interpolation lines with respect to the origin of the axes, due to systematic bias discussed in Section 4.1. The data processing, which did not involve any change in the evaluation of hydraulic conductivity, was carried out in the same way as before.
In this case it resulted that i_0 was -1.4861, corresponding to a hydraulic head of 45 mm, which meant a pressure difference of 4.37 mbar. In Figure 4.12, the red arrows show the translation applied to the experimental data.
Table 4.3 shows the hydraulic conductivity values derived from the analysis of the experimental data and from the application of the Kozeny-Carman formula, recalling that in this case the estimated height of the rock-in-chip microfluidics was considered as characteristic dimension of the flow through the porous medium.

Table 4.3 - Hydraulic conductivity from experimental data and from Kozeny-Carman formula

	Experimental result	Kozeny-Carman theoretical value
Hydraulic conductivity (mm/s)	0.0226 ± 0.0001	0.0669

4.3.2 Results for Rock-in-chip Microfluidics Dissolution

In the second phase of the experiment, the analysis of the microscope images was performed. The microscope parameters were as follows:

- magnification = 10x
- pixel size = 6.5 (μm/px) / 10 = 0.65 μm/px

The pixel size resulted from the pixel size of the Hamamtsu ORCA flash 4.0 v3 camera (6.5 μm/px) and the magnification employed.
The images were captured in two configurations:

- fluorescence images, with the aim of distinguishing the fluorescent element – the working fluid – from the non-fluorescent element – the grains of the rock-in-chip microfluidics –
- bright-field images

However, only fluorescent images were analysed, while bright-field images were not subjected to quantitative analysis.
Figure 4.13 shows a series of fluorescent images acquired during the experiment: the 4.13a was acquired at the beginning of the experiment, the 4.13b was acquired at halfway of the experiment - after 720 minutes -, the 4.13c was acquired at the end of the experiment - after 1440 minutes -. From the images it is possible to notice that the fluorescent power of the working fluid decreased during the experiment, thus the image processing has been more complicated than expected. In fact, the lower fluorescence of the working fluid resulted in a

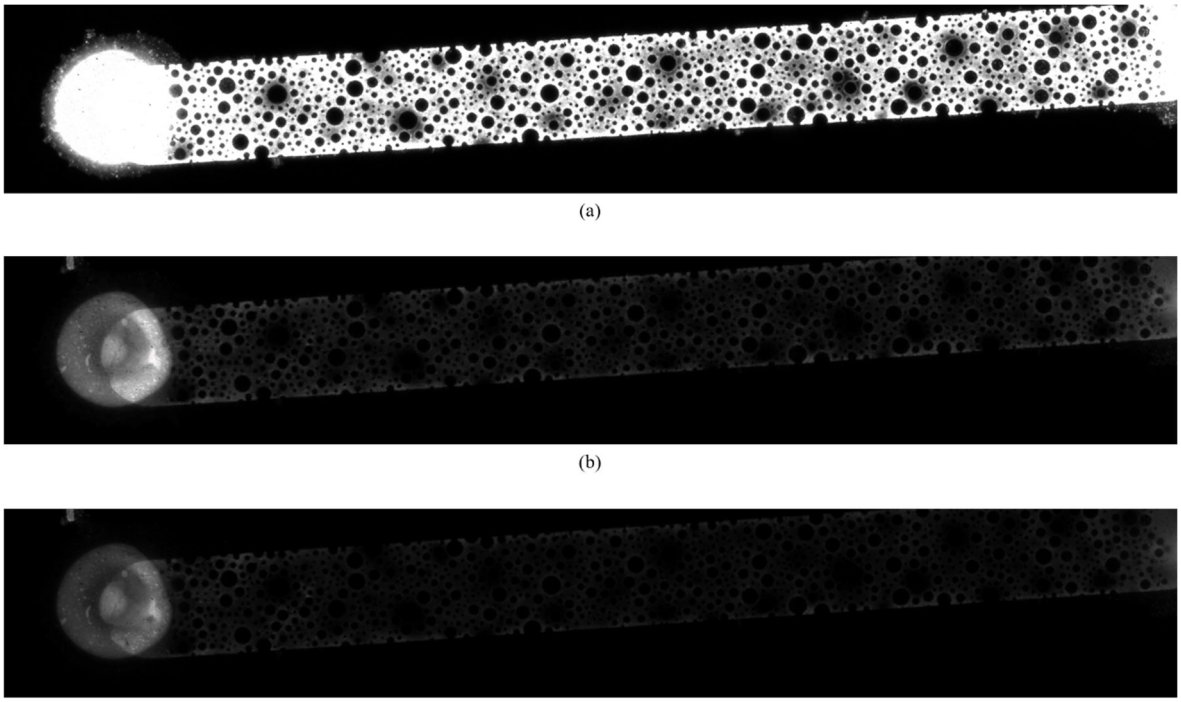

Figure 4.13 - Fluorescent images of rock-in-chip microfluidics. (a) t=0 min. (b) t=720 min. (c) t=1440 min

smaller difference between the pixel intensity of the images - especially in areas of the channel where the fluid flow was less favored -, making thresholding difficult. Probably, this was one of the main reasons why it was necessary to perform an adaptive thresholding, as explained in Section 3.3.4.
An explanation for the decrease in the fluorescence of the working fluid will be provided in the discussion of the results (Section 4.3.3).
Figure 4.14 shows the result of the adaptive thresholding: it can be noted that the value of threshold had rather different values in distinct zones of the rock-in-chip microfluidics. In addition, it shows the identification of rock-in-chip microfluidics' grains as red circles.

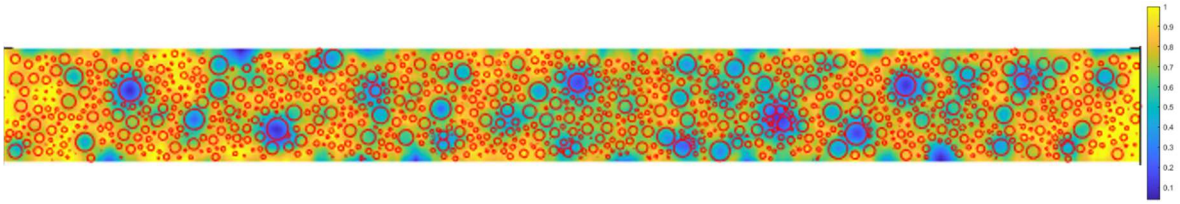

Figure 4.14 - Value of adaptive threshold along the channel and identification of circular grains

The obtained rock-in-chip microfluidics mask is shown in Figure 4.15. Comparing the mask of the rock-in-chip microfluidics and the fluorescent images of it, it can be noticed that the geometry of the microfluidic channel was well represented by the mask: this was already a first success for the experiment. Due to this, the study of the rock-in-chip microfluidics through image analysis was possible.

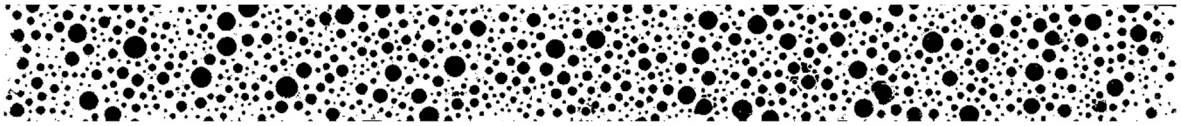

Figure 4.15 - Mask of the rock-in-chip microfluidics

The properties of the rock-in-chip microfluidics, object of investigation, were derived from the analysis of the above images.

Figure 4.16 shows the variation of the average grain radius over time, which had an unexpected trend. In fact, the average grain radius was expected to decrease during the experiment, due to the dissolution of the rock. On the contrary, it started to increase, followed by a stabilization at a constant value.

The average pore throat size - shown in Figure 4.17 - followed a different, but also unexpected, trend during dissolution. In fact, it reached a peak and subsequently returned to a stable value similar to the initial one. Contrary to this, the average pore throat size was expected to increase during the experiment, due to the reduction in grain size because of the dissolution.

In line with what has been written, porosity was expected to increase: the volume of voids had to increase due to dissolution, causing the ratio of volume of voids to total volume – the porosity – to increase. Instead, Figure 4.18 shows an initial decreasing trend, followed by a stabilization at a constant value. It should be noted that the porosity trend is in line with the average grain radius one.

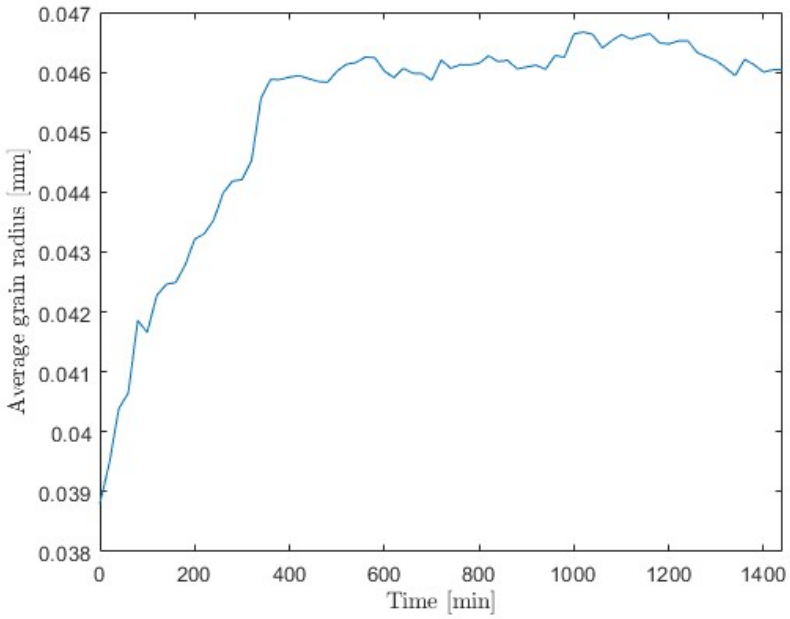

Figure 4.16 - Average grain radius over time

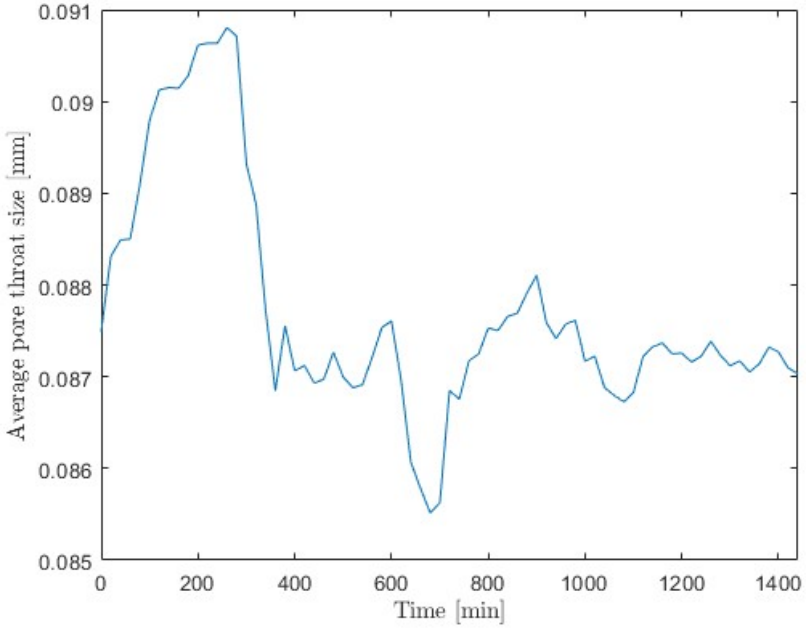

Figure 4.17 - Average pore throat size over time

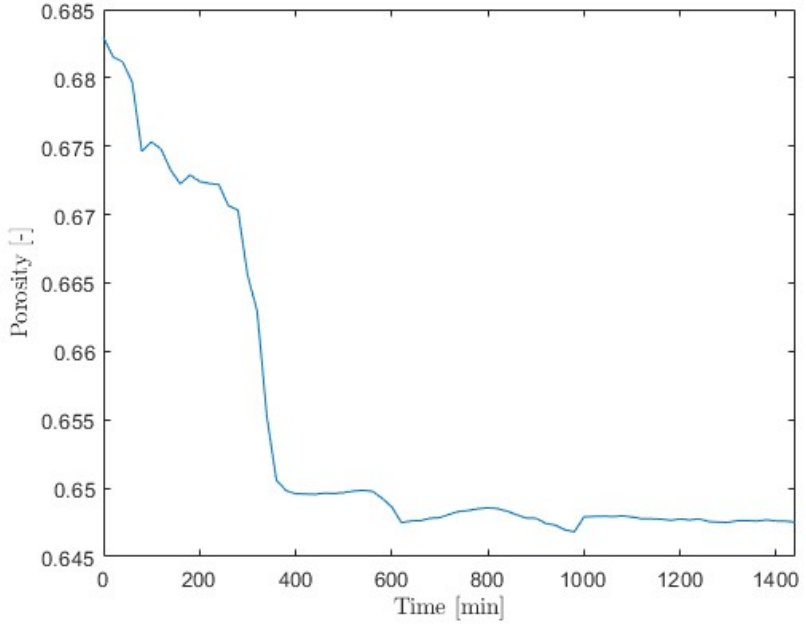

Figure 4.18 - Porosity over time

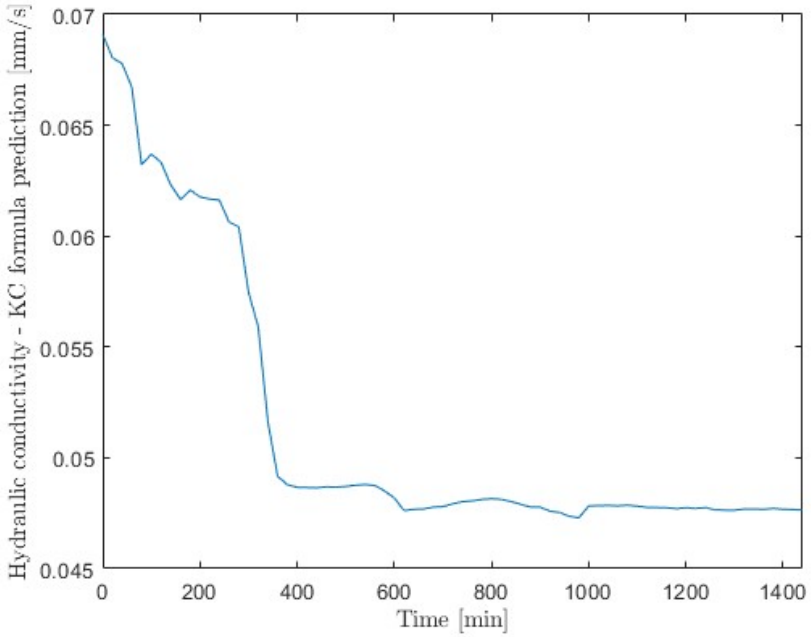

Figure 4.19 - Kozeny-Carman hydraulic conductivity over time

Regarding hydraulic conductivity (Figure 4.19) – assessed according to the Kozeny-Carman formula –, the trend was equal to the one of porosity. The equal trend of porosity and hydraulic conductivity according to Kozeny-Carman was an expected result: in the Kozeny-Carman formula, in fact, only porosity was a variable parameter, as the height of the rock-in-chip microfluidics – supposed to be constant during the experiment - was considered for the characteristic dimension for the flow. Although the hydraulic conductivity was expected to increase during the experiment, it initially decreased, and then it stabilized at a value similar to the initial one.
Thus, the evolution of the considered rock-in-chip microfluidics' parameters did not follow the expectations for rock dissolution: in the next paragraph an explanation for these peculiar behaviours will be given.

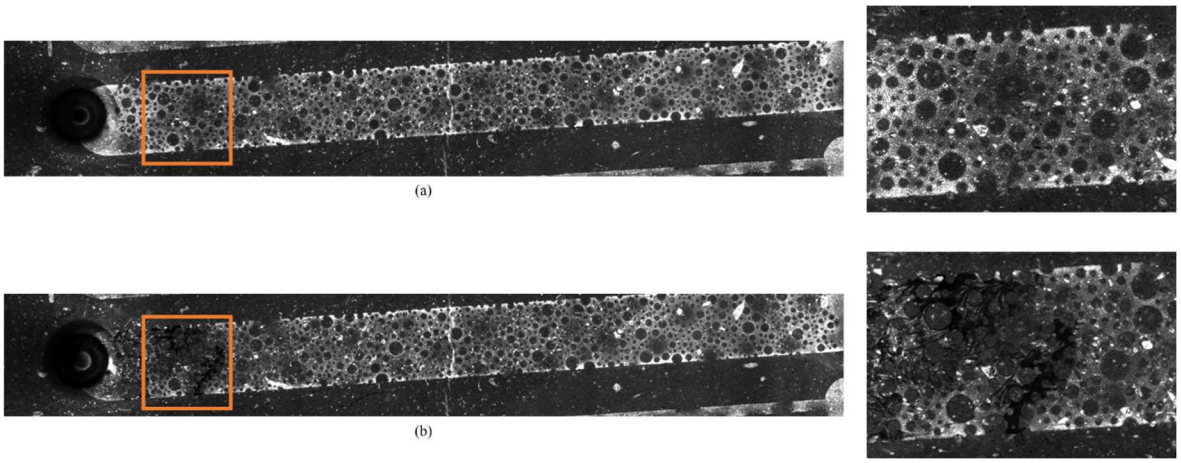

Figure 4.20 - Bright-field images of rock-in-chip microfluidics and details. (a) t = 0 min. (b) t = 1440 min.

Figure 4.20 shows two bright-field images of rock-in-chip microfluidics: Figure 4.20a was acquired at the beginning of the experiment, while Figure 4.20b was acquired at the end of the experiment, after 1440 minutes.
As previously stated, these images were not analysed, however some qualitative considerations can be made. In particular, observing the highlighted detail of the images, it is possible to notice a change of the image between the beginning and the end of the experiment. In fact, at the beginning of the experiment the image appears to be fairly homogeneous; on the contrary, in the image acquired after 1440 minutes, it is noted that in the highlighted detail there are dark areas in the porous medium. Those areas were hypothesized to be zones where the residual rock layer at the base of the rock-in-chip microfluidics had been dissolved by the working fluid. In addition, the location of this dissolution zones – close to the inlet of the rock-in-chip microfluidics – were in accordance with what was expected from the dissolution behaviour. In fact, the acid fluid entered the rock-in-chip microfluidics and began to dissolve the rock, consuming the H^+ ions, as per Equation 3.39. For this reason, the subsequent area of the rock-in-chip microfluidics was less dissolved.

4.3.3 Discussion of the Results

Table 4.3 shows the hydraulic conductivity derived both from experimental data analysis and from Kozeny-Carman formula evaluation. As already stated, the Kozeny-Carman evaluation was considered in order to have an idea about the order of magnitude of what the hydraulic conductivity obtained experimentally should have been. Indeed, especially for the rock-in-chip microfluidics, the Kozeny-Carman model did not fit with the actual geometry of the microfluidic channel. The theoretical model, in fact, was based on a porous medium consisting of identical spheres arranged homogeneously: it is clear from the rock-in-chip microfluidics' acquired images that the actual geometry was different from the one of the model. The experimental procedure used to calculate the hydraulic conductivity of the rock-in-chip microfluidics was considered successful: in fact, the experimental value had the same order of magnitude as the theoretical evaluation. As a result, the definition of an experimental protocol for the evaluation of hydraulic conductivity - and therefore of permeability - for the novel rock-in-chip microfluidics was successfully fulfilled.
Regarding the second experimental phase with rock-in-chip microfluidics, the goal was twofold:

- the validation of an experimental protocol to evaluate the properties of a porous medium by performing image analysis
- the verification of the effects of the dissolution of a porous medium on the properties of the porous medium itself

From what has been explained in Section 4.3.2, it appears that the experimental protocol was successful. In fact, starting from images acquired under the microscope, new analyzable images were built. The processed images faithfully reflected the original geometry of the rock-in-chip microfluidics, hence their analysis allowed to evaluate some characteristic

properties of a porous medium, such as the size of the grains, the size of the pore throats and the porosity.
Instead, with regard to the evaluation of the properties of rock-in-chip microfluidics while rock dissolution was underway, the results were contrasting. On the one hand, it was found that the properties of the porous medium could be quantified during dissolution. On the other hand, from the figures in Section 4.3.2, it was deduced that the trend of the properties taken into consideration (average grain radius, average pore throat size, porosity, hydraulic conductivity according to Kozeny-Carman) did not follow the expected tendency during dissolution. Indeed, they initially varied, but they stabilised at constant values after about 350 minutes.
These evolutions could suggest either an error in image analysis or the failure of the dissolution of the rock-in-chip microfluidics. However, both hypotheses were unfounded. In fact, nothing suggested that the images were incorrectly analyzed: all the processed images that were analysed faithfully reproduced the geometry of the microfluidic channel; all element of rock-in-chip microfluidics were identified during processing.
In addition, the bright-field images in Figure 4.20 show that dissolution took place, at least as regards the residual rock layer at the base of the microfluidic channel.
For these reasons, the explanation of the results of the experiment had to be looked for elsewhere.
Figure 4.21 shows the mass measurement of the outlet reservoir during the experiment. In the first 300 minutes, it reflected what was expected due to the pressure difference imposed by the pressure controller: a slower increase initially – when the pressure difference was 10 mbar – and a larger increase after an hour – when the pressure difference was 180 mbar –.

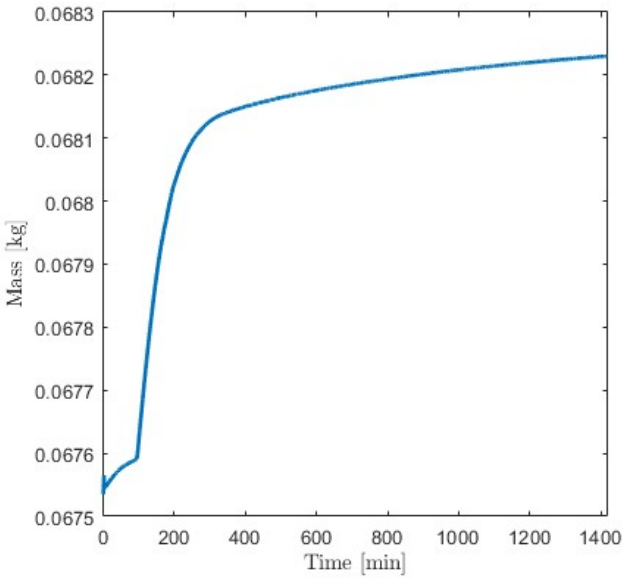

Figure 4.21 - Mass measurement of outlet reservoir during dissolution experiment

However, after about 350 minutes from the beginning of the experiment, the increase in mass slowed down considerably – therefore the fluid flow rate –, as if the pressure difference between the inlet and outlet reservoir had been decreased, which did not happen. The slowing of the mass increase coincided with the stabilization of the parameters, whose trends were shown in Section 4.3.2. Thus, the stabilization of the parameters was most likely caused by the slowing of the increase in mass – therefore by the decrease in fluid flow rate – which caused the dissolution to stop probably.
The decrease in fluid flow rate could have two causes. The first, for which there could be no material evidence, was the detachment of some fragments of rock from the areas where the rock was dissolving, probably from the residual rock layer. Subsequently, the rock fragments would be wedged inside the microfluidic channel, blocking the passage of the fluid.
Instead, the second – and most likely – cause had photographic evidence shown in Figure 4.22. In fact, the figure shows a photograph taken at the inlet reservoir – containing the rock dissolving solution – at the end of the experiment: the presence of an orange powder is visible. It was fluorescein powder that had come out of the solution. The reason why fluorescein came out of the solution was probably the acidity of the solution itself, although no similar situations were found in literature.
As a result, the fluorescein powder, settling, partially clogged both the connecting tubing, between the inlet reservoir and the rock-in-chip microfluidics, and the rock-in-chip microfluidics channel, thus preventing the normal flow of the working fluid.
This would also explain the decrease of the luminous intensity of Figure 4.13. In fact, fluorescein loses its fluorescent power when exposed to fluorescent light for a long time. Therefore, the lack of new fluid supply – due to the obstruction of the hydraulic circuit – caused the lost fluorescence capacity of fluorescein, which remained exposed to fluorescent light for hours.

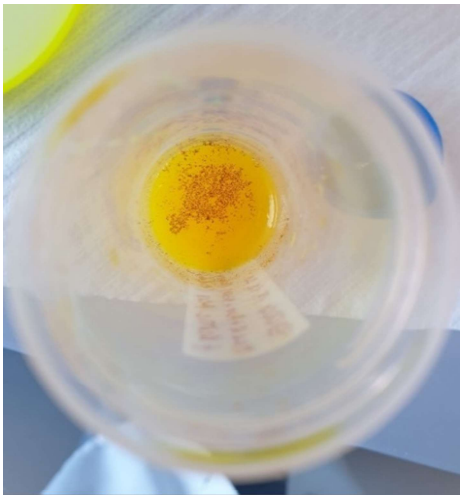

Figure 4.22 - Photograph of the inlet reservoir at the end of the experiment

Chapter 5
Conclusions and Future Directions

Interest in the use of microfluidic devices for the study of reactive transport phenomena within porous media has grown in recent times. However, scientific research is mainly limited to the use of microfluidic devices fabricated with materials such as glass, quartz, poly(methyl methacrylate) (PMMA), PDMS and silicone.
Microfluidic devices have also been used to study the dissolution reaction of rocks. However, since classical microfluidic devices were employed, the rock dissolution had to follow its previous precipitation: reactive solutions were injected into the microfluidic device resulting in the precipitation of the rock; the subsequent injection of acidified water conducted to its dissolution [4].
This thesis proposed the fabrication and use of a novel microfluidic device: the rock-in-chip microfluidics. In addition, an experimental protocol has been proposed and validated for the use of the novel rock-in-chip microfluidics for the observation and the quantification of natural rock dissolution.
In particular, the focus was on the evaluation of the porous medium's properties - such as hydraulic conductivity, grain size, pore throat size and porosity - useful for the characterization of dissolution phenomena of a porous medium.
The main feature of the rock-in-chip microfluidics is the designing onto a natural rock surface. In this way, the study of reactive transport phenomena in porous media can take place in a real porous medium, and not in a medium that mimic a porous medium.
Initially (Section 3.1), an experimental setup in order to evaluate the hydraulic conductivity of a classic PDMS microfluidic device was built. It was validated by comparing the results obtained experimentally with a theoretical evaluation of hydraulic conductivity according to the Kozeny-Carman formula (Section 4.1). Thus, the experimental methodology was deemed suitable for testing on the rock-in-chip microfluidics.
Subsequently (Section 3.2), the processing and analysis of images acquired under the microscope were used to develop a PIV analysis for a fluid flow within a classic PDMS microfluidic device. The methodology to perform the PIV analysis - validated in Section 4.2 - was intended to be applied to the study of rock-in-chip microfluidics, with a twofold objective:

- determine the velocity field within a porous medium and evaluate the relationship between velocity field and dissolution zones in the rock-in-chip microfluidics

- verify the evolution of the velocity field over time, resulting from the rock dissolution

Although the methodology proved to be successful applied to the classic microfluidic device in PDMS, it could not be applied to the rock-in-chip microfluidics due to issues related to the manufacturing of rock-in-chip microfluidics itself.
In the final part of the work (Section 3.3), experimental setups and methodologies, validated for classic PDMS microfluidic devices, have been applied and tested for the study of rock-in-chip microfluidics, in order to:

- verify the quality of the fabrication of rock-in-chip microfluidics and evaluate its hydraulic conductivity

- evaluate the properties of a porous medium and their evolution due to the dissolution of rock-in-chip microfluidics, employing for this purpose the processing and analysis of images acquired under a microscope

The results (Section 4.3) show that:

- the manufacturing of the rock-in-chip microfluidics was such that a complete experimentation could be carried out with its employment

- the experimental setup developed allowed the evaluation of parameters of rock-in-chip microfluidics useful for the study of transport phenomena within porous media

- the employment of image analysis allowed the observation of the natural rock dissolution and the evaluation of the evolution of the rock-in-chip microfluidics properties for the quantification of dissolution

The novel rock-in-chip microfluidics has proven successful for the applications tested in this thesis, however some improvements can be made for future applications.
One aspect to work on is the fabrication of rock-in-chip microfluidics: an improvement of the rock etching would allow to obtain a rock-in-chip microfluidics without the residual layer of rock, present in the prototype tested in this work. As a result, the PIV analysis could be carried out, further expanding the study possibilities available.
In addition, an improvement of the method of visual detection of the working fluid is required: as highlighted in Section 4.3.3, in fact, fluorescein came out of solution from the acid solution in which it was dissolved, complicating the course of the experiment.
The novel rock-in-chip microfluidics could be used for the study of reactive transport in porous media. In particular, it could be of interest both for the prediction of the fluids flow in porous media in the presence of dissolution and for the development and employing of fluids to be injected to control the dissolution of porous media.

Acronyms & Symbols

A	section of microfluidic channel
av	average
a_v	specific surface area
C	empirical constant
D	diameter of equivalent spherical particle
d_p	diameter of the particle
DT	Delaunay triangle side
dx	displacement in x direction
dy	displacement in y direction
E	expected value
FFT	Fast Fourier Transform
g	acceleration due to gravity
G	noisy image
GF	Gaussian function
H	height of microfluidic channel
h	hydraulic head
i	hydraulic gradient
I	image
in	inlet
K	hydraulic conductivity
k	permeability
L	length
l	length of microfluidic channel
loc	location
m	mass
$\dot{m}$	mass flow rate
M	mask
MAL	major axis length
mal	minor axis length
n	number of elements
N	noise of the image
n_p	number of pixels
out	outlet
PDMS	Polydimethylsiloxane
PIV	Particle Image Velocimetry
PMMA	poly(methyl methacrylate)
PTV	Particle Tracking Velocimetry

px	value of pixel
Q	volume flow rate
q	Darcy velocity
R	radius
r	pore throat
t	time
tbg	tubing
u	velocity vector magnitude
U_g	gravitationally induced velocity
v	velocity
V	volume
V_v	volume of voids
v_x	velocity in x direction
v_y	velocity in y direction
w	width of microfluidic channel
z	elevation
μ	dynamic viscosity
ρ	density
σ	variance
σ_s	sphericity of a particle
τ	threshold value
φ	porosity
ω	probability

Bibliography

[1] C. T. Gerold, A. T. Krummel, and C. S. Henry, "Microfluidic devices containing thin rock sections for oil recovery studies," *Microfluid. Nanofluidics*, vol. 22, no. 7, pp. 1–7, 2018, doi: 10.1007/s10404-018-2096-7.

[2] R. Singh *et al.*, "Real rock-microfluidic flow cell: A test bed for real-time in situ analysis of flow, transport, and reaction in a subsurface reactive transport environment," *J. Contam. Hydrol.*, vol. 204, no. August, pp. 28–39, 2017, doi: 10.1016/j.jconhyd.2017.08.001.

[3] Y. A. Alzahid *et al.*, "Functionalisation of Polydimethylsiloxane (PDMS)-Microfluidic Devices coated with Rock Minerals," *Sci. Rep.*, vol. 8, no. 1, pp. 1–15, 2018, doi: 10.1038/s41598-018-33495-8.

[4] H. Yoon, K. N. Chojnicki, and M. J. Martinez, "Pore-Scale Analysis of Calcium Carbonate Precipitation and Dissolution Kinetics in a Microfluidic Device," *Environ. Sci. Technol.*, vol. 53, no. 24, pp. 14233–14242, 2019, doi: 10.1021/acs.est.9b01634.

[5] J. Friend and L. Yeo, "Fabrication of microfluidic devices using polydimethylsiloxane," *Biomicrofluidics*, vol. 4, no. 2, 2010, doi: 10.1063/1.3259624.

[6] J. Bear, *Dynamics of Fluids in Porous Media*. Dover Publications, 1972.

[7] H. Abdulmouti and T. M. Mansour, "The technique of PIV and its applications," *10th Int. Conf. Liq. At. Spray Syst. ICLASS 2006*, pp. 1–10, 2006.

[8] A. Anbari, H. T. Chien, S. S. Datta, W. Deng, D. A. Weitz, and J. Fan, "Microfluidic Model Porous Media: Fabrication and Applications," *Small*, vol. 14, no. 18, pp. 1–15, 2018, doi: 10.1002/smll.201703575.

[9] A. Gerami *et al.*, "Microfluidics for Porous Systems: Fabrication, Microscopy and Applications," *Transp. Porous Media*, vol. 130, no. 1, pp. 277–304, 2019, doi: 10.1007/s11242-018-1202-3.

[10] N. K. Karadimitriou and S. M. Hassanizadeh, "A Review of Micromodels and Their Use in Two-Phase Flow Studies," *Vadose Zo. J.*, vol. 11, no. 3, p. vzj2011.0072, 2012, doi: 10.2136/vzj2011.0072.

[11] F. G. Ergin, B. B. Watz, and N. F. Gade-Nielsen, "A review of planar PIV systems and image processing tools for lab-on-chip microfluidics," *Sensors (Switzerland)*,

vol. 18, no. 9, pp. 1–23, 2018, doi: 10.3390/s18093090.

[12] J. Wu, G. Zheng, and L. M. Lee, "Optical imaging techniques in microfluidics and their applications," *Lab Chip*, vol. 12, no. 19, pp. 3566–3575, 2012, doi: 10.1039/c2lc40517b.

[13] S. Pradhan, I. Shaik, R. Lagraauw, and P. Bikkina, "A semi-experimental procedure for the estimation of permeability of microfluidic pore network," *MethodsX*, vol. 6, no. December 2018, pp. 704–713, 2019, doi: 10.1016/j.mex.2019.03.025.

[14] N. S. Kumar Gunda, B. Bera, N. K. Karadimitriou, S. K. Mitra, and S. M. Hassanizadeh, "Reservoir-on-a-Chip (ROC): A new paradigm in reservoir engineering," *Lab Chip*, vol. 11, no. 22, pp. 3785–3792, 2011, doi: 10.1039/c1lc20556k.

[15] S. Gogoi and S. B. Gogoi, "Review on microfluidic studies for EOR application," *J. Pet. Explor. Prod. Technol.*, vol. 9, no. 3, pp. 2263–2277, 2019, doi: 10.1007/s13202-019-0610-4.

[16] W. Graebel, *Advanced Fluid Mechanics*, 1st ed. Academic Press, 2007.

[17] J. C. W. E. Svendsen, *Lab-on-a-Chip Devices and Micro-Total Analysis Systems*. 2015.

[18] P. Tabeling, *Introduction to Microfluidics*. Oxford University Press, 2010.

[19] H. Bruus, *Theoretical Microfluidics*. Oxford University Press, 2007.

[20] M. J. Blunt, *Multiphase Flow in Permeable Media*. Cambridge University Press, 2017.

[21] M. Ryu, H. Kim, M. Lim, K. You, and J. Ahn, "Comparison of dissolution and surface reactions between calcite and aragonite in L-glutamic and L-aspartic acid solutions," *Molecules*, vol. 15, no. 1, pp. 258–269, 2010, doi: 10.3390/molecules15010258.

[22] D. Hong, M. Fan, L. Yu, and J. Cao, "An experimental study simulating the dissolution of gypsum rock," *Energy Explor. Exploit.*, vol. 36, no. 4, pp. 942–954, 2018, doi: 10.1177/0144598717751927.

[23] B. Kruczek, "Carman-Kozeny Equation," in *Encyclopedia of Membranes*, E. Drioli and L. Giorno, Eds. Berlin, Heidelberg: Springer Berlin Heidelberg, 2015, pp. 1–3.

[24] M. Dentz, T. Le Borgne, A. Englert, and B. Bijeljic, "Mixing, spreading and reaction in heterogeneous media: A brief review," *J. Contam. Hydrol.*, vol. 120–121, no. C, pp. 1–17, 2011, doi: 10.1016/j.jconhyd.2010.05.002.

[25] M. Raffel, C. E. Willert, S. T. Wereley, and J. Kompenhans, "Particle Image

Velocimetry: A Practical Guide, 2nd Edition," *Springer*, 2007.

[26] S. T. Wereley and C. D. Meinhart, "Micron-Resolution Particle Image Velocimetry."

[27] C. Eduardo and E. Perez, "Analysis , Comparison and Modification of Various Particle Image Velocimetry (Piv) Algorithms Analysis , Comparison and Modification of Various Particle Image Velocimetry (Piv) Algorithms," *Image (Rochester, N.Y.)*, no. December, 2004.

[28] MATLAB, "imbinarize." https://it.mathworks.com/help/images/ref/imbinarize.html (accessed Mar. 29, 2021).

[29] J. Yousefi, "Image Binarization using Otsu Thresholding Algorithm," *Res. Gate*, no. May, 2015, doi: 10.13140/RG.2.1.4758.9284.

[30] R. J. M. Bastiaans, *Cross-correlation PIV; theory, implementation and accuracy*, vol. 99, no. 1993. 2000.

[31] D. Dabiri, "Cross-Correlation Digital Particle Image Velocimetry – A Review by," pp. 1–54.

[32] L. N. Plummer, T. M. L. Wigley, and D. L. Parkhurst, "The kinetics of calcite dissolution in CO 2 -water systems at 5 degrees to 60 degrees C and 0.0 to 1.0 atm CO 2," *Am. J. Sci.*, vol. 278, no. 2, pp. 179–216, Feb. 1978, doi: 10.2475/ajs.278.2.179.

[33] MATLAB, "imgaussfilt." https://it.mathworks.com/help/images/ref/imgaussfilt.html (accessed Mar. 29, 2021).

[34] MATLAB, "adaptthresh." https://it.mathworks.com/help/images/ref/adaptthresh.html (accessed Mar. 29, 2021).

[35] MATLAB, "regionprops." https://it.mathworks.com/help/images/ref/regionprops.html (accessed Mar. 29, 2021).

[36] J. Blazek, "Principles of Grid Generation," *Comput. Fluid Dyn. Princ. Appl.*, pp. 373–413, 2005, doi: 10.1016/b978-008044506-9/50013-8.